Self organization of flow in dissolving rocks

Sharma, Rishabh

Self organization of flow in dissolving rocks

Rishabh Prakash Sharma

A dissertation submitted in fulfillment of the requirements
for the degree of Doctor of Philosophy

Under the supervision of

Prof. Mariusz Białecki
Department of Theoretical Geophysics
Institute of Geophysics, PAN

Prof. Piotr Szymczak
Faculty of Physics
University of Warsaw

Faculty of Physics

University of Warsaw

Mar 28, 2025

to my parents

Acknowledgments

This dissertation is the result of two decades of hard work—from my early school year to this day—by many people who have contributed in different ways to my well-being, emotions, and scientific curiosity—keeping me motivated throughout my scientific career and ultimately enabling me to complete this dissertation.

Among them, first and foremost, I would like to express my deepest gratitude to my supervisors, Prof. Piotr Szymczak and Prof. Mariusz Białecki. From the beginning of our collaboration, Piotr's enthusiasm for physics fueled my excitement and confidence in tackling a variety of challenging physics problems. He pushed me to my limits whenever needed, trained me in delivering presentations, and significantly improved my writing skills. His door was always open whenever I needed guidance, career advice, or scientific discussions. I am especially grateful for the immense amount of time he dedicated to reviewing this thesis.

My collaboration with Mariusz was equally inspiring. His articulated thinking and openness to working on diverse research problems motivated me to see this thesis through to completion. He was always available whenever I needed his support, and for that, I am truly thankful.

I would also like to extend my gratitude to Prof. Anthony J. C. Ladd for his valuable time and weekly discussions, particularly during his visits to Warsaw.

It is a pleasure to thank both Jingxuan Deng and Prof. Peter K. Kang for the collaboration, which resulted in an exciting application of dissolution patterns in transport physics.

I am also grateful to Prof. Maciej Lisicki for numerous insightful scientific and friendly discussions.

A special thanks to Dr. Max Cooper for his guidance during his postdoctoral time in Warsaw. This thesis would not have been possible without his experimental work.

I deeply appreciate Dr. Michał Dzikowski for his suggestions which are not only useful in scientific matters but also in life challenges. Many of his basic ideas, especially projecting 3D tomography scans on 2D plots, are further developed in this thesis. He was always available whenever I needed him.

I would also like to thank Stanisław Żukowski for taking the time to read my dissertation and provide valuable feedback.

A heartfelt thanks to my colleagues, Tomasz Swało, Antek Wrzos, and Dawid Woś, who not only created a friendly and supportive environment but also reminded me to take care of myself and eat on time.

I am especially grateful to my friends, Joydeep Sarkar and Dr. Vikul Tomar, whose brotherly love and emotional support helped me navigate through difficult times.

Finally, I want to thank my parents, my sister, and my beloved wife for their unwavering support—without which completing this thesis would have been impossible.

Rishabh P. Sharma
Mar 28, 2025

List of publications

During the course of my PhD research, the following publications have been produced:

Journal Articles:

1. J. Deng, **R. P. Sharma**, P. Szymczak, and P. K. Kang, “Anomalous Transport in Dissolving Porous Media: Transitions Between Fickian and Non-Fickian Regimes”, Geophysical Research Letters 2025 (Submitted)
2. **R. P. Sharma**, J. Deng, P. K. Kang, and P. Szymczak, "Effects of mixing at pore intersections on large-scale dissolution patterns and solute transport", Geophys. Res. Lett., 50(21):e2023GL105183, 2023.
3. **R. P. Sharma**, M. Białecki, M. P. Cooper, A. P. Radliński, and P. Szymczak, "Pore merging and flow focusing: Comparative study of undissolved and karstified limestone based on microtomography", Chem. Geol., 627:121397, 2023.
4. M.P.Cooper, **R. P. Sharma**, S.Magni, T.P.Blach, A.P.Radlinski, K.Drabik, A.Tengattini, and P.Szymczak, "4D tomography reveals a complex relationship between wormhole advancement and permeability variation in dissolving rocks", Adv. Water Resour., 175:104407, 2023.

Contents

Chapter 1

Introduction

The most beautiful thing we can experience is the mysterious. It is the source of all true art and science. He to whom the emotion is a stranger, who can no longer pause to wonder and stand wrapped in awe, is as good as dead; his eyes are closed.

Albert Einstein

1.1 Motivation

Pattern formation in nature is an ubiquitous phenomenon where intricate shapes often emerge from a seemingly complex and chaotic process. A very similar-looking structure can be observed in different physical systems. Conversely, within a physical system, the formed patterns can be very different from each other, which is due to their sensitivity to external parameters. For instance, a variety of shapes are observed in snowflakes (Fig. 1.1), which form due to the molecular arrangement of freezing water, depending on temperature and humidity.

The phenomenon of pattern formation is not limited to smaller systems such as snowflakes. It is also observed at larger scales such as in geological and cosmological systems. An impressive example of a geological pattern is the Giant's Causeway in Ireland (Fig. 1.2a), made by a polygonal arrangement of basalt columns, which are up to 12m in height. The striking feature of these columns is their hexagonal shape—sometimes there are pentagons as well—which is the result of shrinkage cracking of solidifying lava rocks [2]. Other fascinating examples of pattern formation in geology are stalactites (Fig. 1.2b) and stalagmites (Fig. 1.2d), which are formed in caves by precipitating $CaCO_3$ and can be of several meters in height [3]. The largest known examples of pattern formation are cosmic structures such as the logarithmic spiral galaxies (Fig. 1.2c). These galaxies consist of a flat, rotating disk which extends through gigantic spiral arms up to several light-years in size.

The origins of a vast majority of these patterns are still not well understood. The question, "How did these patterns emerge from a seemingly chaotic system?" baffled generations of scientists in different fields, including physics, chemistry, biology, mathematics, and computer science [5, 6]. One of the biggest hurdles in answering

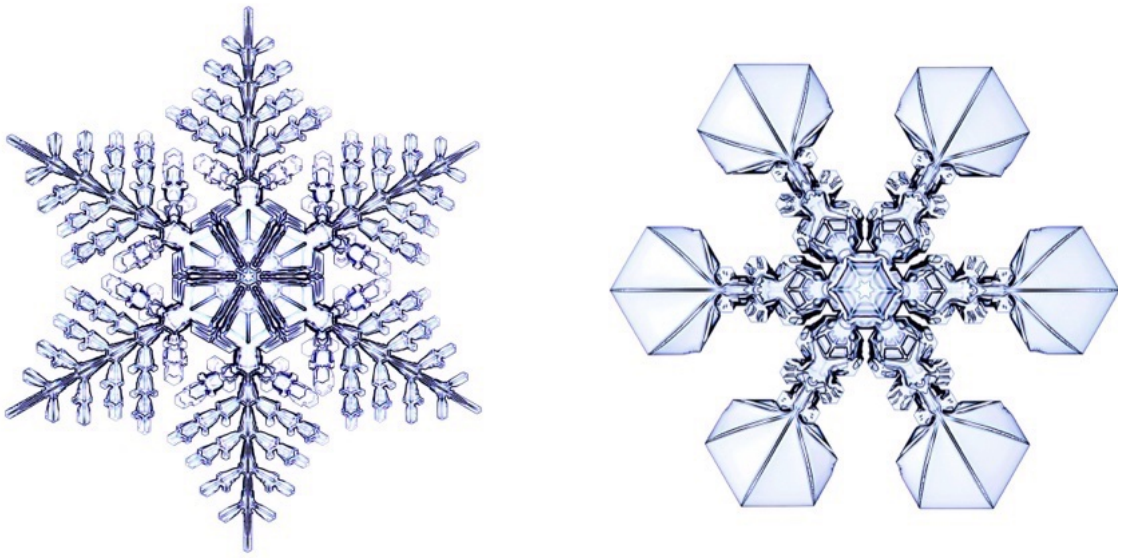

(a) (b)

Figure 1.1: Different types of snowflakes made in laboratory setup by Ken Libbrecht [1] (a) Fernlike stellar dendritic snowflake (b) Stellar dendritic snowflake.

this question is either the complexity of the process itself or the spatial and temporal scales of emerging patterns, which makes them hard to study in a laboratory under controlled conditions. However, in some systems, similar-looking patterns have been observed in laboratory experiments. This similarity between natural patterns and laboratory-made patterns is usually not coincidental but is a result of a similar mechanism of growth, even though the length and time scales in these systems differ significantly.

Physical instabilities are often referred to be the cause of the emergence of these patterns, regardless of their length scales. One classic example here is the Kármán vortex street [7]. In a laboratory setup, when flow moves around a cylinder at a certain speed, it can become unstable. In certain flow conditions, a regular pattern of alternating vortices known as Kármán vortex street appears [8]. These vortex streets are also observed in clouds near the Chilean coast when the wind hits Juan Fernandez island (see Fig. 1.3).

Another example of pattern-forming instabilities is Rayleigh-Taylor (RT) instability [9, 10], which appears at the interface of two fluids of different densities when heavier fluid is placed at the top of lighter fluid in a gravitational field. The heavier fluid forms a finger-like shape which streams downward while the lighter fluid rises upward. This instability has been observed in Crab Nebulae (Fig. 1.4a) after a supernova explosion which happened in 1054 AD and was witnessed by Arab and Chinese astronomers [11]. The supernova explosion formed a bubble of ejected heavy material trapping the lighter relativistic plasma known as the Crab synchrotron nebula, which pushes through the ejected heavy material. The remaining ejecta formed distinct filaments or finger-like shapes [12, 13]. It has also been observed in laboratory

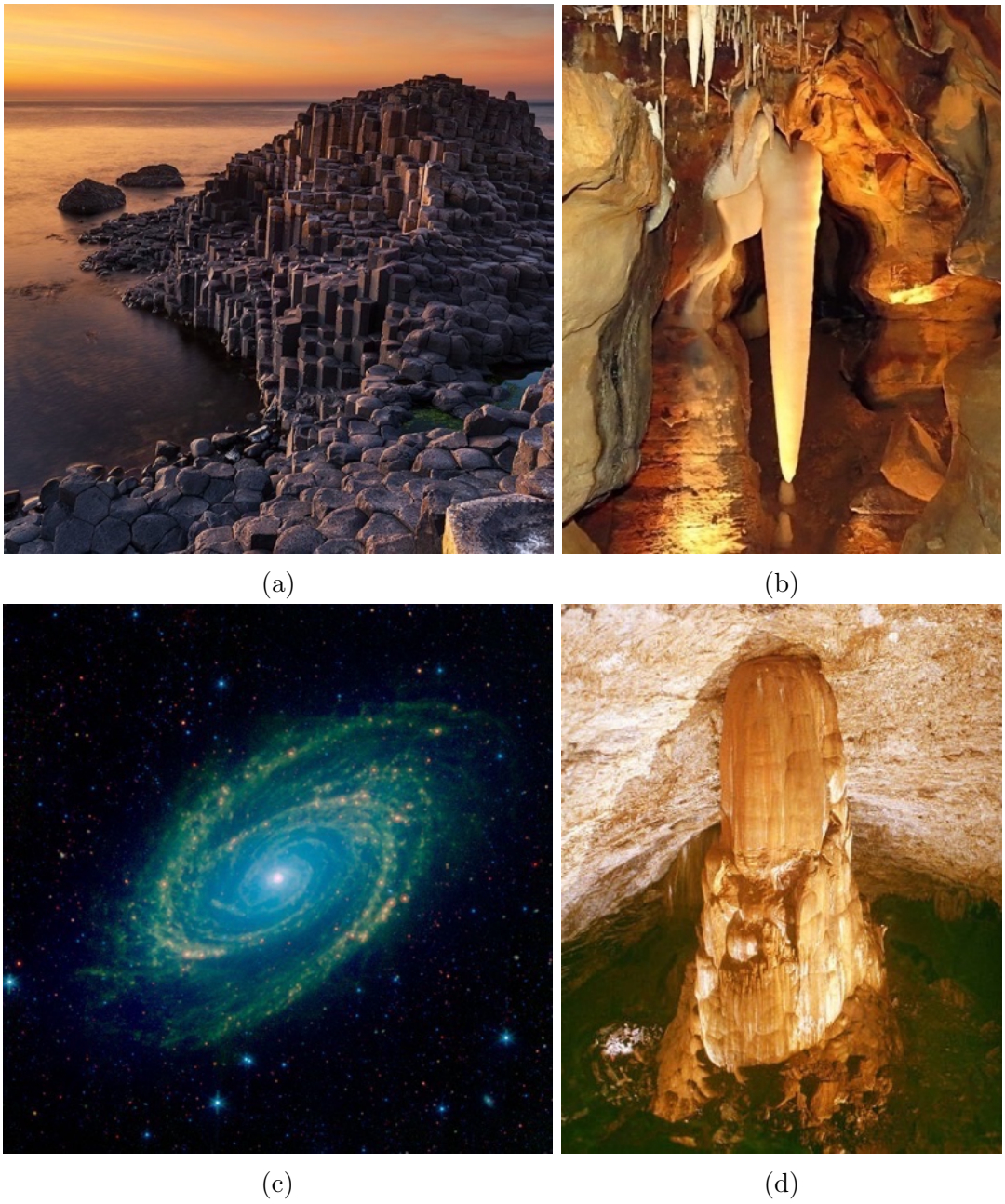

(a) (b)

(c) (d)

Figure 1.2: Pattern formation at large scale (a) Basalt columns in the giant causeway, Antrim, Ireland. Source: livingartphotography.ie (b) A stalactite—current size 1.5m—in Crystal King cavern in Ohio forming over the span of 250,000 years. Source: TrekOhio.com (c) The spiral shape of Messier 81 galaxy with a diameter of 96000 lightyears. Source: NASA [4] (d) World's second tallest stalagmite (67.2m high) in Cueva San Martin Infierno. Source: Kevin Downey, The Virtual Cave, (www.goodearthgraphics.com/virtcave/largest.htm). Note that a caver on the left, dressed in red, is almost invisible at the scale of the image.

experiments [9, 10, 14] (see Fig. 1.4b).

In this variety of examples we have mentioned, patterns can be categorized in dif-

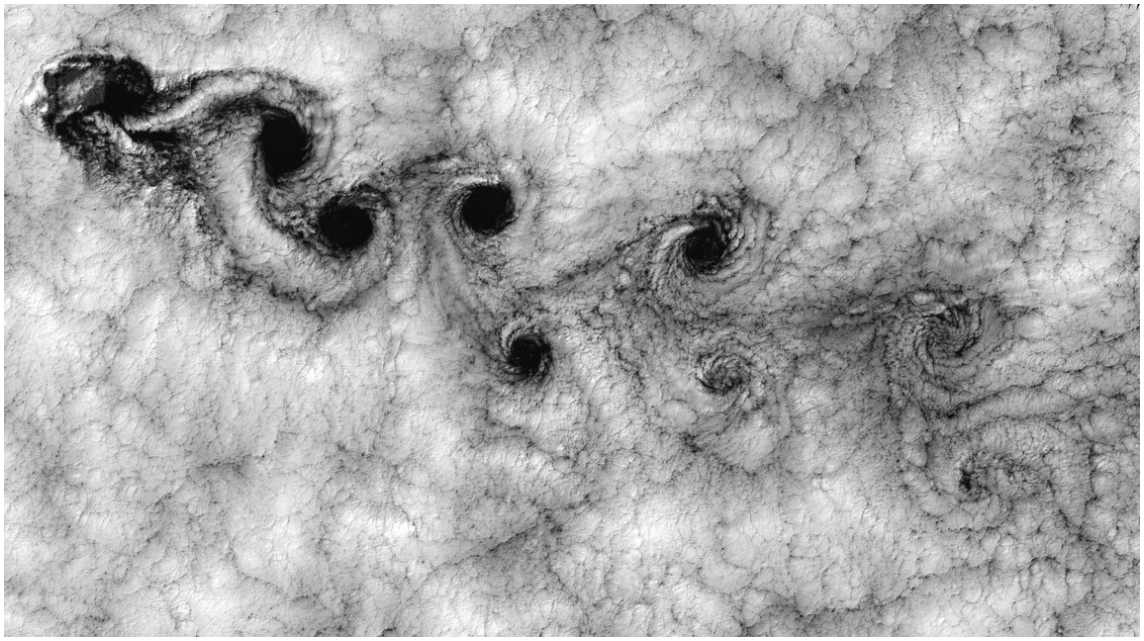

Figure 1.3: A satellite image, taken by Landsat 7 on 15 Sep 1999, shows Kármán vortex street imprinted on clouds, produced by wind flowing around Juan Fernandez island, which is at the top left corner. The island has a diameter of around 1.5 km and rises 1.6 km into the atmosphere. Source: NASA [7].

ferent ways such as tiling, branching, spirals, waves, and fingers. In this thesis, our main interest lies in fingering pattern which is very common in moving front problems where a boundary separating two phases (for example two liquids of different densities) moves initially with a flat profile. In certain conditions, the advancing interface becomes unstable and a slight disturbance in the front results in the appearance of sinusoidal-looking undulations which then transform into fingers. Previously mentioned RT fingers are a result of such process (Fig. 1.4b).

Moving front problems are particularly difficult to describe due to their lack of orderliness and their occurrence at far from equilibrium conditions. Typically, in systems close to equilibrium, regular shapes (for example, interface movement without any perturbation) are formed, but as the system is pushed far from equilibrium, the mechanism of self-organization takes place and distinct patterns with a range of complexity—for instance, fingers—emerge. The characteristic feature of far-from-equilibrium moving boundary processes is that the formed patterns are scale-free and can have fractal properties, for which the interactions between individual elements of the system are responsible.

Another important example of the moving front instability is Saffman-Taylor instability [15], which occurs at the interface of two fluids of different viscosities. When

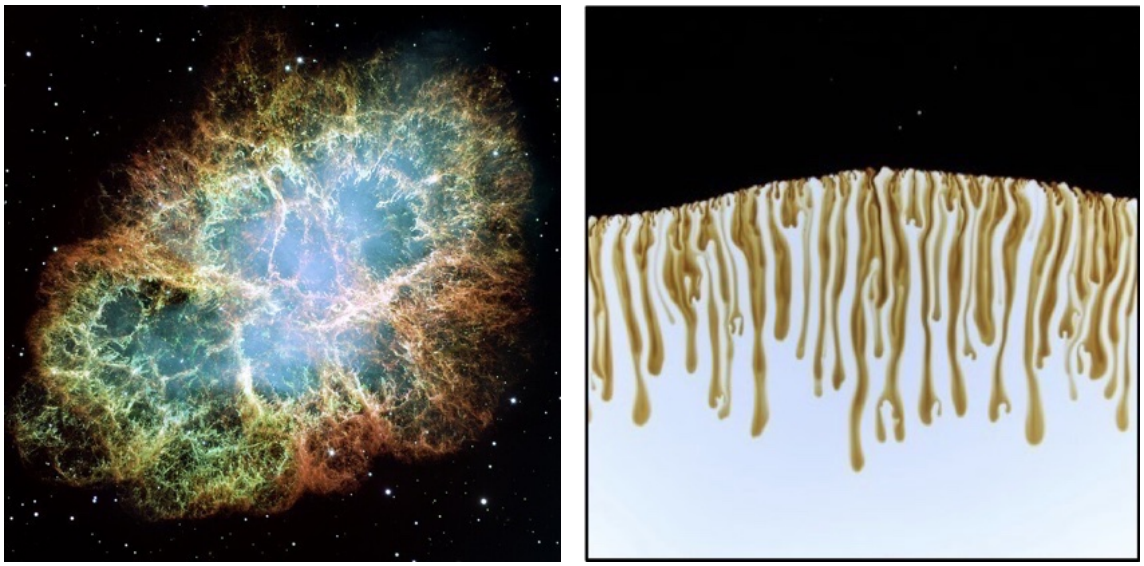

(a) (b)

Figure 1.4: Finger formations due to RT instability (a) Crab Nebulae. Source: NASA/ESA (b) In laboratory experiments, conducted in Hele-Shaw cell, consisting of two closely placed transparent plates, with heavier fluid moving from top to bottom. The resulting fingers are formed by denser fluid shown in brown color.

a less viscous fluid is injected into a system filled with more viscous fluid, it pushes through the more viscous fluid. The interface between these fluids becomes unstable and leads to the emergence of complex patterns. At lower injection rates, the interface moves smoothly; however, an increase in flow rates results in an unstable front, which splits into fingers (Fig. 1.5a). The shapes and dynamics of these fingers depend on different physical parameters such as injection rate, fluids miscibility and mobility ratio—the ratio of the viscosity of fluids [16]. In the case of two miscible fluids, a similar experiment as Fig. 1.5a produces a highly branched fingering pattern (see Fig. 1.5b) which is very different than the original experiment.

Moving front instabilities are not limited to fluids but are also observed in electromagnetic systems such as dielectric breakdown, where high voltage is applied between two electrodes separated by an insulating material. When the voltage difference between the electrodes increases sufficiently, the insulating material suddenly becomes conductive, forming fractal patterns known as Lichtenberg figures (Fig. 1.6a). A frequently encountered example of dielectric breakdown is lightning (Fig. 1.6b) in which the atmosphere acts as an insulator and the earth-cloud system acts as electrodes. However, the timescales of the formation of lightning patterns are very short, making it difficult to observe the details of dynamics with the naked eye.

Another example of the moving front problems in a non-fluidic system is the slow combustion of paper in a quasi-2D system [17]. In a Hele-Shaw cell, when a thin paper is burnt in controlled conditions against an oxidizing wind, a fingering instability develops. The shape of the fingers depends on several system parameters

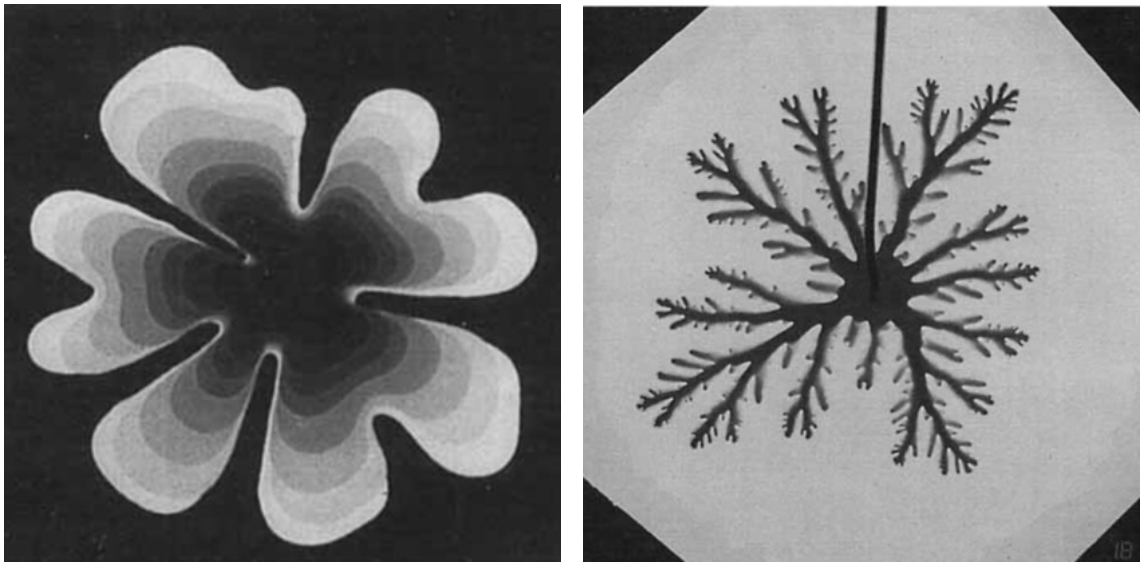

(a) (b)

Figure 1.5: Viscous fingering experiment conducted in a Hele-Shaw cell at same flow rates with (a) immiscible fluids and (b) miscible fluids, In (a) the time evolution of the pattern is captured by overlaying the digitized images of time-sequence photographs. The difference between both patterns is due to the presence or absence of surface tension. In the left figure, there is a sharp front indicating the surface tension effect while in the right figure, there is a diffuse front due to the absence of surface tension, shown by the gradient of grey color. [16]

including the amount of provided oxygen. At a higher volume of available oxygen, the paper burns uniformly. However, with a decrease in the amount of oxygen, the burning front becomes perturbed, and splits into fingers with recurrent tip splitting (Fig. 1.7a). The fingers compete for the available oxygen, and the ones closer to the oxygen source dominate, resulting in the screening of neighbouring fingers which stop growing due to unavailability of the oxygen. Further decrease of oxygen amount results in the formation of distinct fingers with larger spacing and without tip splitting (Fig. 1.7b).

Up to this point, we have discussed moving front problems only in physical systems, but it is also observed in a biological system This is rather unobvious to expect pattern formation in a system where a living organism is involved. However, when a bacteria colony such as *Bascillus subtilis* is allowed to grow on a Petri dish with a limited amount of food, it strongly competes for food and self-organizes itself for survival into strongly bifurcated fingers. (Fig. 1.8a). These patterns depend on the type and concentration of food as well as the species of bacteria. Moreover, in the same species, when the population of different morphotypes dominates, the competition leads to a change in the pattern after some time, which is entirely different from the parent generation colonies (Fig. 1.8b).

In most of the above-mentioned cases, the time scales of formation of the patterns from instabilities are relatively small. Furthermore, these patterns cease to exist as

(a) (b)

Figure 1.6: Fractal patterns in dielectric breakdown case (a) Lichtenberg figures produced in a lab experiment in acrylic specimens. The colour is artificially added using blue LEDs. Source: capturedlightning.com (b) Lightning in a storm as a result of atmospheric dielectric breakdown. Source: Wikimedia commons.

soon as the driving force disappears. One notable exception is pattern formation in geological systems in which the patterns can take thousands or millions of years to form and, once formed, can exist another millions of years. However, longer time scales also make them particularly hard to study as the evolution of the patterns can not be directly observed, and they might still be evolving while being studied. On the other hand, these processes shape our planet, and perhaps Mars as well [19, 20], by forming rivers, and karst landscapes such as valleys, sinkholes, and caverns, making them crucial subjects of study. Among this rich variety of patterns, some noteworthy examples of the geological patterns formed due to moving boundary processes are river networks, dendrites, and dissolution channels.

Probably one of the most commonly observed geological patterns is a river network, which is formed by flowing streams of water towards lower altitude regions. The water flows and erodes the land, resulting in the formation of a network of streams and tributaries which compete for water and continue to grow in a direction that corresponds to the water flux entering its head [21, 22]. These networks can have fractal features with numerous sub-streams and a unique feature—the direction of

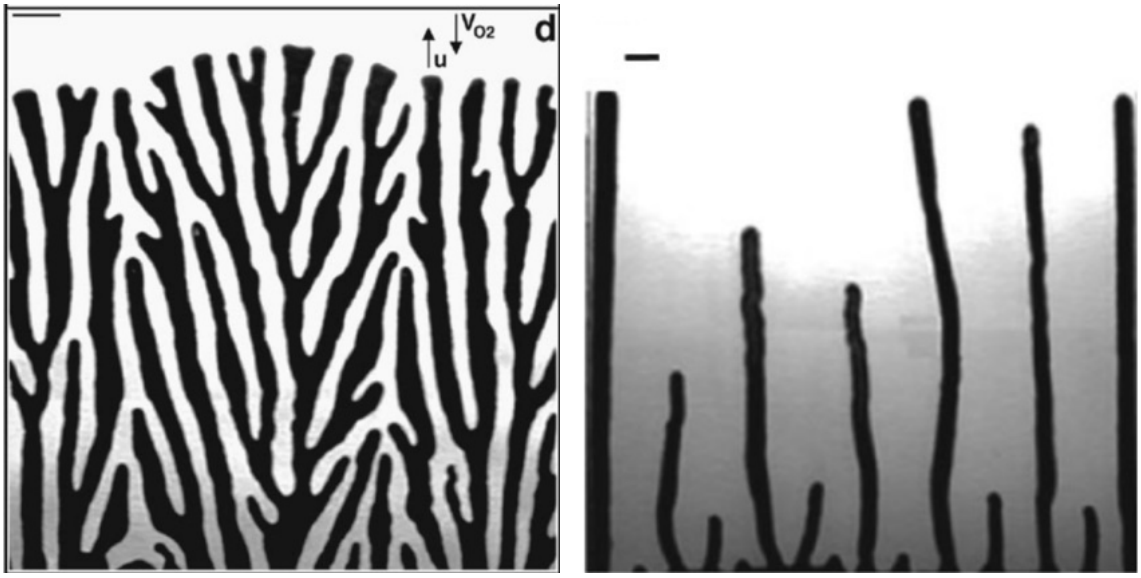

(a) (b)

Figure 1.7: Fingering patterns in the combustion of thin paper with a counter flow of oxygen with (a) tip splitting (b) distinct fingers without tip splitting. Two characteristic length-scales are observed: finger width and spacing. The latter is the function of the amount of oxygen available—the smaller the amount, the larger the spacing, resulting in stronger screening of neighbouring fingers. [17]

(a) (b)

Figure 1.8: *Bascillus subtilis* colony growth experiments on a Petri dish with the same concentration of food (a) first generation colony with fractal-like shape (b) a mutated colony with chiral pattern with a notable feature of the same twist of all the branches. [18]

the growth of these networks, contrary to other fingering patterns, is opposite of the flow direction. Fig. 1.9a shows a high-resolution topographic view of a river network

near Bristol, Florida. The streams flow toward the Apalachicola River (on the left).

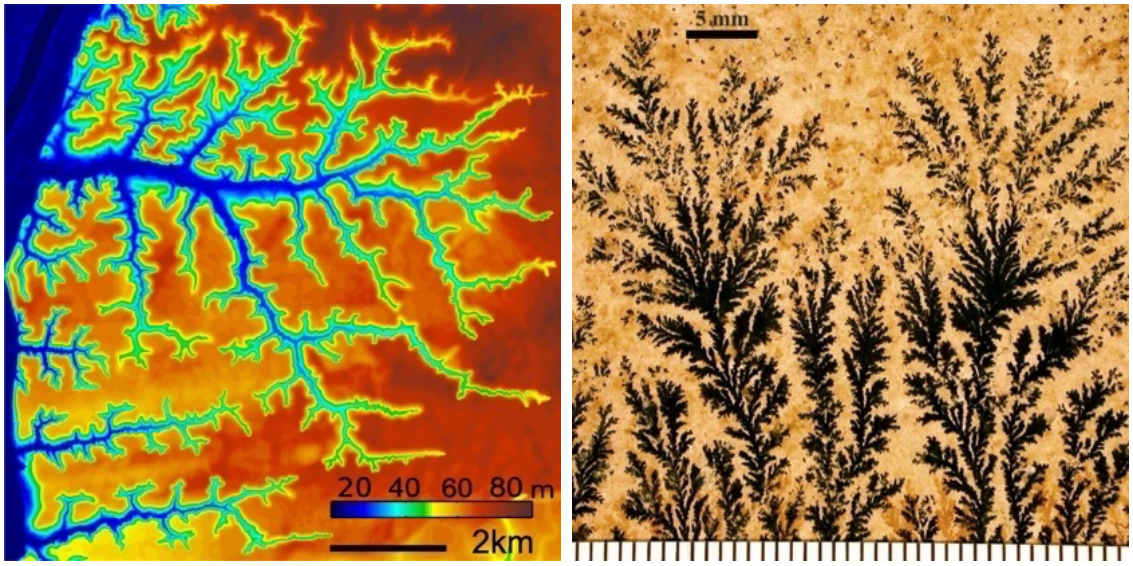

(a) (b)

Figure 1.9: Examples of geological patterns (a) Topographic map of a river network located near Bristol, Florida. The colour represents here the height of the valley [21] (b) Mineral dendrites (scale at bottom in mm) formed by manganese on a limestone, Solnhofen, Germany. Source: Mark A. Wilson, Department of Geology, The College of Wooster.

Another noteworthy example of a geological pattern are mineral dendrites which are fractal-like structures formed by precipitation of minerals. Two categories of dendrites exist: the first one is a crystalline dendrite, whose shape is governed by crystalline structures, for example, metal crystals; the second one is non-crystalline dendrite, which is usually observed in rocks (Fig. 1.9b). The former is very common in metallic growth processes in which the crystallization of minerals takes place in a supercooled solution [23]. The latter forms when a super-saturated solution (for example manganese rich water) infiltrates a porous rock and precipitates metal oxides, while mixing with the oxygenated solution [24]. The resulting branches are highly irregular, contrary to crystal dendrites, where crystallographic angles govern the branching angle. The geometry of these patterns is controlled by concentrations of chemical reagents, interfacial energy, diffusion coefficients, and temperature [25].

1.2 Dissolution patterns

So far, we have provided a general overview of various examples of fingering patterns observed in moving boundary processes across physical, biological, and geological systems. A more specific example of moving front problem is chemical erosion (dissolution), which is the main interest of this thesis, and the corresponding patterns are known as dissolution patterns. Notable examples of these patterns are karst caves, dolines, sinkholes, karst funnels, solution pipes, and wormholes. These patterns are very common in carbonate systems where reactive fluids such as acidic

water dissolve the minerals of the rock. The formation of these intricate patterns is a complex process in which the interplay of reaction and transport plays a vital role. Here, the dissolution front creates an interface between the dissolved and undissolved parts of the rock. The dissolved phase grows in an undissolved phase, resulting in the occurrence of reaction-infiltration instabilities [26]. As a result, the interface between dissolved and undissolved phases is prone to be perturbed, and a slight perturbation can grow into finger-like shapes. The resulting dissolution fingers can exist in many forms across various length scales—from centimeter scale redox fronts in siltstones [27] to kilometer scales uranium rolls [28].

(a) (b)

Figure 1.10: (a) Solution pipes in limestone rock observed in an active quarry in Smerdyna, Poland, with a colleague as a scale. The freshly uncovered pipes are filled with clay. (b) A hollow solution pipe in Roca-Vecchia, Italy, with a hammer as a scale. Photos: Author

Dissolution patterns are observed in a variety of natural systems where CO_2 enriched ground water flows through a rock and chemically dissolves the carbonate minerals, permanently altering the morphology of the rock. However, this process is not instantaneous—the reaction front advances along the flow direction, gradually dissolving the rock. A small perturbation in the front can evolve into distinct fingers over hundreds to thousands of years. Notable examples of dissolution-induced structures are solution pipes (Fig. 1.10) which are finger-shaped formations that form in carbonate rocks over thousands of years [29]. However, it was not always obvious that these patterns are formed due to dissolution. For instance, in the case of karst caves, till the 18th century, it was believed that the mechanical erosion of rock by flowing water was forming caves [30, 31]. In the 19th century, Lyell [32] was the first one to point out that the caves are formed due to the chemical erosion of limestone by water surcharged with carbonic acid.

Dissolution fingers are also important in many engineering processes where the ex-

amples of their application range from the stability of dams built on a soluble rock [33], CO_2 sequestration process [34], risk assessment of contaminant migration in groundwater [35], to the reservoir stimulation process [36]. However, unlike the natural formations, in many engineering applications dissolution rates are higher and the system can be dissolved in a matter of hours. A relevant example here is the acidization of petroleum reservoirs, where a strong acid is injected into the permeable rocks of a reservoir to increase oil extraction. The acid enlarges the pores in reservoir rocks and stimulates the flow of oil. The most efficient stimulation of a reservoir is obtained when the flow self-organizes into a small number of distinct channels and bypasses the rest of the medium. In fact, petroleum engineers have observed the formation of these channels in the oil stimulation process and named them wormholes (see Fig. 1.11), similar to the holes made by worms [37–40].

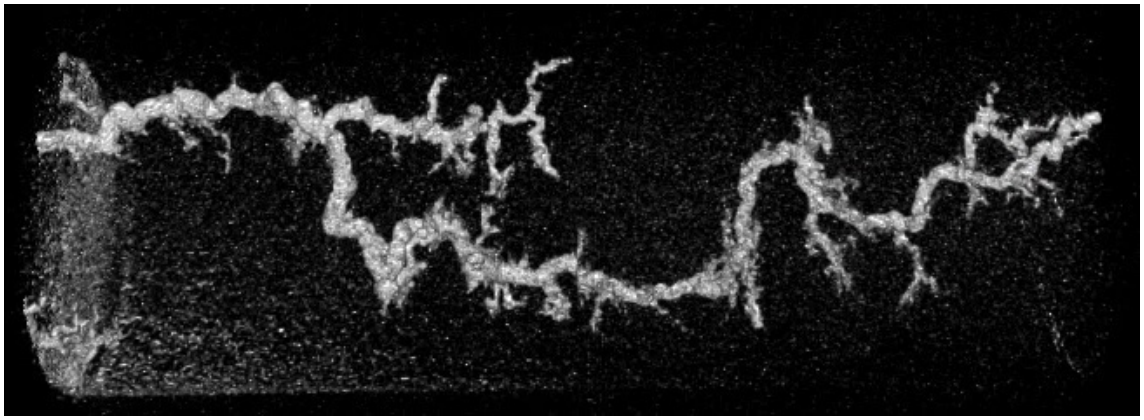

Figure 1.11: A wormhole formed in a lab experiment conducted on Pińczów limestone core with length 11.9 cm and diameter 3.8 cm. The sample is dissolved by HCl solution, which was injected from the left. The data is obtained using an X-ray imaging technique and post-processed to extract the formed channel. [41]

Studying the processes involved in the formation of dissolution patterns and the factors influencing their shape and morphology is the main theme of this thesis. Based on the previous studies [37–39, 42–44], it has been concluded that the shape and geometrical properties of dissolution channels depend on system parameters such as flow through the system, system length and heterogeneity, and the reaction rate of the reactive fluid. For instance, in a sample of fixed size, injection of an acid with a very low flow rate leads to face dissolution—the reaction front is flat and incoming acid is consumed at the inlet pores. On the other extreme, if the flow rates are high, the reactant is consumed simultaneously in all pores, resulting in uniform dissolution of the entire sample. The most interesting regime (wormholing regime) is observed with moderate flow rates. At moderate flows, the reaction front splits into fingers, dissolving certain areas of rock faster and bypassing the rest of the system.

1.3 The Thesis

This dissertation is an attempt to gain an improved understanding of the factors influencing the shape of dissolution patterns as well as their effect on the system in which they form. In particular, it is dedicated to investigating the role of rock heterogeneity and pore-scale mixing process on the shape and growth dynamics of dissolution patterns, as well as to examining how dissolution, in turn, affects and modifies the pore-space of the host rock.

The growth of wormholes is often shielded from our eyes due to the rock mass surrounding the structure. Initial studies of the dissolution process were limited to the visual observation of the rock cores in which dissolution patterns form. Since the rocks are non-transparent, it was only possible to record openings at the inlet and outlet side of the samples where the channels first emerged. A significant advancement was to extract the shape of formed channels using non-invasive methods such as casting Wood's metal into the developed wormhole or using tomographic imaging techniques [37, 45, 46]. This allowed the visualization of the final stage of the dissolving sample and the extraction of the final wormhole network. However, the understanding of the growth dynamics of these patterns remained limited to measuring the changes in permeability and pressure throughout the experiment. Bazin et al. [47], in their pioneering work, developed an approach for in-situ observations of dissolution process. The growth dynamics of wormholes were studied by taking 2D scans (i.e radiographs) at different locations of the sample. Nevertheless, the dynamics was still hard to capture due to technological limitations on acquisition times. The channels progress relatively fast inside the rock; therefore, a shorter acquisition time was required to capture the growing wormholes.

More recently, tomographic imaging technique has been increasingly employed in wormhole studies [48–51], although it was still restricted to ($\sim$ 30) min time resolution, typically allowing only a few 3D scans per dissolution experiments. Cooper et al. [41] further improved the tomography method by balancing resolution with acquisition time and were able to conduct up to $\sim$ 130 scans per experiment with scan times as short as five minutes. This approach has provided an unprecedented insight into the progressive development of wormholes within the sample. The time-lapse experiments conducted by Cooper et al. [41] showed that the tip of a dissolution channel does not move linearly in the mean flow direction but shows speed-ups in different regions of the sample. Moreover, the final wormhole showed geometric features such as turns in the lateral direction and different branching intensities along the length. These detailed geometric properties of a wormhole are important for understanding its growth dynamics; however, they have not been extensively studied. Li et al. [52] attempted to characterize the geometric properties of dissolution patterns in laboratory made gypsum samples. Laboratory-made gypsum cores are relatively homogeneous in comparison to the cores made of naturally formed limestone. Consequently, the wormholes observed in gypsum [52] show less geometrical complexity compared to, for example, the wormhole formed in Pińczów limestone [41]. We expect that local rock inhomogeneities influence the shape of dissolution patterns; even in the same rock, the formed wormholes can be different between the

samples, and this variability can be correlated to the heterogeneity of the rock.

In Ch. 5, we will attempt to address these issues by studying the geometry of dissolution channels formed in the cylindrical cores of different limestones as well as in plaster of Paris cores made in a laboratory. We will use grayscale tomography data collected from two types of experiments: first one, when the sample is scanned during dissolution, resulting in a time-series data of evolving wormhole. In the second case, scanning is done after the dissolution experiment finishes. For both types of data, the developed image processing methods—such as volume segmentation, connected component and skeletonization—will be discussed. These methods will be used for the removal of noise, existing voids and grains from the scans, and finally isolating the dissolution channels. We will first investigate the effect of tomography scan resolution on its ability to capture the fine details of wormhole geometry. Later, we will discuss the characteristics such as tortuosity and length wastefulness, used by us for the characterization of the geometry of these patterns. These characteristics will be calculated for the wormholes formed in different dissolution experiments. Next, we will extract the tip movement of wormholes in different time-series experiments. Finally, we will attempt to correlate all wormhole characteristics with rock properties and injection rates.

Dissolution patterns are usually observed at the macro scale, while the reactive transport driving the emergence of these formations takes place at the pore scale. The governing process, dissolution, is controlled by transport within pore-bodies, as well as chemical reactions at the rock surfaces. However, the flow magnitude and concentration profile within the rock are global in nature and highly sensitive to large-scale heterogeneities or the presence of preferential flow paths. This micro-to-macro scale coupling may be significantly intensified by dissolution, especially in the unstable regime, where existing flow paths are enhanced, and new ones appear [53, 54]. Recent research has demonstrated that pore-scale properties significantly impact large-scale phenomena, suggesting that macroscopic transport can be influenced by pore geometry and distribution of the minerals at pore scale [55, 56]. Furthermore, pore-scale transport processes such as mixing are shown to significantly affect the effective surface reaction rates [57–60].

The pore-scale mixing process is important in reactive flows as it influences the transport of reactants and mixing-induced reactions. In particular, mixing at pore intersections is very important because fluids with different properties vigorously mix and react in these areas. Previous research has pointed out that the extent of mixing at pore intersections can govern solute spreading at a larger scale [61–63]. This implies that dissolution patterns can also be influenced by mixing at these intersections, with recent studies indicating that there is a wide range of mixing conditions which can occur at intersections [64, 65]. Note that these modelling studies do not use a continuum approach, where fundamental equations (like Navier-Stokes) are applied in actual pore space. Instead, they introduce a simplified representation of porous medium as pores and intersections. This leads to a problem of determining how to partition the concentrations at the intersections—specifically, which percentage of the incoming concentration from each pore should go to each outgoing pore. This problem is remedied by introducing mixing rules at intersections, which

account for mixing intensity at pore intersections. Nevertheless, the effect of pore-scale mixing rules on the shape of macro-scale dissolution patterns remains unclear, with most of the modelling studies assuming full mixing condition at pore intersections [37, 38, 56, 66]. This is mainly due to the absence of a universal, coarse-grained mixing rule that quantifies the degree of mixing at intersections.

We attempt to fill this gap in Ch. 6 by using a modelling approach, similar to Budek and Szymczak [66], and Roded et al. [56], in which we will assume that pore space can be represented as a network of interconnected cylindrical tubes, which can widen as a result of dissolution. In order to study the effects of the mixing of reactive solutes at pore junctions on large-scale dissolution patterns, we will implement two mixing rules at pore junctions into the pore network model of a dissolving porous medium. The first is so-called full mixing. It assumes that the solute transport at pore junctions is diffusion-dominated such that reactive solutes become well mixed. The second is streamline routing which assumes that the system is advection-dominated such that reactive solutes follow streamlines and do not transit between streamlines at pore junctions. This leads to partial mixing or even a complete lack of mixing of incoming concentrations at junctions. Using the network model, we will investigate the influence of different mixing rules on the shape of the channels formed in networks of different heterogeneity.

Till now, we discussed a number of factors which can influence the shape of dissolution patterns. However, the pore space of the host rock also evolves with the development of the patterns. Recent advancements in tomographic measurement provided insight into the dynamics of evolving pore space during chemical transformation [48, 53, 67–71]. The alteration in solid phase volume, along with the associated modification to rock structures, characterized by changes in reactive surface area, tortuosity, and connectivity, have been studied and linked with the progress of the reaction and evolving flow paths within the sample. To quantify the dynamics of evolving pore space, two characteristic features of dissolution have been identified. The first are the changes in reactive surface area of dissolving rocks [72–75]. It is well-known that in rocks of relatively smaller porosity, the specific reactive surface area increases during the early stages of dissolution. As the pores widen, more mineral surface is exposed. However, this trend reverses at a certain point due to pore merging, with reactive surface area ultimately decreasing to zero as the porosity approaches unity [74]. Here, the mechanisms of pore space evolution are pore widening and pore merging, where the latter is arguably the most elusive process in mineral dissolution, difficult to characterize in a quantitative manner [76]. The second challenging aspect of dissolution is its multi-scale nature: flow and transport are influenced by the large-scale properties of the medium, while the chemical reactions are controlled by the local geometry of the fluid-mineral interface [37, 56, 77–79].

Contrary to the large amounts of data collected from lab experiments, much less is known about the changes in the pore geometry due to natural dissolution. One of the reasons for such a situation might be the difficulty in making a comparison of the dissolved rock geometry with the original one since, in many cases, the latter is no longer available, as the entire rock mass has undergone the transformation.

In Ch. 4, we attempt to fill this gap by analyzing the changes in pore-geometry of rock as a result of natural dissolution. For this purpose, we will use samples of naturally dissolved limestone rock, which are collected from a karstified area near a solution pipe. Using the tomography data of the samples, we will first extract the pore space, and then carry out a comparative study of it by quantifying the changes in pore geometry of each sample. For quantification, we will use various geometric properties such as connectivity, flow tortuosity, thickness distribution, and ellipsoid factor, which are measured using image processing methods. We will show that in our samples, natural dissolution resulted in an inhomogeneous growth of the pore space, with pore-merging playing a key role. The occurrence of pore merging is confirmed by an analytical model of local thickness change as well as by the analysis of the evolution of geometrical properties. In addition, we will show that dissolution is strongly focused on largest pores, resulting in a decrease in number of flow-paths and flow-tortuosity.

1.4 Structure of thesis

This dissertation consists of seven chapters: the first three are introductory, while the following three present the main findings of the thesis. For the reader without any prior knowledge of dissolution patterns, Ch. 2 presents the physics behind their formation. It delves into various concepts, such as reaction-infiltration instability, dimensionless numbers, breakthrough curves, and pressure curves, which are important tools for studying dissolution patterns. The following chapter, Ch. 3, deals with the modelling of dissolution process. It discusses three main modeling approaches: micro-scale models, continuum models and pore network models. Ch. 4 is the first result chapter which presents a study in which we analyze the changes in pore geometry of limestone induced by the natural dissolution. In the method section of this chapter, we present several image analysis methods, including connectivity, thickness distribution and ellipsoid factor, which are adopted from bone research [80, 81]. In addition, we will investigate the changes in flow characteristics in both samples by calculating the flow field numerically. The flow field will be used to calculate the permeability ratio and flow tortuosity.

In the following chapter, Ch. 5, we investigate the influence of rock characteristics and flow rates on the evolution of wormhole shape and its geometry. For this purpose, we use the tomography data obtained from the dissolution experiments [41] which were conducted by Dr. Max P. Cooper. We have data from several experiments in which cylindrical cores of two types of rocks, Pińczów and Wierzbica limestone, were dissolved at a range of flow rates. This data is processed using a specially devised segmentation method—volume-based segmentation which combines the typical segmentation process and connected component algorithm—to extract the shape of the wormholes. The extracted wormholes are then converted to network graphs following the skeletonization process [82]. These graphs are further used in the characterization of the geometric characteristics of a wormhole. We first investigate the influence of different resolutions of tomographic data on the geometry of a wormhole. Next, we study the time evolution of the tip of wormholes in

Pińczów limestone by analyzing the time-series 3D X-ray scans. Finally, we analyze the geometry of the wormholes using the geometrical characteristics such as tortuosity and length wastefulness, and study their dependence on the rock structures and the flow rates.

The next chapter, Ch. 6, presents a study related to the effect of micro-scale mixing process on large-scale dissolution patterns. We first introduce two end members of mixing rules: full mixing and streamline routing. Then, we discuss the implementation of both mixing rules in a pore network model, introduced in Ch. 3. Later in the result sections, we simulate dissolution patterns using both type of mixing rules for a range of Damköhler numbers in the networks of different heterogeneity. The shape of the dissolution patterns is analyzed, both qualitatively and quantitatively. We also investigate the influence of mixing rules on the amount of reactant required for a wormhole to reach the outlet. Finally, we study the effect of system heterogeneity and the sensitivity of mixing rules towards it.

Chapter 2

Physics of dissolution patterns

Water is fluid, soft and yielding. But water will wear away rock, which is rigid and cannot yield. As a rule, whatever is fluid, soft and yielding, will overcome whatever is rigid and hard. This is another paradox: what is soft is strong.

Lao Tzu (600 BC)

2.1 Introduction

In the general introduction of the thesis (Ch. 1), we have discussed different types of pattern formation observed in nature, especially dissolution patterns, which is our main focus. In this chapter, we will discuss more specifically the physics of dissolution and how it leads to the emergence of patterns in a carbonate rock. In Sec. 2.2, we will explain the basic concepts behind the emergence of dissolution patterns from a perturbed dissolution front. Then, in Sec. 2.3, the dimensionless numbers will be discussed, which control the form of the patterns.

A porous carbonate rock is made of voids and solid grains—fossils and impermeable minerals—which are usually distributed non-uniformly. More than that—there are micro-cracks, fractures, and voids etc—in the field, limestone can be very heterogeneous across all scales, resulting in a non-uniform distribution of flow paths in the system. The injected reactant, following these flow paths, preferentially flows through the regions of larger permeability and dissolves them. The dissolution of the pore matrix enlarges the existing flow paths, causing them to receive even more flow. The complex interplay of reaction and transport results in the preferential growth of some regions over others and leads to the spontaneous appearance of intricate patterns.

Dissolution patterns are observed both in laboratory experiments and in nature, where dissolution timescales are extremely long, making them particularly difficult to study. In contrast, laboratory experiments allow the use of much stronger acids than those present in natural systems. This shortens the dissolution timescales and enables the study of pattern formation in a controlled environment. Hence, to

understand the physics of the problem, we will review the past experimental studies in Sec. 2.5.

Many factors can influence the shape of dissolution patterns including physical parameters, such as flow rate, system length, rock porosity, and permeability, as well as processes like pore-scale mixing and chemical kinetics. These factors can strongly influence the dissolution mechanism, potentially leading to entirely different dissolution regimes within the same rock. The effect of these factors will be discussed in Sec. 2.7.

2.2 Reactive-infiltration instability

Reaction-infiltration instability is a physical mechanism [26, 83], which is known to be behind the formation of dissolution patterns. In a dissolving medium, a planar reaction front is potentially unstable to an arbitrarily small perturbation. A positive feedback loop of dissolution and transport amplifies certain wavelengths of the perturbation, resulting in the splitting of the reaction front into finger-like protrusions. Here the positive feedback loop refers to a closed loop of a sequence of processes in which each process amplifies itself through the others in the loop. In reactive transport process, reaction enhances flow, flow enhances the transport of reactant, which in turn speeds up the reaction.

Using linear stability analysis, Chadam et al. [26] were the first to show that reaction-infiltration instabilities can arise in dissolving rocks and result in the formation of fingering patterns. This process can be understood intuitively. Let us consider a small protrusion in a planar reaction front, as shown in Fig. 2.1a by a solid line. Behind the reaction front, the medium is dissolved and, therefore, has lower hydraulic resistance compared to the undissolved medium ahead of the front. Incoming flow preferentially focuses within the bump and brings more fresh reactant to the tip of the perturbation. As a result, the bump dissolves faster (dashed line in Fig. 2.1a) compared to the neighborhood and gets amplified.

Fig. 2.1b shows a time-evolution of dissolution fingers from multiple small protrusions in microfluidic experiments [84]. Initially, the perturbations exhibit a nearly sinusoidal pattern. However, as the nonlinear effects of dissolution begin to dominate their dynamics, the protrusions evolve into finger-like shapes. These fingers compete for the available flow and screen each other off. Consequently, the screened fingers stop growing and merge with the winning fingers.

2.3 Dimensionless parameters

To study a physical phenomenon, it is a common practice to use dimensionless numbers obtained from non-dimensionalizing the governing differential equations. We will also adopt a similar method by non-dimensionalizing the advection-diffusion-reaction (ADR) equation, governing the transport of a reactant in the system. The obtained dimensionless numbers provide a convenient way to compare the relative

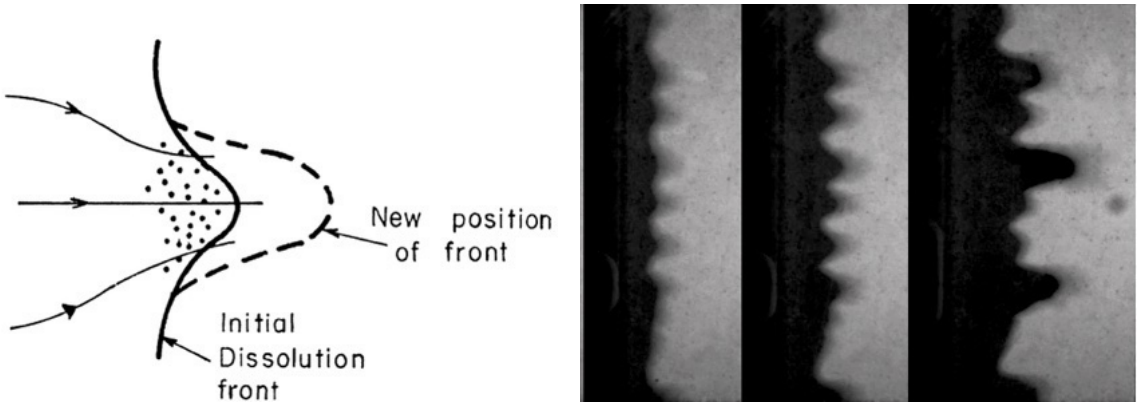

(a) (b)

Figure 2.1: (a) A perturbation in a planar dissolution front (solid line). The left side of the perturbation is the dissolved phase, while the right side is the undissolved one. The flow comes from left to right and focuses within the bump, resulting in faster growth of the bump. The dashed line shows the new position of the perturbation. Source: Ortoleva et al. [83] (b) Evolution of fingers from dissolution instabilities in a fracture dissolution experiment performed in microfluidic setup—gypsum, shown in grey colour, is dissolved using distilled water. Flow direction is from left to right, and the dissolved part is black [84].

importance of different terms of the governing equation (e.g. advective flux to diffusive flux).

2.3.1 Damköhler number

Damköhler number (Da) is a dimensionless number, named after *Gerhard Damköhler* (1908 – 1944), used in chemical engineering. It is defined as the ratio of advective time scale (τ_A) to reactive time scale (τ_R). In a porous medium in which a reactant is injected at a constant volumetric flowrate (Q), the advective time scale can be defined by ($\tau_A = l_0/v_0$). Here l_0 is the characteristic length scale over which the solute is transported advectively, and v_0 is the Darcy velocity, defined as ($v_0 = Q/A$), where A is the cross-section area of the porous medium. Similarly, the reactive time scale can be defined by ($\tau_R = d_0/k$), where k is the reaction rate constant (assuming first-order kinetics), and d_0 is the characteristic length for geometry change (i.e pore diameter or grain size). Using these definitions Da can be written as following:

$$\mathrm{Da}(l_0, d_0) = \frac{\tau_A}{\tau_R} = \frac{k l_0}{v_0 d_0}, \tag{2.1}$$

When $\mathrm{Da} \gg 1$, the reaction time scale is smaller in comparison to the time scale of advective transport of solute to the mineral surface. The reactant is consumed at the inlet, with less being transported inside the system. On the other hand, for $\mathrm{Da} \ll 1$, the advective time scale is smaller, and the reactant is transported and consumed deep in the system. The whole system dissolves homogeneously as the reactant invades the whole system and dissolves all the pores throughout the system.

2.3.2 Péclet number

Péclet number (Pe), named after *Jean Claude Eugene Péclet* (1793-1857), is a dimensionless number which is very useful in studying different transport phenomena. It is defined as the ratio of diffusive time scale (τ_D) to advective time scale (τ_A). In a porous medium, diffusive time scale can be written as ($\tau_D = l_0^2/D$) where D is the diffusion constant of the reactive fluid. Then, Pe can be written as following:

$$\mathrm{Pe} = \frac{\tau_D}{\tau_A} = \frac{v_0 l_0}{D} \tag{2.2}$$

For larger length scales ($\mathrm{Pe} \gg 1$), flow in the system is naturally advection-dominated, while for smaller l_0, Pe is $\ll 1$; therefore, diffusion dominates the transport phenomenon.

2.4 Penetration length

In dissolving system, penetration length (l_p) relates to a natural length scale that represents the spatial decay of reactant concentration in the mean flow direction (Fig. 2.2). Bazin et al. [39] reported that in the same physical conditions, samples with different lengths dissolve differently—permeability of the 5cm sample increases faster compared to the 20cm long sample, indicating a reactant penetration length l_p between 5cm and 20cm. This shows that in laboratory experiments, the ratio of the penetration length to the system length (l_p/L) is an important parameter. However, this ratio plays a much less important role in natural systems, e.g. karst conduits or cave systems, where the system size is usually very large [85, 86].

Let us consider a homogeneous porous medium of size L, and specific reactive surface area s_0 (defined as reactive surface area per unit system volume). The reactive transport in this medium is governed by advection-reaction equation.

$$\frac{dc}{dx} = \frac{-k s_0 c}{v_0} \tag{2.3}$$

On integrating Eq. 2.3, we obtain $c = c_{\mathrm{in}} \exp(-k s_0/v_0 x)$ where the term $(v_0/k s_0)$ is the penetration length l_p. Note that, $l_p/L = 1/\mathrm{Da}(L, 1/s_0)$ according to the definition 2.1.

In an advection-dominated system, such as described above, penetration length is proportional to the flow rate. For larger flow rates, penetration length is larger, which means a similar reactant concentration is available along the whole length of the system, resulting in a nearly uniform dissolution of whole system at the same time. On the other hand, for smaller flow rates, the penetration length is also smaller, and the reactant is consumed close to the inlet, resulting in face dissolution.

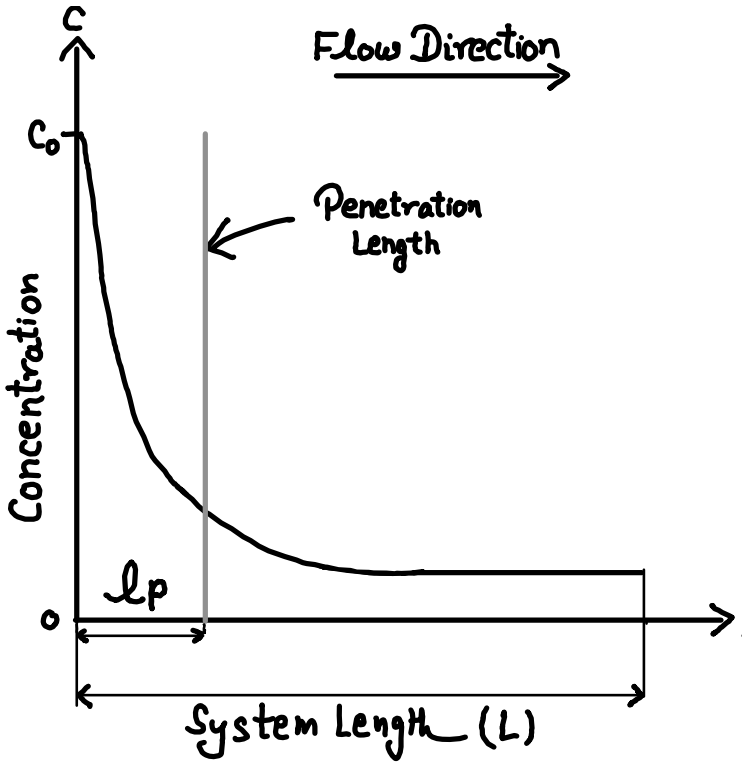

Figure 2.2: A schematic description of decay of reactant concentration c along the length of the system L with penetration length l_p.

2.5 Dissolution patterns in experiments

Studying dissolution patterns is of key importance from geological and industrial perspectives; however, due to the large length and time scales involved, there is a limited amount of methods to study these processes. Laboratory acid-flooding experiments on rock cores offer precise control over system parameters like pressure, temperature, and reactant concentration, making them an efficient way to study the formation of dissolution patterns. In these experiments, changes in pore space can be directly measured before, during, and after the tests.

In a core-flooding experiment, a reactant such as hydrochloric acid (HCl), is used to dissolve samples of a carbonate rock.

$$2\,H^+ + CaCO_3 \longrightarrow Ca^{2+} + CO_2 + H_2O \tag{2.4}$$

One of the first experimental studies related to the formation of dissolution patterns using core-dissolution experiments was conducted by Hoefner and Fogler [37] in 1988. In this study, cylindrical cores of different carbonate rocks were dissolved using a reactant in a pressurized system. The experimental setup consists of a high-pressure cell to which a high-pressure pump is connected, and injection of a reactant is performed either at a constant flow rate or at constant pressure. Fig. 2.3 shows the schematic of the setup in which the pump is connected to a reactant source. The

pump injects a reactant, such as HCl, at the inlet of the cell (bottom) and keeps the flow continuous. To prevent the flow of reactant around the core, a confining pressure is applied between the cell wall and the core surface. In addition, to avoid the formation of CO_2 in the gas phase (Eq. 2.4) and keep the flow single-phase, back pressure is maintained in the sample by a back-pressure regulator downstream of the sample.

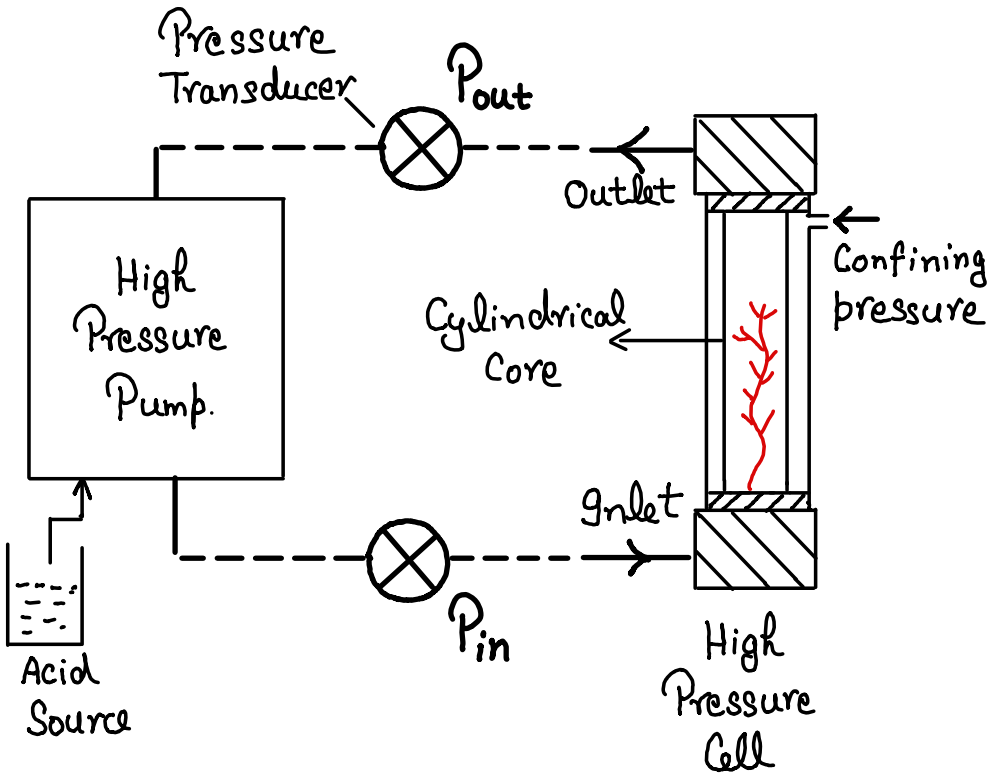

Figure 2.3: A schematic of general core-flood experimental setup.

Using this setup, Hoefner and Fogler [37] dissolved several limestone cores with a range of acid injection rates. Fig. 2.4 shows the wormholes formed in different limestone samples with increasing flow rates. A smaller injection rate leads to face dissolution in which the acid flux is insufficient to propagate inside the core, and acid is consumed at the surface (Fig. 2.4a). At slightly higher flow rates, the reaction front becomes unstable. As a result, the acid starts penetrating inside the pores, creating a dissolution channel. However, due to the relatively slow velocity, most of the acid is consumed at the walls of the channel before reaching the tip; therefore, it propagates slowly and increases its size in a lateral direction to mean flow. The formed wormhole is very wide near the entrance, with a decrease in diameter along the length. The required amount of acid for the wormhole to reach the outlet is also very large. This regime of wormholing is known as a conical regime (Fig. 2.4b). At moderate flow rates, the channel becomes thinner with a slight branching (Fig. 2.4c). More unconsumed acid starts reaching the tip of the wormhole. As a result, the wormhole propagates faster and increases the permeability of the sample significantly while spending the least amount of acid volume. Further increase in flow rates results in

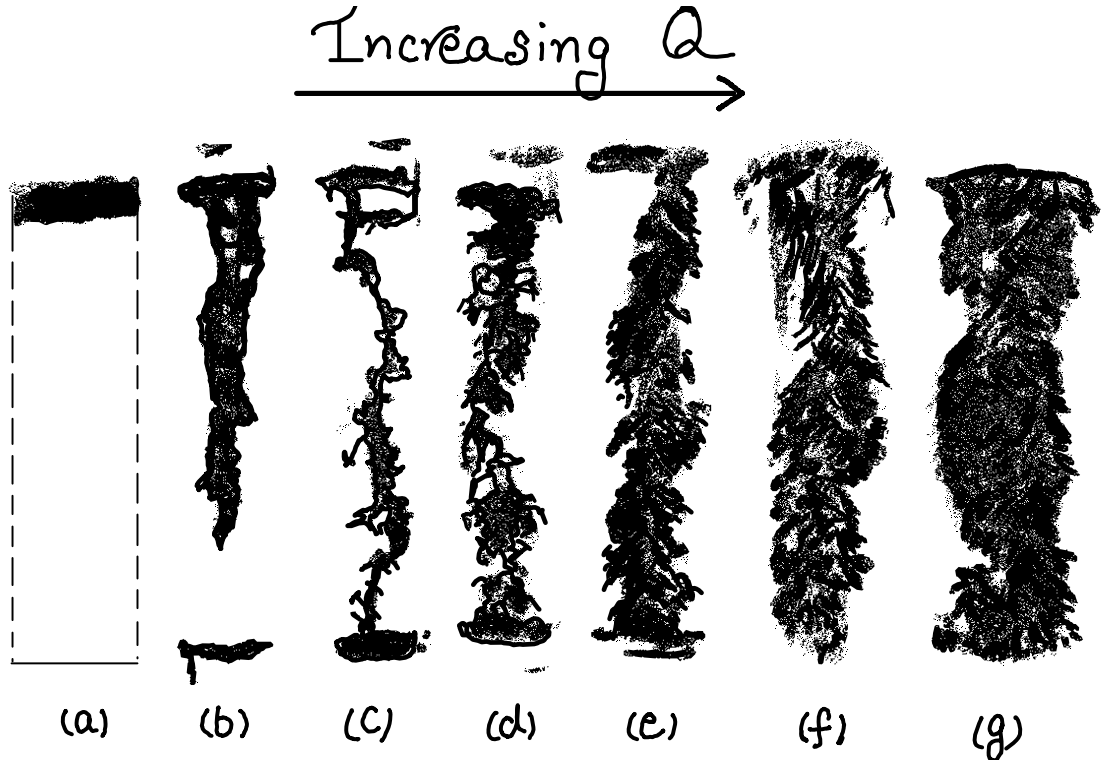

Figure 2.4: Dissolution patterns obtained in the experiments conducted by Hoefner and Fogler [37] by injecting HCl in limestone samples at different flow rates (a) Illustration of face dissolution is added by the Author (b-g) Adapted from Hoefner and Fogler [37].

the formation of multiple pathways simultaneously, and the resulting patterns are highly ramified with stronger branching (Fig. 2.4d-g). With even larger flow rates, the reactant invades the whole pore space simultaneously and dissolves the sample uniformly. This regime of dissolution is known as uniform dissolution regime.

Golfier et al. [43] also correlated the transition of dissolution regimes and the resulting change in dissolution patterns to injection rates (i.e. to Pe), and reported that in water-NaCl system face dissolution and uniform dissolution are observed at very low and very high injection rates, respectively. At intermediate flow rates, conical, dominant, and ramified wormholes are observed in sequence as injection rates increase. In addition, a Pe-Da phase diagram (see Fig. 2.5) was also reported, based on the numerical simulation of salt dissolution process. Note that, Da in this study is defined as $\mathrm{Da} = \alpha l/v$ where α is the mass transfer coefficient, l and v—similar to the Eq. 2.1—are the pore-scale characteristic length and inlet velocity, respectively. This definition of Da is essentially similar to our definition of $\mathrm{Da}_{\mathrm{eff}}$ in transport-limited dissolution, which we will discuss in Ch. 3.

The diagram reported by Golfier et al. [43] shows that the transition between the face dissolution, conical, and dominant wormhole regime does not depend only on the Péclet number but also can be influenced by Damköhler number. For example, with $\mathrm{Pe} \leq 10^{-2}$, no dominant wormholes are observed for any Da regime, while for $\mathrm{Pe} > 10^{-2}$, uniform dissolution as well as ramified and dominant wormholes are

observed, depending on Da.

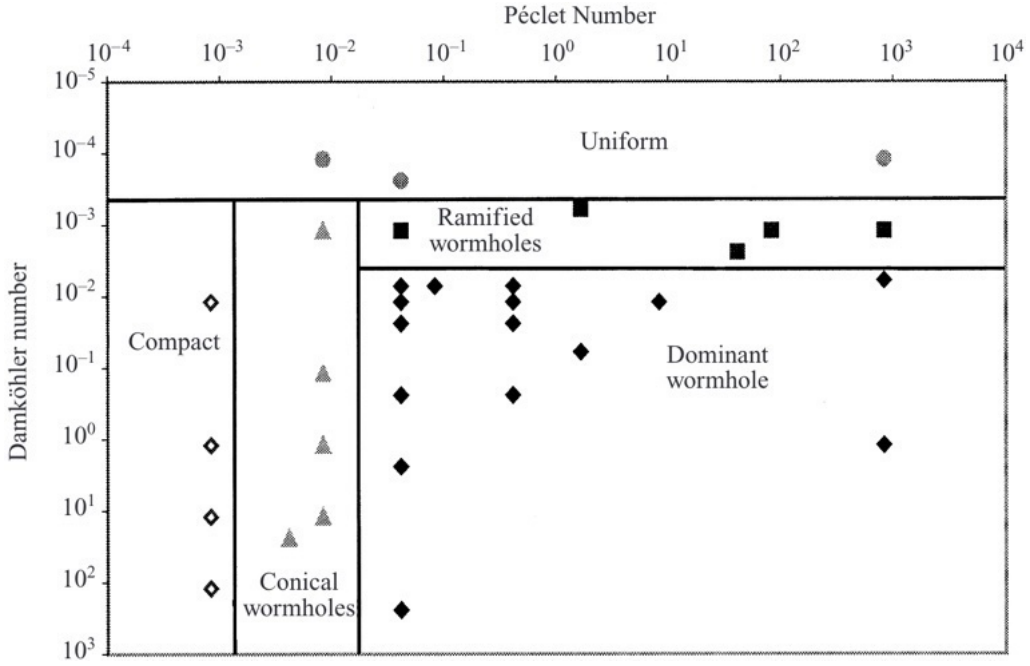

Figure 2.5: Pe-Da phase diagram for water-salt system where points indicate the type of wormhole observed in numerical simulations. [43]

A similar variety of wormholes is also reported in several other studies [39, 42–44, 87–90]. However, the key emphasis is placed usually on dominant wormholes due to their importance in the oil industry, since they minimize the amount of reactant needed to significantly increase the permeability of the sample. Experimentally, this is investigated by measuring the amount of reactant required for a wormhole to reach the outlet (referred to as breakthrough) as a function of the Damköhler number.

A typical shape of a breakthrough curve is presented in Fig. 2.6, with a well-defined minimum corresponding to the Damköhler number at which dominant wormholes appear. On the other hand, both extremes—low and high Da—of this curve show a larger amount of reactant volume needed to achieve breakthrough. At low Da, dissolution occurs across all pore surfaces, leading to significant reactant consumption. At high Da, in the face dissolution regime, the front moves steadily from the inlet to the outlet, and breakthrough can only be achieved by dissolving the entire sample, again requiring a large amount of reactant

Fredd and Fogler [38] noted that for different acids the wormholes corresponding to the optimum Damköhler number are morphologically different (Fig. 2.7) from each other. For instance, the channels formed with stronger reactant (HCl) and weaker reactant (acetic acid, HAc) are relatively thinner while the wormholes formed with chelating agents—organic molecules that release protons (H^+ ions) when mixed with water, forming a weak acid—are wider and diffuse. In addition, the wormhole formed with the weakest acid (HAc) is highly tortuous with the least amount of branching.

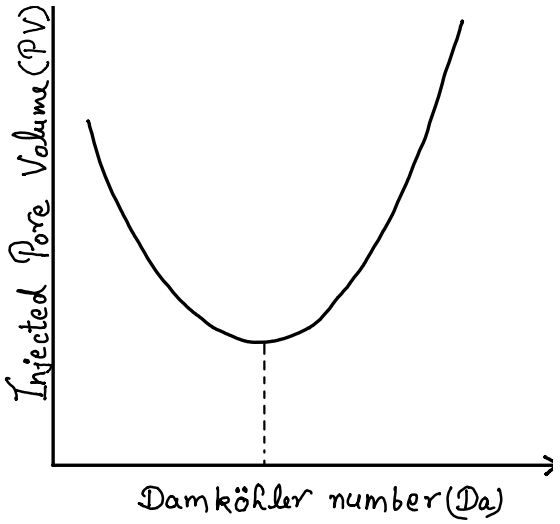

Figure 2.6: Illustration of the dependence of injected volumes of reactant (pore volume) required to obtain breakthrough on Damköhler number. Note that from Eq. 2.1, Da is directly related to injection rate Q, (Da $\sim 1/Q$).

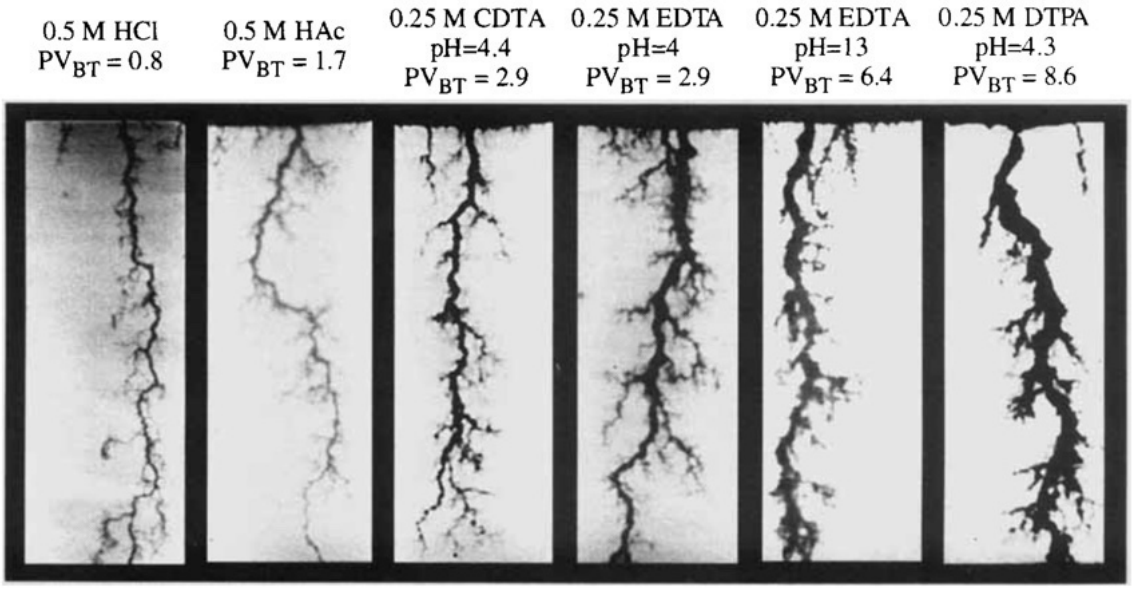

Figure 2.7: Dominant wormholes formed in limestone-core dissolution experiments with different type of reactants. Note that, in all these experiments, the reactive solution prepared from different reactants has same effective acid capacity which means that they all can dissolve at similar rates. Wormholes formed with strong acid HCl and weak acid (acetic acid, HAc) are relatively thinner than the wormholes formed with chelating agents (panels 3-6 from left). Furthermore, the branching intensity varies in the wormholes, with HAc wormhole showing least amount of branching, while chelating agents showing stronger branching. [38]

Another step forward in research on dissolution patterns was associated with the advancements in CT scanning. A good example of the level of detail that such an approach can provide is the work of McDuff et al. [40] who studied wormholing using

phase-contrast X-ray imaging technique. This method exploits the fact that different materials have different refractive indices, resulting in a phase-shift in the passing X-ray beams. The obtained scans provide detailed information on 3D characteristics of the wormhole by utilizing phase shift enhanced contrast (see Fig. 2.8).

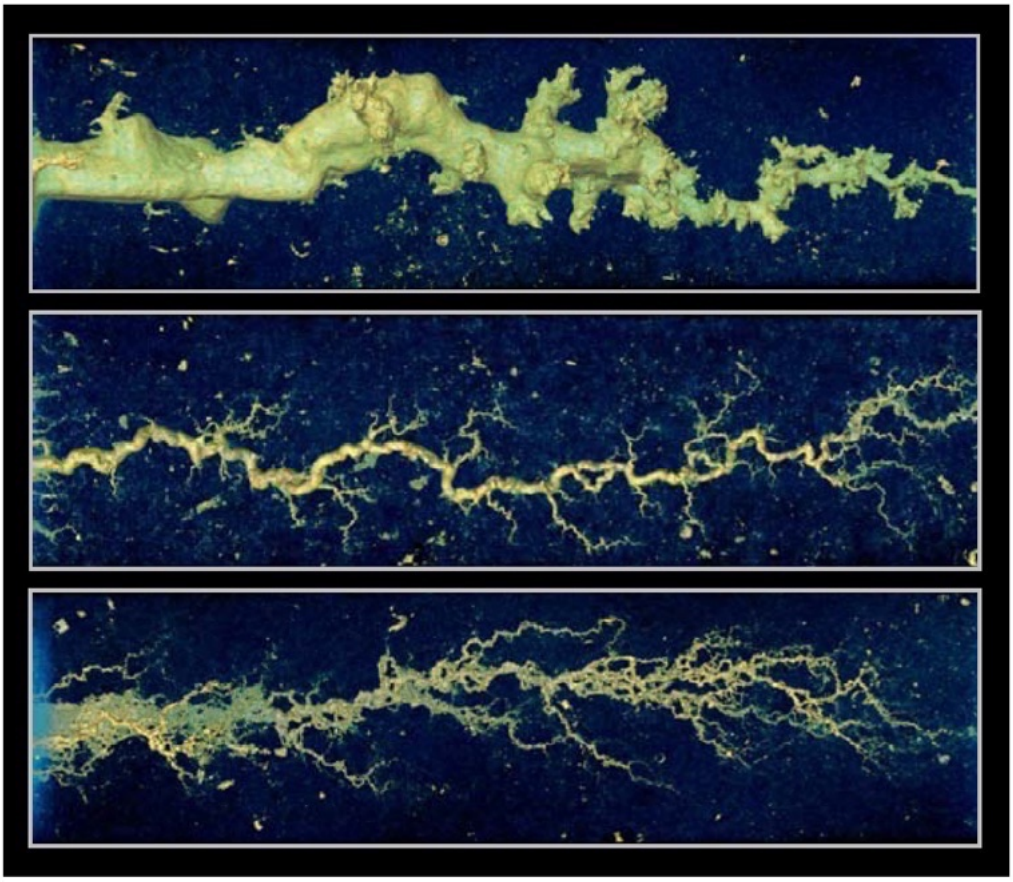

Figure 2.8: Visualization of different wormholes in dissolution experiments performed on Indiana limestone samples. The middle panel corresponds to optimum injection rate, while the top and bottom panels correspond to lower and higher injection rates with respect to optimum. These visualizations show detailed geometric features of wormholes, which were not observed in 2D radiographs. [40]

With recent advancements in X-ray micro-CT technology, in the last decade, several authors [48–51] attempted to capture the intermediate stages of the wormhole evolution by scanning a dissolving sample inside the X-ray machine. However, due to technical limitations the scanning time remained larger than a characteristic wormhole propagation time. A better time resolution (even up to 125 frames per experiment) was reported in a recent study by Cooper et al. [41]. Interestingly, such detailed data revealed that the extension of the tip of the wormhole is highly non-uniform in time, with periods of slower growth interspersed with sudden jumps.

2.6 Permeability evolution in dissolving system

The evolving channels in a sample increase its permeability, which can be quantified by observing pressure drop evolution with time across the sample in the experiments in which the injection rate of the reactant (Q) remains constant in time. The correlation of wormhole length with the increasing permeability of the sample can be explained using a toy model [47, 52, 91]. Let us consider a homogeneous system with initial permeability K in which a wormhole is growing in the mean flow direction, left to right (Fig. 2.9). The total length of the system is L, and at a certain instant, a wormhole has developed up to the length z. Further, let us assume a negligible hydraulic resistivity in a wormhole, in comparison to that of the surrounding medium and approximate the flow in the part beyond the wormhole tip (of length L-z) by a uniform flow. By applying Darcy's law ($Q = K\Delta P/(L - z)$), we can obtain a linear decrease of the total hydraulic resistance of the sample with the length of the wormhole (Fig. 2.9):

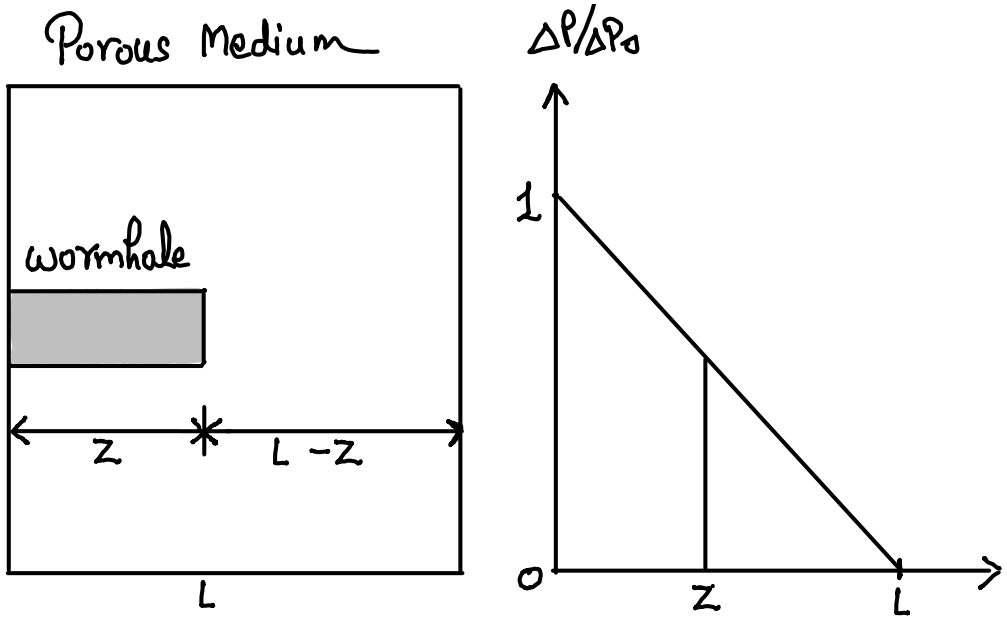

Figure 2.9: (left) A model of dissolving porous medium with a wormhole of length z inside, shown in grey colour. (right) The corresponding pressure (ΔP) drop along the length in this simplified model, normalized pressure by initial pressure drop (ΔP_0) without the wormhole.

Hill et al. [91] reported a similar linear pressure curve in core-flood experiments in which cores of Indiana limestone were dissolved at different injection rates. In the same study, however, the pressure curve obtained in dolomite dissolution experiments showed a deviation from linearity in terms of plateaus and large drops, indicating that wormhole progress was not uniform. Several other studies [39, 41, 92] also reported non-uniform pressure drop curves. For instance, in HCl-limestone system Bazin et al. [39] observed plateaus and drops in pressure curve (ΔP) in the dominant wormhole experiment. Similar behaviour is also observed by Izgec et al. [92], who attributed it to the vugs, where pressure drop is related to the intersection

of vugs and wormholes. In another experimental study, conducted by Cooper et al. [41], the non-linear pressure curves were correlated to layers of small porosity. The wormhole moves faster through these regions, which is accompanied by a significant change in the permeability of the sample.

The limited understanding of the non-linear behaviour of the (ΔP) curve is related to the lack of information on the evolving dissolution patterns. In most of the studies [37–39, 43, 45, 47, 87, 93], the X-ray scans of the samples were usually taken either at the beginning or at the end of experiments, ignoring the details of the temporal evolution of the pattern. We will return to these matters in Ch. 5

2.7 Other factors influencing dissolution patterns

As already mentioned, dissolution patterns do not depend only on the flow rate and reaction rate, but also on the characteristics of the rock matrix, such as porosity, permeability as well as the degree to which these properties are heterogeneous within the rock [37–39, 43, 47, 87, 92–95].

Porosity refers to the overall void fraction of pore space in a rock, but it also includes local variations in the sample such as packed regions [41, 96] and larger vugs [92]. These local variations can influence the shape and growth of dissolution channels. For example, high local permeability of the vugs can lead to flow focusing and attract the moving tip of the wormhole. On the other hand, the packed regions of lower porosity act as obstacles to the flow. In core-dissolution experiments, conducted on Pińczów limestone samples, Cooper et al. [41] observed that dominant wormhole progress non-uniformly within the sample. While passing through a packed layer, wormhole show speed-ups in tip movement, which was correlated to relatively larger drops in pressure curves. In another study, Petrus and Szymczak [96] reported that larger porosity contrast between the packed layers increases the competition between wormholes. The growth of the smaller ones is hindered and entire flux is directed to the winning channel. The stratification (layers) also affected the shape of the channel with characteristic narrowing within the packed region and the bulbous widening as it emerged from the layer.

The relation between permeability and porosity is not always simple. A sample with well-connected but relatively low porosity can have higher permeability, while a sample with larger porosity can still have lower permeability. Frick et al. [93] showed that in Austrian limestone samples (permeability range 0.2 - 2md), dissolution patterns are influenced by rock permeability; the channels formed in highly permeable samples are of dominant type, even at the lower injection rates—it is contrary to the results reported by other authors [37, 38] who observed conical channels at similar injection rates. However, Dubetz et al. [95] argued that there is no significant correlation between permeability and breakthrough volumes. Furthermore, Ziauddin and Bize [97] suggested that the permeability of tip region can also influence the shape of these patterns. In experiments conducted with rocks of different permeability and porosity, even with similar breakthrough curves, the wormhole formed in Austin chalk ($\phi \approx 25\%$ and $K \approx 14$md) were more ramified compared to Win-

terset limestone ($\phi \approx 16\%$ and $K \approx 17$md). The lower permeability of tip region of Austin chalk wormhole allow acid to explore multiple flowpaths, resulting in a more branched wormhole. Similar findings of combined effect of porosity-permeability are also supported in several other numerical studies [43, 56].

Summing up, the formation of dissolution patterns is a complex process which can be influenced by several factors including the rock structures and injection rates. Recent advancements in imaging and modeling technologies have significantly improved our understanding of the processes underlying the formation of these patterns. However, the complexity of wormholing remains challenging due to the non-linear coupling between processes at micro- and macro-scales. The following chapters will explore these issues in greater detail, beginning with a discussion of different modeling approaches for studying dissolution patterns.

Chapter 3

Numerical modelling of dissolution process

All models are wrong, but some are useful.

George Box

3.1 Introduction

This chapter aims to give a brief overview of the modelling approaches of dissolution process and set up a framework for numerical study presented in Ch. 6. In last two decades, several models have been proposed to study dissolution [37, 38, 45, 56, 66, 79, 98–111], which can be broadly classified into three main categories: pore-scale, continuum-scale and network models. The representation of scale comparison of Darcy and pore-scale models is shown in Fig. 3.1.

At pore-scale, the pore space is fully resolved and each point of it is occupied by either a solid phase or a liquid phase. Therefore, to model dissolution at pore-scale, an accurate description of pore matrix is required. The first pore-scale models were introduced in the pioneering work of Békri et al. [98]. These models solve for flow and reactant transport in the actual, three-dimensional pore-space geometry, built either numerically or reconstructed from the tomographic data. With recent advances in X-ray micro-tomography and computational power, there has been a surge in pore-scale studies [79, 101–110, 112], encompassing the X-ray imaging techniques, characterization methods, experimental studies, numerical simulation, and various combination of these approaches. We will discuss these models in detail in Sec. 3.2.2. Despite the ability to capture accurate pore-scale physics, pore-scale models are computationally very expensive. To reconstruct the fine details of a pore matrix, substantial information on pore space is required. Furthermore, the time needed to model the relevant time scales is often prohibitive. These requirements limit the pore-scale approaches to micro-scale systems and make them impractical for studying larger (km-scale) systems.

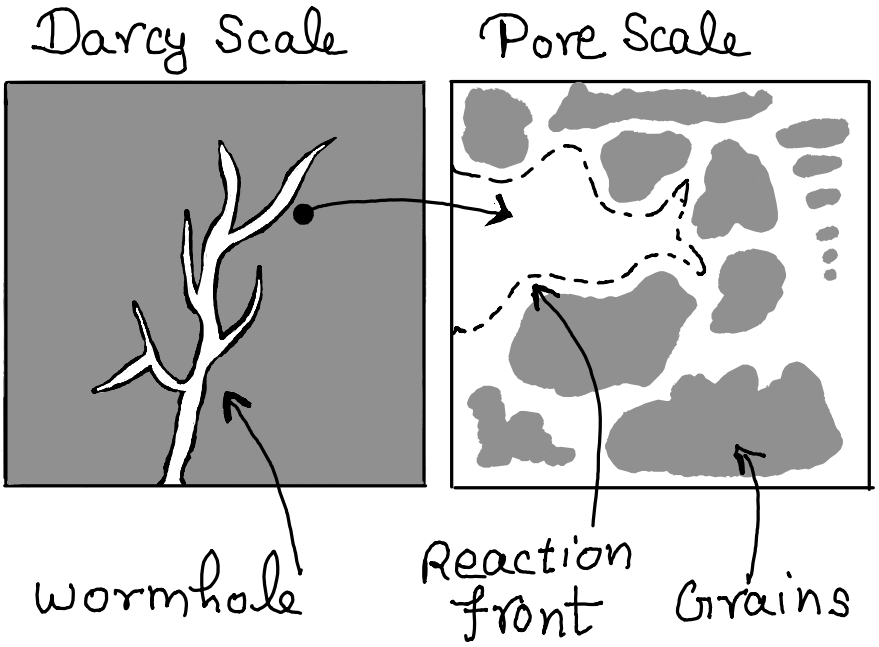

Figure 3.1: Representation of a dissolving porous medium at different scales which are used in modelling. The gray colour represents the matrix phase, while the white colour represents the empty space (pores). (left) At Darcy scale, porosity of the medium is a continuous field where the details of porosity are still unresolved. A wormhole-like feature is visible at this scale. (right) An enlarged view of the region, marked by the black dot next to the wormhole, shows a reaction front at pore scale with clearly resolved pores and grains.

Another class of models are continuum scale or Darcy-scale models [43, 113, 114] in which pore space is represented by a continuous field. An underlying assumption in this approach is that a representative elementary volume (REV) can be defined within which the properties of pore space are assumed to be homogeneous and statistically representative of the larger system. This assumption allows the usage of continuous equations for fields like porosity, concentration, and Darcy velocity [109, 115]. We will discuss these models in detail in Sec. 3.2.2. Although these models are computationally efficient and widely used, their limitation lies in the absence of explicit pore space geometry, which makes them less accurate if the processes such as the competition between the individual pores for the available reactant become important.

A third approach to study reactive-transport problems is network models in which porous rock is represented either as a network of interconnected capillaries [37, 56, 66] or as spherical pores connected by cylindrical channels [116, 117]. Compared to Darcy scale models where the details of the pore space are smeared out, competition among pores at individual pore level is possible to capture in network models. Therefore, in problems where individual pore-level competition is important, network models are a suitable candidate. We will discuss them in detail in Sec. 3.2.3.

3.2 Dissolution models

3.2.1 Pore-scale models

These models account for the details of pore matrix where each point $\boldsymbol{r}$ in pore space belongs to either a solid phase or a fluid phase. Hence, the medium properties such as viscosity and diffusivity can be measured directly and independently. In addition, the complete flow physics is considered in these models, making them a method of choice where a detailed study of dissolving porous medium is required. Let us consider a porous medium where a reactive fluid of constant density ρ and viscosity μ is injected into the system. The solid grains are assumed to be impermeable to flow except if the grains are made of smaller pores through which the diffusion of ions is allowed [118]. Then the flow is governed by Navier-Stokes equation for incompressible fluid.

$$\nabla \cdot (\boldsymbol{u}\boldsymbol{u}) + \nabla(p/\rho) = \mu \nabla^2 \boldsymbol{u}; \qquad \nabla \cdot \boldsymbol{u} = 0 \tag{3.1}$$

Here on all pore-grain boundaries, a no-slip boundary condition is applied. In between the grains, the transport of aqueous species is governed by advection and diffusion. In advective transport, the species are carried away by bulk flow, while in diffusion, these species move from regions of higher concentration to regions of lower concentration due to random molecular motion. The transport equation in the pores is as follows:

$$\nabla \cdot (\boldsymbol{u} c_i) = D \nabla^2 c_i \tag{3.2}$$

where D is the diffusion coefficient. The transported reactant chemically dissolves the minerals at the pore-grain boundary, therefore the chemical reactions can be incorporated as a reactive boundary condition at the mineral surface as follows:

$$D(\boldsymbol{n} \cdot \nabla c_i)_S = -R(c_1, c_2, ...c_n) \tag{3.3}$$

where R is the reaction term and the subscript S indicates the mineral surface. For a single component reaction with linear kinetics, the reaction term can be expressed as kc_S where k is the reaction rate, and c_S is the reactant concentration at the mineral surface. Here, the diffusive flux of ions to the surface ($D(\boldsymbol{n} \cdot \nabla c)_S$), is balanced by their consumption through the chemical reaction (kc_S). Finally, the evolution of pore space can be calculated by utilizing reactive flux

$$c_{\text{sol}} \frac{\partial \boldsymbol{r}_s}{\partial t} = -\nu D(\boldsymbol{n} \cdot \nabla c)_S \boldsymbol{n} \tag{3.4}$$

where ν is the stoichiometric coefficient and c_{sol} is the molar concentration of the mineral in the consolidated rock, which is the inverse of the molar volume of the mineral ($c_{\text{sol}} = 1/v_m$). It is important to note that neither the flow (Eq. 3.1) nor the transport equation (Eq. 3.2) includes a time derivative. This time-independence is a consequence of the time-scale separation between the characteristic time over which changes in pore geometry occur and the flow and transport relaxation times. Using scaling analysis [119], it can be shown that in most of the field-related cases dissolution time scales are much larger than either the concentration or velocity

relaxation times.

The main computational problems in pore-scale modeling are, how to represent the mineral-fluid interface and how to update it as the mineral dissolves. To tackle them, three solution methodologies are proposed [120]. The first is the interface tracking approach which requires that the mineral–fluid interface is defined by a bounding curve (2D) or surface (3D). The time evolution of this bounding surface is governed by an equation of motion [91, 121–124]. The second is the interface reconstruction method in which evolving porosity field is tracked and the interface is constructed at each step from its spatial variation [125–127]. Both of these methods assume a sharp solid-fluid interface. The third approach—diffuse-interface models—assumes that the interface spans multiple computational grid points [128, 129]. The obtained governing equations can be solved numerically using different numerical methods including finite-volume, particle-tracking, and lattice Boltzmann methods.

One of the potential applications of the pore-scale modelling approach is to set up benchmark solutions for upscaled models such as Darcy models. Accordingly, several experimental studies have validated these models against the measurements of effluent concentration [79, 122, 130, 131], and the local dissolution of interface [108, 109, 132]. However, the system size in these experiments is limited to micro-scale; therefore the study of the large-scale dissolution patterns using these models remains of limited use.

3.2.2 Darcy-scale models

In this category of models, a porous media is represented by continuous fields such as porosity $\phi(\boldsymbol{r}, t)$—the fraction of void space—and permeability K, which can vary in space $\boldsymbol{r}$ and time t. Consequently, the flow physics can be modelled using a continuum approach where all the fields including concentrations of different aqueous species and velocity field can evolve as a result of dissolution.

In a saturated porous medium, the flow is governed by Darcy's law, formulated by *Henry Darcy* (1803-1858) based on the experiments. It dictates that the Darcy velocity $\boldsymbol{v}$ ($= Q/A$, where Q is volumetric flow rate, and A is cross-sectional area) in a porous medium is related to the applied pressure gradient ∇p, the permeability of the medium, and the viscosity of the fluid μ (Eq. 3.5):

$$\boldsymbol{v} = -\frac{K}{\mu}\nabla p \tag{3.5}$$

This needs to be supplemented by the incompressibility condition

$$\nabla \cdot \boldsymbol{v} = 0 \tag{3.6}$$

The pore matrix can be highly heterogeneous and anisotropic, with properties that vary locally. In this model, we assume that porosity $\phi(X, t)$ is the only property which contains the information of the pore-matrix, and the permeability field K can be derived from the porosity field. However, there is no universal relationship between K and $\phi(X, t)$ and the dependence of K over ϕ could be different for

different porous medium. We assume a general expression of $K - \phi$ dependence, similar to the Kozeny-Carman [115] relationship as follows:

$$K = K_0 \frac{\phi^n}{(1-\phi)^2} \tag{3.7}$$

where K_0 is a constant, and for $n = 3$, we recover the classic Kozeny-Carman equation, but in general, a different value of n can be used. As mentioned earlier, the transport is governed by advection and diffusion. However, microscopic diffusion is further enhanced by the presence of solid grains, which act as obstacles within the pore matrix. Even small diffusive displacements can cause a molecule to jump between streamlines, redirecting it along an entirely different path than a neighboring molecule. This mechanism is known as dispersion and can be expressed as a tensor (dispersion tensor, $\underline{\underline{\boldsymbol{D}}}$), which depends on the flow rate and porosity of the medium. Considering these transport mechanisms, the governing equation can be written as follows:

$$\nabla \cdot (\underline{\underline{\boldsymbol{D}}} \nabla c_i) - \boldsymbol{v} \cdot \nabla c_i + R(c_1, c_2, ..., c_n) = 0 \tag{3.8}$$

Here, the reaction term R, unlike the pore scale models, depends not only on reaction rate k but also on the specific reactive surface area $s(\phi)$ in a pore space. This distinction arises because, at the REV scale, the actual pore geometry is not explicitly resolved, necessitating introduction of available reactive surface area per unit volume [120]. For single-component linear chemical reactions controlled by the reactant concentration, R can be given as follows:

$$R = -ks(\phi)c \tag{3.9}$$

here, $R < 0$ represents the chemical erosion of the mineral. For specific reactive surface area $s(\phi)$, a so-called sugar-lump model [74] is often used.

$$s(\phi) = 4s_0\phi^m(1-\phi)^n \tag{3.10}$$

where s_0 is a constant. Reflecting the fact that at low porosity, dissolution primarily occurs through pore expansion, increasing the reactive surface area. In contrast, at high ϕ, dissolution is better described as grain shrinkage, which reduces the reactive surface area. At both extremes when there is no surface area exposed to reactive fluid ($\phi = 0$) or the system is completely dissolved ($\phi = 1$), s can be assumed negligible (i.e. $s \to 0$). Finally, the system of equations can be closed by introducing a porosity evolution law

$$c_{\text{sol}} \frac{\partial \phi}{\partial t} = -\nu R \tag{3.11}$$

As we argued before, the time scales of flow and transport are much smaller compared to porosity evolution time scale. Therefore, we dropped the time derivatives in flow (Eq. 3.6) and transport (Eq. 3.8) equations. This ensures the stationarity of the flow and concentration fields while allowing the porosity to evolve over time (Eq. 3.11).

Dimensionless numbers in Darcy models

The dimensionless numbers in Darcy models are derived from non-dimensionlization of the transport equation (Eq. 3.8). The advantage of the dimensionless form of a partial differential equation (PDE) is a direct comparison of the relative importance of physical processes represented by that PDE. For that purpose, let us consider a 1D porous medium with characteristic length scale l_0, Darcy velocity (v_0), and specific reactive surface area (s_0). A reactant of concentration c_0 is injected into the system. The fields and the spatial coordinates can be scaled as follows

$$x^* = \frac{x}{l_0}; c^* = \frac{c}{c_0}; v^* = \frac{v}{v_0}; s^* = \frac{s}{s_0} \tag{3.12}$$

Now, for simplicity, by using a 1D steady-state version of Eq. 3.8 with reaction term from Eq. 3.9, the dimensionless form of the transport equation can be written as follows:

$$\frac{Dc_0}{l_0^2}\frac{\partial^2 c^*}{\partial x^{*2}} - v_0 c_0 \frac{v^*}{l_0}\frac{\partial c^*}{\partial x^*} - k s^* s_0 c^* c_0 = 0 \tag{3.13}$$

for which we get:

$$\frac{1}{\mathrm{Pe}}\frac{\partial^2 c^*}{\partial x^{*2}} - v^*\frac{\partial c^*}{\partial x^*} - \mathrm{Da}(l_0, 1/s_0) s^* c^* = 0 \tag{3.14}$$

where, the expressions, $\mathrm{Da}(l_0, 1/s_0) = k s_0 l_0 / v_0$ and $\mathrm{Pe} = v_0 l_0 / D$, are analogous to definitions 2.1 and 2.2, respectively.

The study of reactive transport problems using Darcy scale models is a well-established approach for which various commercial and open-source codes are available. General purpose codes were first developed 30 years ago [133–135], and have been under constant development ever since. Some notable examples are PFLOTRAN, CrunchFlow [136], and PorousFoam [103]. These codes are not only able to simulate multiple component chemical reactions but also able to solve field scale problems using supercomputers. However, dissolution is a highly nonlinear process where reactions and transport occur at the microscale, while large-scale dissolution patterns emerge at the macroscale. In Darcy-scale models, the porous medium is represented by averaged continuous properties, neglecting key micro-scale processes. This includes local concentration gradients, the precise evolution of streamlines at pore intersections, and their role in enhancing or suppressing mixing. Such oversimplifications make Darcy-scale models inadequate for capturing the intricate coupling between micro- and macro-scale dynamics, which is crucial for understanding the growth and evolution of large-scale dissolution patterns.

3.2.3 Pore network models

These models introduce a simplified representation of a porous material, either as a network of interconnected capillaries [37, 56, 66, 137, 138] or as spherical pore bodies connected by cylindrical throats [116, 139–143], offering a compromise between the computational accuracy characterizing the pore-scale models and the ability to tackle large-scale problems, which are the advantages of Darcy-scale methods.

Pore-network models (PNM) allow for control of the pore architecture (diameters, lengths, connectivity), tuning it to represent different rocks. In dissolution problems, pore network models are able to correctly reproduce the competition between the individual pores for the reactant flux, which leads to a successful representation of the variety of spontaneously formed dissolution patterns such as wormholes [66, 144], including their structure and advancement rate, permeability evolution, and the non-monotonic relationship between injection rate and fluid volume required for breakthrough [37, 38, 66]. They were also successfully used to analyze the link between pore-scale features and large-scale morphologies [56, 137].

In this section, we will discuss PNM in which the pore-space of a rock is represented using a network of interconnected cylindrical tubes [37, 66, 137, 138] which are broadened by dissolution. The intersections of the tubes are nodes in the network, which are assumed to be negligible in volume and only play a role in the mixing and distribution of reactant concentrations while the reaction takes place in the tubes. Fig. 3.2 shows a representation of the extracted network from a quasi two-dimensional porous medium. The lines represent cylindrical tubes (pores) to which diameters can be assigned using a diameter distribution with given mean d_0 and standard deviation σ, while the red dots mark nodes.

Pore networks of a porous medium can be constructed either directly from micro-CT images of it [145] or by assigning statistical properties of the medium to a random network [66]. However, for simplicity, a regular pore network is often preferred. For example, Hoefner and Fogler [37], and Fredd and Fogler [38] used a hexagonal lattice-based network for dissolution modelling, while Roded et al. [137] and Roded et al. [56] used a square lattice-based network. Sharma et al. [138] used a rhombic lattice based network—essentially a square lattice rotated at 45°—to study intersection mixing effects. Fig. 3.3 shows different types of regular pore networks where lines are capillaries and nodes are red dots.

In this model, the injected fluid is assumed to be incompressible, and the flow in each pore is considered to be laminar and fully developed. For a pore (ij), joining nodes i and j, the volumetric flow rate (q_{ij}) then is given by Hagen-Poisueille equation

$$q_{ij} = -\frac{\pi d_{ij}^4}{128\mu l_0}(p_i - p_j) \tag{3.15}$$

where d_{ij} is the diameter of pore (ij), p_i is the pressure at node i, and μ is the dynamic viscosity of the fluid. The term $\pi d_{ij}^4/128\mu l_0$ in Eq. (3.15) represents the hydraulic conductance of a pore (ij) which increases with time as the pore grows. Finally, the flow conservation condition is applied at each node.

$$\sum_j q_{ij} = 0 \tag{3.16}$$

where the summation in Eq. (3.16) is taken over all the neighboring nodes directly connected to node j. As a result, we obtain a system of sparse linear algebraic equations for pressure, which, after solving, will give the value of pressure at each

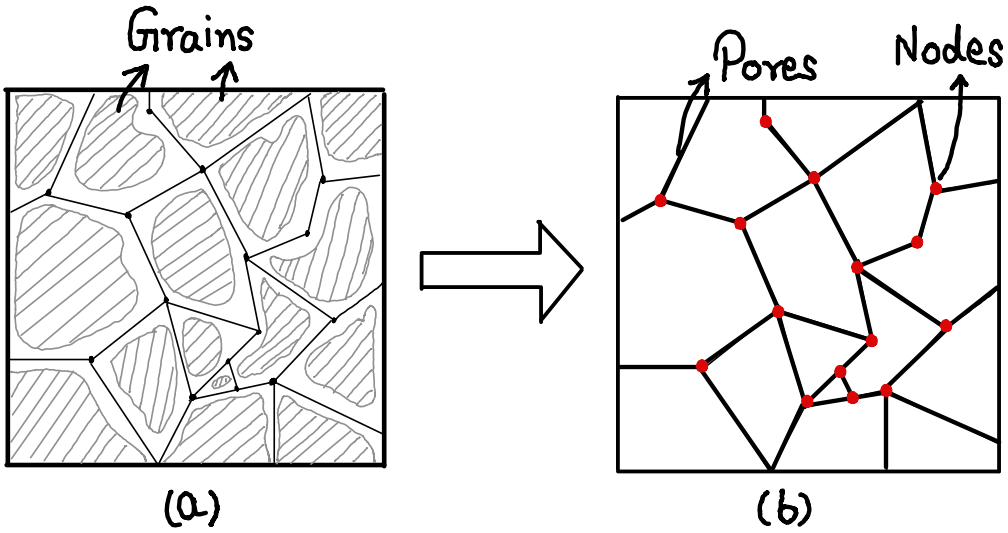

Figure 3.2: (a) A 2D representation of a porous medium with pores and grains. The grey blobs with dashed lines represent the grains, and the fitted lines represent the pores. (b) The extracted pore network with nodes as red dots where mixing takes place. In this representation, it is assumed that pore-space can be fully resolved in terms of pores ($\phi = 1$) and grains ($\phi = 0$) and there are no semi-porous objects.

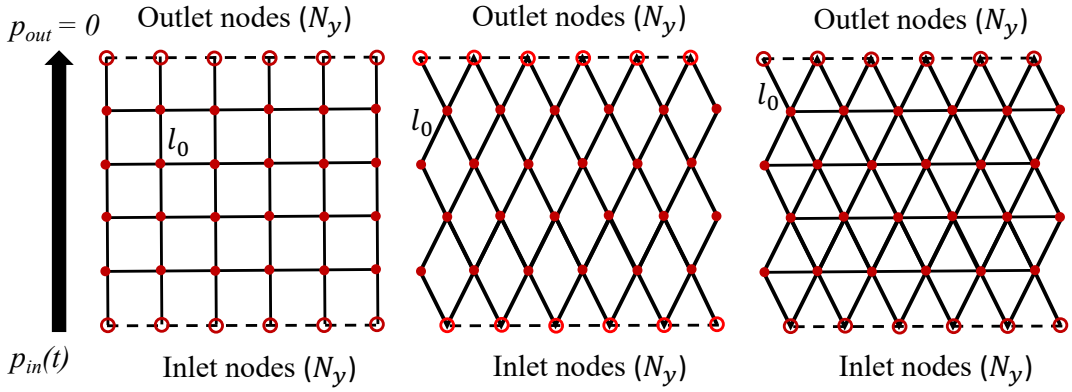

Figure 3.3: Different type of regular 2D networks: (left) square lattice with 4 coordination number, (middle) rhombic lattice also 4 coordination number, and (right) hexagonal lattice with 6 neighboring nodes. In the networks, lines are the pores or capillaries, and red dots are volumeless nodes where mixing takes place. Each pore has a fixed length, i.e. lattice constant (l_0) of the network, and a diameter d_{ij}. The mean flow direction is shown by the arrow, and in the lateral direction, a periodic boundary condition is applied.

node.

We now can introduce reactant into the system through inlet face by applying fixed concentration boundary conditions ($c = c_{\text{in}}$). The reactive flux, defined as the num-

ber of reactant particles consumed in a unit pore surface in unit time, is following:

$$R = -kc_w \tag{3.17}$$

where c_w is the reactant concentration available at the pore surface and k, as mentioned earlier in Eq. 2.1, is the reaction rate. In addition, to participate in the reaction, the reactant particles first need to diffuse from bulk toward the surface of the pore. Assuming a steady state bulk concentration (c) and surface concentration (c_w), the diffusive flux can be expressed by

$$J = -\frac{D\mathrm{Sh}}{d}(c - c_w) \tag{3.18}$$

where Sh is a dimensionless mass transfer coefficient known as Sherwood number [146, 147]. The bulk concentration c is calculated by taking a flow-weighted average of the concentration field over the cross-section of a pore. Finally, the wall concentration c_w can be expressed in terms of bulk concentration c by equating both diffusive and reactive flux, which leads to:

$$c_w = \frac{c}{1 + \frac{kd}{D\mathrm{Sh}}} \tag{3.19}$$

Using this expression, we can now write the final expression of kinetic rate law in terms of mean bulk concentration for a pore (ij)

$$R = -\frac{k}{1 + \frac{kd_{ij}}{D\mathrm{Sh}}}c \equiv -k_{\mathrm{eff}}(d_{ij})c \tag{3.20}$$

The parameter $g = kd_{ij}/D\mathrm{Sh}$ in the denominator of Eq. (3.20) accounts for the hindering effect of diffusion on the dissolution rate, particularly pronounced in wider pores. As a result, the pore surfaces tend to react with a slower effective rate, k_{eff}, which includes the transverse diffusion effect. For narrow pores or low reaction rates ($g \ll 1$), dissolution is reaction-limited ($k_{\mathrm{eff}} \approx k$), and diffusion is fast enough to maintain the uniform concentration profile along the diameter of the pore. When the pores are large or reaction rates are high, then dissolution becomes transport-limited ($g \gg 1$) and the effective reaction rate is controlled by diffusion. The Sherwood number itself depends on kd/D, but the variation is relatively small [147], bounded by two asymptotic limits: high reaction rates (transport limit) and low reaction rates (reaction limit). For circular cross section, these limits correspond to $\mathrm{Sh} = 4.861$ and $\mathrm{Sh} = 5.385$, respectively [148]. In practice, Sh is often assumed to be approximated by a constant (e.g. $\mathrm{Sh} = 5$ is used by Sharma et al. [138])

The reactant concentration decays along the length of the pore due to its consumption at pore walls, which can be obtained from mass balance [66]

$$q_{ij}\frac{dc}{dx} = -\pi d_{ij}k_{\mathrm{eff}}c \tag{3.21}$$

where (x) is the axial coordinate and diffusion along the axial direction is neglected.

By solving Eq. (3.20) for a constant diameter, we obtain an expression of concentration decay along the length of the pore (Eq. 3.22).

$$c(x) = c_{ij}^{\text{in}} \exp(-\frac{\pi d_{ij} k_{\text{eff}}}{q_{ij}} x) \tag{3.22}$$

here c_{ij}^{in} is the concentration at the inlet of the pore ij. Eq. 3.22 can also be solved for the decay of concentration along the whole length l_{ij} for pore ij with a uniform diameter, which yields

$$c_{ij}^{\text{out}} = c_{ij}^{\text{in}} \exp(-\frac{\pi d_{ij} k_{\text{eff}}}{q_{ij}} l_0) \tag{3.23}$$

These equations need to be supplemented with mixing rules at all the pore intersections. For mixing of concentrations at intersections, it is usually assumed that incoming reactant concentrations have enough residence time to mix completely and the final outgoing concentration is calculated by taking a flux-weighted average of incoming concentrations. More specifically, for a node i with incoming concentrations c_{ij}^{out} from pore-outlets (j), the expression of outgoing concentration c_{ij}^{in} to pore inlets (k) is:

$$c_{ik}^{\text{in}} = (\sum_j q_{ji} c_{ji}^{\text{out}})/(\sum_j q_{ji}) \tag{3.24}$$

where, for a node i, the sum is taken over all the neighbouring pores (ij) connected to that node (i), which are bringing flow to the node while ik refers to the one of the outgoing pores into which the final concentration given by Eq. (3.24) is entering. By solving Eq. (3.23) and (3.24) together, we again obtain a system of sparse linear equations which is solved for the concentration at the intersections.

To close the system of equations, the final element of this model is the erosion equation which governs the evolution of pore diameters [66, 138].

$$\partial_t (d_{ij}/2) = \frac{k_{\text{eff}}}{\nu c_{\text{sol}}} c \tag{3.25}$$

As we argued before in Darcy and pore-scale models, the time-scales of dissolution are significantly larger. Therefore, the time-scales of flow and transport can be neglected [66]. This assumption is crucial for the network model to work because in solving the transport equations, the time-dependent terms $(\partial_t c)$ are neglected, and a quasi-static approximation is adopted. Next, by using Eq. (3.25), one can obtain the volume of material removed from the walls of the pores with diameter d over time Δt.

$$\Delta V = \frac{\pi d k_{eff} \Delta t}{\nu c_{sol}} \int_0^l c(z) dz = \Delta t q \frac{c_0}{c_{sol} \nu} (1 - \exp(-\pi d k_{eff} l / q)) \tag{3.26}$$

Within the network model, it is assumed that a pore grows in diameter uniformly along the length and maintains its cylindrical shape [37, 38]. Hence, the above

mentioned change in volume corresponds to an increase in the pore diameter by

$$\Delta d = \frac{\Delta V}{\pi dl} = \frac{2\Delta t q}{\pi dl}\frac{c_0}{c_{sol}\nu}(1 - \exp(-\pi d k_{eff} l/q)) \tag{3.27}$$

For more details about the implementation of this network model, we refer the reader to Roded et al. [56], Budek and Szymczak [66] and Sharma et al. [138].

Dimensionless numbers in pore network models

In this network model, instead of the traditional approach of introducing Da and Pe, we define two dimensionless numbers G and $\mathrm{Da}_{\mathrm{eff}}$, which are derived at pore scale using a single tube model [66], and account for the combined effect of flow rate, reaction rate, and transverse diffusion. As given in Eq. (3.20), parameter $g(d_{ij})$, at an individual pore level, accounts for the relative strength of reaction and transverse diffusion. We can define a characteristic value of g at the sample level in the following manner:

$$G = \frac{k d_0}{D\mathrm{Sh}} \tag{3.28}$$

Here, G, which plays a similar role to Thiele's module in chemical engineering [149], characterizes the hindering effect of the diffusive transport on the dissolution rate throughout the sample. Note that d_0 in Eq. (3.28) is the average diameter in the system.

Another important parameter in our model is the effective Damköhler number ($\mathrm{Da}_{\mathrm{eff}}$) which is related to the exponent in Eq. 3.23.

$$\mathrm{Da}_{\mathrm{eff}} = \frac{\pi d_0 k_{\mathrm{eff}} l_0}{q_0} = \frac{\pi d_0 k l_0}{q_0(1+G)} \tag{3.29}$$

where q_0 is a characteristic initial volumetric flux in a pore. It is noteworthy to mention that $\mathrm{Da}_{\mathrm{eff}}$ depends on G and, therefore, accounts for transverse diffusion in the pore. Budek and Szymczak [66] has shown that $\mathrm{Da}_{\mathrm{eff}}$ has stronger influence on the shape of dissolution patterns than G.

Note that this definition (Eq. 3.29) is consistent with our earlier definitions of the Damköhler number. Substitution of $q_0 = \pi d_0^2 \langle v_0 \rangle / 4$ leads to $\mathrm{Da}_{\mathrm{eff}} = k_{\mathrm{eff}} l_0 / d_0 \langle v_0 \rangle$ which is of the same form as Eq. 2.1, only with k replaced by the effective reaction rate. Finally, we can define the dimensionless time $\hat{t}$ which is given by

$$\hat{t} = \frac{2k\gamma t}{d_0} \tag{3.30}$$

where $\gamma = c_0/\nu c_{\mathrm{sol}}$ is the acid capacity number, which is defined as the ratio of number of molecules of reactant per unit volume of incoming fluid to the number of molecules per unit volume of a mineral.

Concluding this chapter, we introduced different type of dissolution models, ranging from micro-scale models which utilize the information of pore space, to continuum models such as Darcy models in which the medium properties are characterized by

continuous fields such as porosity and permeability. These models are highly accurate within their specific application ranges. However, they struggle to bridge micro-scale processes, such as pore-scale mixing, with large-scale dissolution. For example, while pore-scale models effectively capture detailed physics, they are restricted to very small systems. In contrast, Darcy models are well-suited for field-scale problems but lack mechanisms to incorporate micro-scale processes. The alternative is the third model we discussed (i.e. network model) in which the pore-space is represented as interconnected capillaries. These models are able to capture the pore-scale physics without compromising the size of the system. Therefore, in Ch. 6, we will take advantage of network models in investigating the influence of pore-scale mixing rules on network scale dissolution patterns.

Chapter 4

Pore merging and flow focusing: Comparative study of undissolved and karstified limestone based on micro-tomography

There is no royal road to geometry

Euclid

4.1 Introduction

Building on the previous chapters that reviewed the dynamics of dissolution finger formation based on past studies, this chapter and the following ones present the original research of this thesis. The results of this study have been published [150].

Dissolution leads to permanent changes in the rock's pore space, either increasing or decreasing system heterogeneity. Penetration lengths comparable to the system size result in uniform dissolution, which homogenizes the system, while shorter penetration lengths lead to channel formation that increases heterogeneity. The mechanisms behind the formation of dissolution patterns are usually explored through laboratory experiments, where reactions occur faster than in natural dissolution processes. Pore-space changes in such studies are often assessed using micro-tomography imaging [48, 53, 67–69, 71], allowing for the quantification of modifications in rock structure, including variations in reactive surface area, connectivity, and tortuosity, and linking these changes to reaction progress and the evolution of flow paths in the sample.

On the contrary, in case of natural dissolution much less is known about the changes of pore geometry of a rock (see, however, [151, 152]). The pore geometries could evolve through different mechanisms such as pore-enlarging, merging, or a combination of both. In this chapter, we will argue that this is indeed the case. This

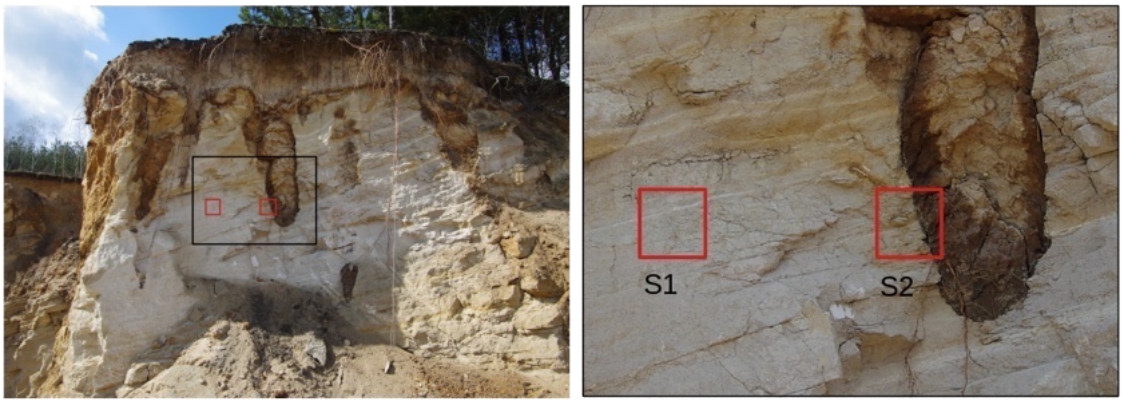

Figure 4.1: Solution pipes in Smerdyna quarry with locations of samples S1 and S2.

study [150] is among the first original works that investigate the natural dissolution-induced changes in pore geometry using the collected limestone samples from karstified area. We will focus on different mechanisms, through which pore-geometry can evolve, by performing a comparative study of undissolved and karstified limestone samples. In addition, we will explore changes in the geometrical properties of pore space.

To investigate the influence of natural dissolution over a rock, we will perform a comparative study between two samples. One of them is collected from a karstified area, where, due to natural dissolution, an intense flow focusing took place, resulting in the formation of solution pipes which are freshly exposed due to mining activity [153, 154] (see Fig. 4.1). The presence of spontaneous piping indicates that the rock in the immediate vicinity of the pipes has been exposed to the aggressive flow, leading to the chemical erosion of the rock matrix while the rest of the rock masses between the pipes remained largely unaffected by karstification. The second sample belongs to the unkarstified area. Details of these samples will be discussed in Sec. 4.2.

Comparison of these samples, provided us a unique opportunity to characterize the changes in pore geometry induced by natural dissolution. The host rock has around 40% porosity, and pore-space is very irregular with extensively interconnected pores, which means the merging of pores might play an important role in pore-space evolution. The irregular geometry and lack of distinct pore-throats complicate the usage of conventional tools for pore geometry analysis, such as identifying individual pores and throats, and the subsequent calculation of pore-size distributions. Consequently, an alternative approach is required for the characterization of such a geometry lacking well-separated pore structures. For this purpose, we have adopted the geometrical and topological characteristics developed for bone research [80, 81] such as local thickness, ellipsoid factor, and connectivity, which will be introduced in Sec. 4.3. Furthermore, we have also integrated the data analysis of micro-tomography images with simple analytical models, which enabled us to quantify the impact of pore-merging and inhomogeneous dissolution in the natural dissolution of the analyzed samples. The results are discussed in Sec. 4.4

4.2 Materials and methods

4.2.1 Collection of samples

The study site is near Smerdyna, Poland, approximately 12 km northeast of Staszów. The mining activities provide extensive exposures of mid-Miocene calcarenite formations characterized by intense epikarst features. The carbonate content in calcarenites of Chmielnik Formation around Smerdyna is, on average, more than 90% [153]. These calcarenites are covered by uncemented glacial till up to 5 m, which serves as the source material for filling solution pipes [153, 155].

Two samples of Miocene calcarenites, referred to as S1 and S2, were obtained from a fresh exposure within one of the quarries, where extensive epikarst development—mainly in the form of solution pipes which can reach a diameter of about 0.5 m and length up to 6 m (*cf.* Fig. 4.1)—is observed on the open cut walls. The samples are taken along the axis perpendicular to the pipe in a cylindrical shape with a diameter of 2.2 cm and length of 2.4 cm. Sample S1 was collected from a location of approximately 1.5 m away from the solution pipe, while sample S2 was extracted directly from the side of a long-and-wide pipe such that the top of the cylinder aligned with the surface of the pipe.

Visual examination of sample S2 reveals it to be more porous and much softer than S1, almost at the edge of crumbling. This difference is corroborated by the porosity measurements conducted using the hydrostatic method, ISO 5017, which gives the porosity values of sample S1 at $\phi_1 = 39.35 \pm 0.8\%$ and of S2 at $\phi_2 = 50.7 \pm 0.6\%$. The observed porosity difference is likely attributed to the dissolution of sample S2 by CO_2-saturated water, which was focused in the pipe. Consequently, we have the opportunity to observe the difference between a naturally dissolved sample, S2, and a relatively undissolved sample, S1, originating from the same host rock.

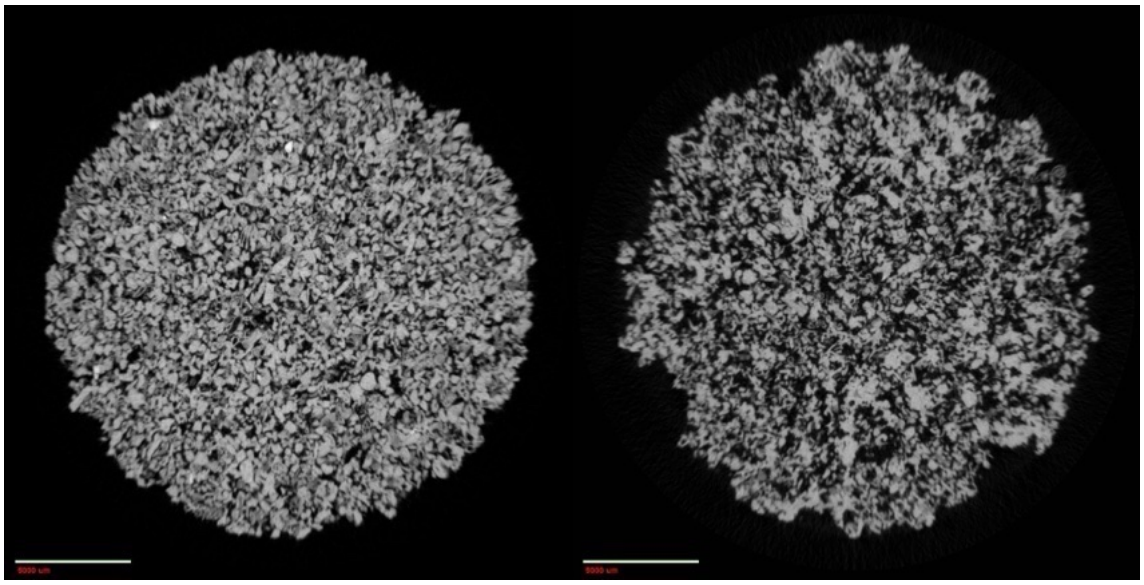

Figure 4.2: The tomographic images of the undissolved sample (S1, left) and naturally dissolved sample (S2, right) [150]

4.2.2 X-ray microtomography

The collected samples were scanned at 26 µm resolution using an Xradia MicroXCT-200 X-ray imaging system at the Institute of Paleobiology, Polish Academy of Sciences. The obtained scans were of 1024×1024 pixels with 648 slices, each in 16-bit grayscale format.

An image processing software, ImageJ [156], is used to analyze the obtained X-ray microtomgoraphy scans. Fig. 4.2 shows a single slice of obtained scans for both samples, S1 and S2. To facilitate comparison between the samples, a cubic region of interest (ROI) was selected in each, measuring 5064 voxels corresponding to 13.2 mm^3 in size. Furthermore, the image stacks were converted to 8-bit images to reduce the data size for computational purposes. Finally, for segmentation process, a grayscale threshold value is chosen by tuning it to match the experimentally measured porosity values of the respective samples. The variation of porosity within the cores remained relatively small, within 3%, and no macroscopic porosity gradients were observed. Notably, the scans (as shown in Fig. 4.2) confirm a considerably rougher appearance of naturally dissolved sample, S2. However, the objective of this study is to quantitatively characterize these differences to gain insights into the dissolution process.

4.2.3 Numerically eroded sample

In order to investigate the similarities and differences between natural dissolution and homogeneous dissolution, we have created a numerically generated pore geometry from segmented undissolved sample, S1. The segmented geometry is numerically dissolved by removing pixels randomly from pores/grains boundaries with probability $\mathbb{P}$ which is tuned to ensure a total porosity increment of 11.35%, precisely matching the difference between the sample S1 and S2. Following numerical erosion, we have applied a median filter with a radius of one voxel to smooth out the boundaries between pores and grains. Since each voxel at pore-grain boundary has same probability of removal, such procedure mimics a fully homogeneous dissolution of rock. By construction, the porosity of the resulting geometry (hereafter referred to as sample S3) matches that of sample S2. Moreover, to maintain consistency, we have applied an identical median filter to the original geometries of both S1 and S2.

4.3 Pore space characterization

In both collected samples, the pore space has highly irregular geometry which is comprised of a single connected component without distinct pore bodies and throats. This makes it difficult to apply standard tools for pore-space analysis such as identification of individual pores and subsequent calculation of pore size distribution. The division of the pore space into individual pores becomes somewhat arbitrary in such cases, largely reliant on the parameters utilized in the pore-segmentation algorithm (watershedding) [157]. The alternative, in such cases, is to employ continuous measures of pore (and grain) space, such as local-thickness and ellipsoid factors [80, 81], which are defined at each point in the sample. However, for samples

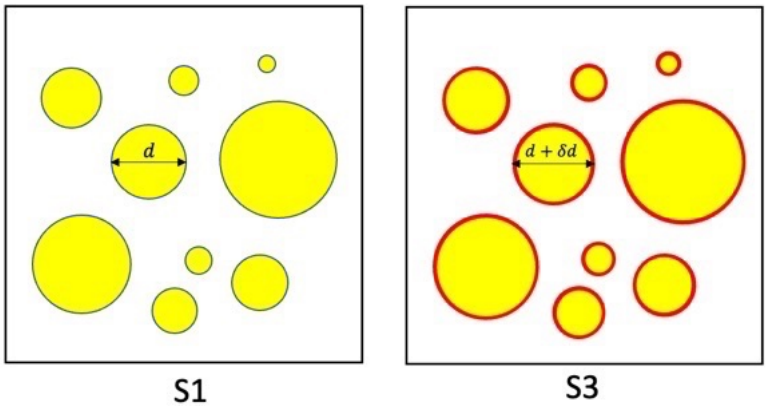

Figure 4.3: Numerical erosion of the samples: starting from the undissolved sample (S1, with pores depicted in yellow and rock matrix - in white) we produce a homogeneously dissolved one (S3) by removing a fraction of the voxels at pore-grain boundaries and smoothing it using median filter (marked in red in the figure) [150]

with smaller porosity, a standard pore-network extraction algorithm —capable of identifying pore bodies and throats—combined with mercury intrusion porosimetry remains a viable alternative [71, 158].

4.3.1 Local thickness

One of the most important measures to characterize such an interconnected pore space is the local thickness. It is defined locally at each point by fitting the largest possible sphere within the pore, containing that point, as depicted in Fig. 4.4 [80, 81]. The diameter of this sphere is the local thickness at that point. It is important to note that the local thickness differs from pore diameter and pore throat size, providing an independent measure of the pore extent.

In the context of digital rocks physics, the concept of local thickness has been utilized in a variety of applications: in multiphase flow problems to characterize the pore-scale configurations of fluids [159, 160], in the characterization of pore space constrictions to interpret mercury intrusion porosimetry experiments [161], and-of particular relevance in present context-to quantify the opening of pore spaces during the dissolution experiments [162].

In this work, to calculate the local thickness (as well as other measures discussed below), we used an image processing algorithm, BoneJ, developed for trabecular bone analysis and implemented in ImageJ [163]. In fact, the pore space in trabecular bone exhibits numerous similarities with the extended and irregular pore space of analyzed rock samples. Notably, the concept of local thickness can also be employed for a grain phase, following an analogous methodology to that used for the thickness of pore space, by looking for the largest sphere fitting in the grain phase only, which encompasses the point of measurement.

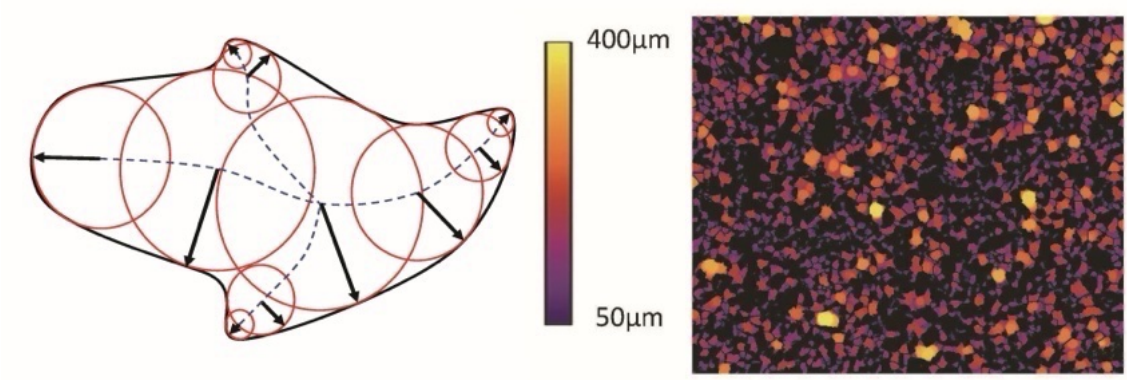

Figure 4.4: Left: Schematic illustration of a local thickness measurement. Right: thickness map of a cross-section of sample S1 [150].

4.3.2 Ellipsoid factor and Flinn diagram

Pore space or matrix can be further characterized using the local thickness method by incorporating additional geometric information about the surrounding space at a specific point of interest. This is achieved locally by fitting a maximum ellipsoid instead of a sphere. We refer the reader to Doube [164] for a comprehensive explanation. For an ellipsoid with axes $A \leq B \leq C$, the ellipsoid factor (EF) is defined as the difference in the axes ratios:

$$EF = \frac{A}{B} - \frac{B}{C},$$

This factor, EF, distinguishes between oblate (pancake-like) shape, indicated by $A/B \to 0$ and $B/C \to 1$, and prolate (cigar-like) shapes, indicated by $A/B \to 1$ and $B/C \to 0$. For illustration purposes, we employ the Flinn diagram [164, 165], a two-dimensional plot with coordinates of A/B versus B/C.

4.3.3 Connectivity

The interconnectedness of the pore space can be measured using connectivity $\beta 1$ which, in the context of a graph or a network, corresponds to the maximum number of edges (links) that can be removed without disconnecting the structure into separate parts [166]. This measure is a topological invariant of pore space, hence it is preserved under deformations as long as they do not involve cutting of the grains or filling the holes. Euler-characteristic χ is another well-known topological invariant that relates to connectivity by the Euler-Poincare formula, which for 3D geometry is expressed as:

$$\chi = \beta_0 - \beta_1 + \beta_2,$$

where β_0 and β_2 are zeroth and second Betti numbers, respectively [167]. The first Betti number β_1 corresponds to connectivity. In the context of rock matrix, β_0 can be interpreted as the number of connected pieces or components of the rock, typically equal to unity. Conversely, β_2 indicates the number of cavities in the rock [166] which may be greater than zero in the presence of closed porosity.

BoneJ calculates connectivity by relating it to these Euler characteristics. To do so, it purifies the sample first by filling all closed pores and therefore setting $\beta_2 = 0$.

4.3.4 Permeability, tortuosity and velocity distribution

We have also employed computational modelling of the flow field through the ROI of our samples to supplement the analysis of the geometric characterization of the pore space. Lattice Boltzmann method, implemented in Palabos library [168], is used to solve the Stokes equation within the pore space which is obtained from the segmented tomographic images. The absolute permeability of the sample is calculated by integrating the flow velocity across the cross-section. Additionally, tortuosity is calculated as:

$$\tau = \frac{\langle u \rangle}{\langle u_x \rangle}, \tag{4.1}$$

where $\langle u \rangle$ is the average magnitude of the Darcy velocity over the entire sample volume and $\langle u_x \rangle$ is the volumetric average of its component along the macroscopic flow direction [169]. Furthermore, we analyze the velocity distributions for both samples and compare them.

4.4 Results and Discussions

In this comparative study, we analyze the pore geometry by comparing the ROI of the samples S1 and S2, and the numerically eroded sample S3, which serves as a reference for homogeneous dissolution.

As previously mentioned, the samples are highly porous (∼40% primary porosity) even before dissolution, exhibiting a complex and highly irregular pore structure with high reactive surface area. In the segmented images, a direct count of sides of voxels on the pore-grain boundaries gives an estimation of a specific surface area, s_1, around 10 mm^2/mm^3 which is comparatively larger than the other limestones of similar porosity [74]. Given the high porosity and reactive surface area of a sample, even uniform dissolution may induce significant changes in pore space topology, as some walls between pores will be completely dissolved. Consequently, we anticipate that pore merging might be an important process in Smerdyna limestone. Indeed, the estimated reactive surface area of the dissolved sample is approximately ($s_2 \approx 9.1$ mm^2/mm^3) which is around 10% smaller compared to s_1. The decrease of reactive surface area, s, during dissolution, indicates that pore merging plays a significant role in the dissolution process, which is fundamentally different from the dissolution process of packed limestones where the dilation of the pores is a dominating process and no merging takes place.

Fig. 4.5 illustrates the distribution of measured local thickness for samples S1, S2, and S3, representing the number of voxels associated with a specific local thickness. BoneJ, a plugin of ImageJ, is used to obtain the distributions from the segmented images, and a local Gaussian filter is applied to smooth out the distribution curves. The smoothing of the curves removes the artificial variability in data resulting from

the voxelization effects in small pores.

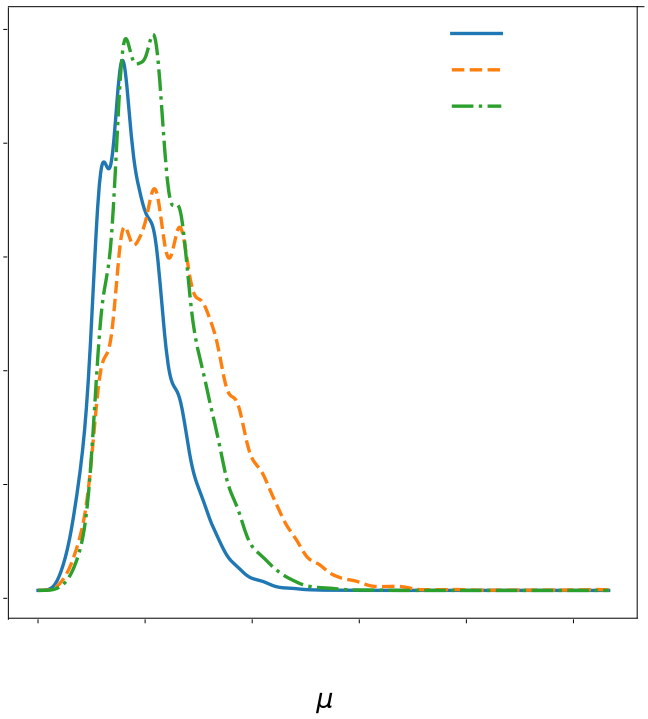

Figure 4.5: Thickness distribution for samples S1, S2 and S3. The counts correspond to the number of voxels with thickness in the range $(b-\frac{\Delta b}{2}, b+\frac{\Delta b}{2})$ with the bin size $\Delta b = 0.26$ µm [150].

We observed that the distributions of S2 and S3 overlap for small local thicknesses, below 100 µm. When interpreting these data, it is important to note that S3 has been obtained from the fully uniform dissolution of S1 by the removal of a layer with uniform thickness across the entire rock matrix. The overlap of local thickness distributions, $P_{th}(b)$, for small b values indicates that during the natural dissolution, the smallest pores grow in size in an approximately uniform manner. Conversely, the tail of the thickness distribution $P_{th}(b)$, corresponding to larger pores, for dissolved sample S2 is significantly higher, not only compared to undissolved sample S1 but also with respect to the uniformly eroded sample S3. This suggests that the majority of the dissolution process has been focused on the largest pore spaces.

As previously noted, no macroscopic porosity gradients were observed in the dissolved sample, leading us to the conclusion that the penetration length of the reactant was significantly larger than the sample size. This is commonly referred to as the uniform dissolution regime [37, 43, 44, 53, 170], in the sense that the dissolution takes place throughout the rock matrix rather than being localized near the inlet of a reactive fluid. However, if the dissolution was truly uniform across the pore space, then the statistical characteristics of the naturally dissolved sample (S2) should resemble the characteristics of the numerically dissolved sample (S3). This is clearly not the case, as evidenced by the preferential dissolution of the largest pore spaces.

It is important to mention that this phenomenon, characterized by the relatively greater dissolution of larger pore structures, is not related to the concept of pore-controlled solubility [171, 172]. Indeed, the solubility dependence on pore size arises from the interphase surface tension.

$$c(r) = c_\infty e^{\nu\gamma/N_A k_B T r}$$

where γ is the interfacial energy, r is the pore size, N_A is Avogadro's number, T is the temperature, ν is the mineral molar volume and c_∞ is the bulk solubility. Nonetheless, in the case of calcite, the interfacial energy significantly contributes to the solubility for pores smaller than 1µm [173], well below the size range considered here.

Instead, we draw a connection between our observations and the experimental findings of Menke et al. [53]. In their study, they conducted a series of dissolution experiments on limestone samples by dissolving them in a uniform dissolution regime using CO_2-saturated brine. They found that the heterogeneity of the rock facilitates the formation of preferential flow paths which focus the majority of the reactant on a relatively limited portion of the surface of the rock. Since the permeability of the pore structures increases significantly with pore size (as indicated by the local thickness), we anticipate that these preferential pathways primarily involve the regions with high thickness, which should result in the most intense growth of pore space, as indeed observed in Fig. 4.5. Qajar and Arns [71] and Egermann et al. [174] reported similar findings of preferential enlargement of the pores in their experimental studies in which they analyzed the dissolution of limestone in a uniform dissolution regime.

Thickness (µm)	S1	S2	S3
pores (max)	588 ± 52	1097 ± 159	641 ± 43
pores (mean)	184 ± 8	261 ± 15	221 ± 9
pores (std)	68 ± 3	109± 12	75 ± 3
grains (max)	840 ± 48	764 ± 51	807 ± 43
grains (mean)	245 ± 5	262 ± 7	226 ± 4
grains (std)	90 ± 4	104 ± 4	87 ± 4

Table 4.1: Characteristics of the thickness distribution of the samples S1-S3

Further insight into the characteristics of natural dissolution can be obtained from the study of distribution statistics, as presented in Table 4.1. Before we discuss these results, it is important to note that during the dissolution process, the local thickness of pore space may increase through two different mechanisms: firstly, through the enlargement of individual pores and secondly, by merging of pores. If the former takes place without the latter, the average thickness increase (Δb) can be calculated by balancing the gain of the volume of pores ($\Delta V \sim \phi_2 - \phi_1$) to the surface area of pores times "shift" of the pore-grain boundary ($\Delta b/2$).

$$\Delta b \approx 2(\varphi_2 - \varphi_1)/s_1 = 22.7\mu\text{m}$$

The above calculation shows a much smaller increase in local thickness compared to the thickness difference between the numerically eroded sample S3 and the undissolved sample S1, which is approximately 34 µm. This implies that the merging plays a significant role in the increase of local thickness, consistent with the high porosity of the original sample. Conversely, the increase in local thickness in the naturally dissolved sample S2 compared to S1 is even larger, exceeding 70 µm. This further suggests that the dissolution is non-uniform and predominantly occurs in regions with the largest local thickness. Since these regions contribute dominantly to the average (scaling as b^3), any additional increase in their local thickness leads to a substantial growth of $\langle b \rangle$.

Another noteworthy observation based on the data presented in Table 4.1 is that, while the mean thickness of pore space in the dissolved sample is significantly larger than the mean thickness of an undissolved one, the mean thickness of grains (rock phase) remains approximately the same. Intuitively, one might anticipate these two effects to balance each other, with the thickness of grains decreasing by a similar amount as the thickness of pores increased. This assumption would hold if the pores in the samples are well-separated. Nevertheless, as we will discuss further, the merging of pores disrupts this balance. To elucidate this point, we introduce a two-dimensional conceptual model (Fig. 4.6) made with a specific arrangement of circular grains in which a smaller grain is surrounded by several larger grains and pore spaces, which merge as a result of the dissolution. Merging of the pores removes the 'obstacles', allowing a much larger sphere or ellipse to be inscribed than when such 'obstacles' exist (as illustrated by the small circle in the middle of Fig. 4.6(left)). This results in an additional thickness increase beyond that caused solely by the shifting of the rock/pore boundary. For the details of this model, the reader is referred to Sharma et al. [150].

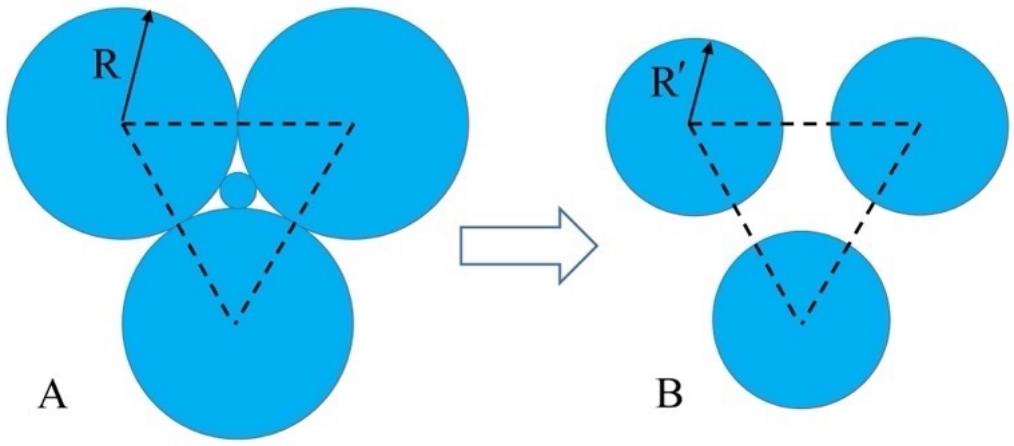

Figure 4.6: A simple conceptual model showing the asymmetry between growth of pore thickness and decrease of grain thickness: initial geometry (A), and the geometry after the dissolution (B). The blue circles represent grains while the in-between white space represents pores. The grains in (A) shrink and the small one completely vanishes due to dissolution, resulting in larger pore space in (B) [150].

In three dimensional case, it becomes evident that not all pore shapes, while merging,

experience a significant increase in their average local thickness: the largest relative increase is anticipated in oblate or pancake-like shapes, which have similar depths as their initial local thickness (Fig. 4.7). When two such pores merge, their local thickness can increase significantly. Conversely, if two prolate (cigar-like ellipsoids) shapes merge, the increase in their local thickness is only marginal.

Consequently, if we claim that the local thickness increases due to pore merging, we must also ensure that at least some of the pores are of the oblate shape. This is because merging between two prolate shapes, or even between a prolate and an oblate shape, results in a relatively smaller increase in local thickness. This phenomenon can be observed in the corresponding Flinn diagram for an undissolved sample, as depicted in Fig. 4.8, which shows the fraction of pore volume for which the largest inscribed ellipsoid has specific values of A/B and B/C (as indicated on the axes). Small A/B and relatively large B/C ratios characterize the oblate shapes while the opposite corresponds to prolate shapes. Although the majority of the pore shapes are neither oblate nor prolate, there is in fact a significant fraction of oblate-shaped pores in our sample.

	S1	S2	S3
χ	139987	82438	103955

Table 4.2: Connectivity (χ) for samples S1-S3.

We also study the changes in pore structure due to natural dissolution using connectivity χ. Change in connectivity is a direct indicator of pore-merging in the sample, since χ is a topological invariant pore enlargening without merging does not change it. Table 4.2 shows the measured connectivity in all three samples. The natural dissolution results in a substantial change in χ with a 25% decrease in connectivity between S1 and S3. This is primarily due to merging associated with uniform dissolution of the pore space. Conversely, the dissolved sample S2 shows an additional 20% decrease in connectivity, which is attributed to extra merging due to the focusing of dissolution in the largest pore spaces.

Finally, the changes in pore space are also reflected in the flow characteristics, the description of which is given in Section 4.3.4. The dissolution results in a large increase in rock permeability as the dissolved sample is characterized by a larger overall permeability compared to the undissolved one, with a ratio of ($K_2/K_1 \approx 4.15$). This exceeds the expected calculated values from Kozeny-Carman equation ($K(\phi) \sim \phi^3/(1-\phi)^2$), which would yield the ratio (K_2/K_1) around 3.24, indicating an additional focusing of flow in larger pores. The tortuosity (τ) of the samples is calculated using Eq. (4.1) which yields ($\tau = 1.463$) for the undissolved sample and ($\tau = 1.323$) for the dissolved sample. The decrease of tortuosity during dissolution is an indication of straightening of flow paths, which is consistent with the experimental findings of Luquot et al. [68] and Pereira Nunes et al. [107]. Notably, Luquot et al. [68] observed that a significant (>10%) decrease in tortuosity is usually associated with the uniform dissolution regime, whereas the changes in tortuosity are relatively smaller in wormholing regime.

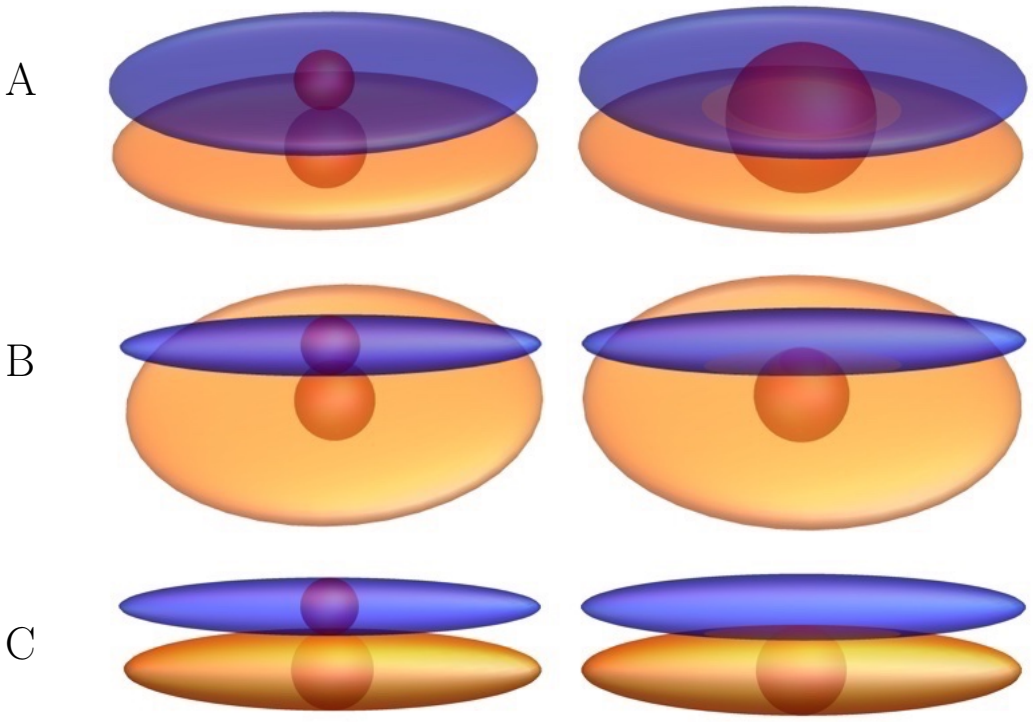

Figure 4.7: Merging of two oblate spheroidal pores (A), an oblate and prolate pore (B), and two prolate spheroidal pores (C). The left column shows the pores just before merging, in the right column the pores are enlarged by dissolution and they intersect. Red balls correspond to the maximal inscribed spheres inside the pores. In (C) the increase of thickness is only due to the dissolution of the larger pore, with no contribution from merging. In (B) there is a relatively small, but non-zero, increase in b due to merging. Finally, in (C) there is a significant increase of thickness, most of it due to merging, with the final b of the order of the sum of the thicknesses of the original pores, $b_{12} \approx b_1 + b_2$ [150].

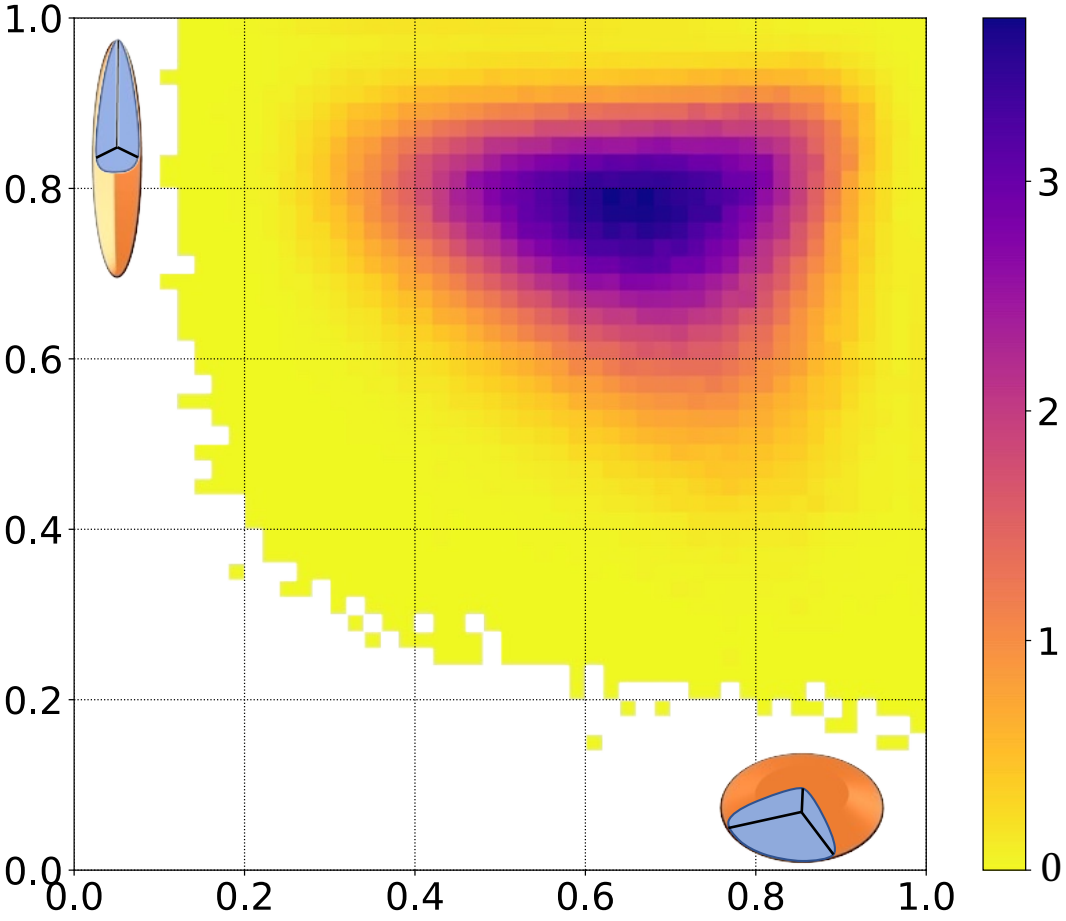

Figure 4.8: Flinn diagram for the undissolved sample. The colors indicate value of the contribution to the total pore volume coming from specific shape - i.e. volumes for which the largest inscribed ellipsoid has values of A/B and B/C from specific ranges. All contributions sum to 1. Oblate shapes correspond to small A/B and relatively large B/C [150].

Confirmation of the presence of faster-flowing region in the sample is further supported by the analysis of the velocity distribution (Fig. 4.9) which shows a noticeable shift towards higher values with an emergence of a fat tail for large velocities.

4.5 Conclusions

In this study, we have investigated the changes of pore space geometry incurred in natural samples as a result of dissolution. The small porosity gradients observed in a dissolved sample led us to the conclusion that dissolution proceeded in a uniform regime, with a reactant penetration length much larger than the system size. Naively, one would expect that uniform dissolution should result in the removal of a constant layer of mineral from all the rock surfaces and the associated increase in the local thickness by $\Delta b = 2\Delta\varphi/s$, however, the actual increase in thickness is

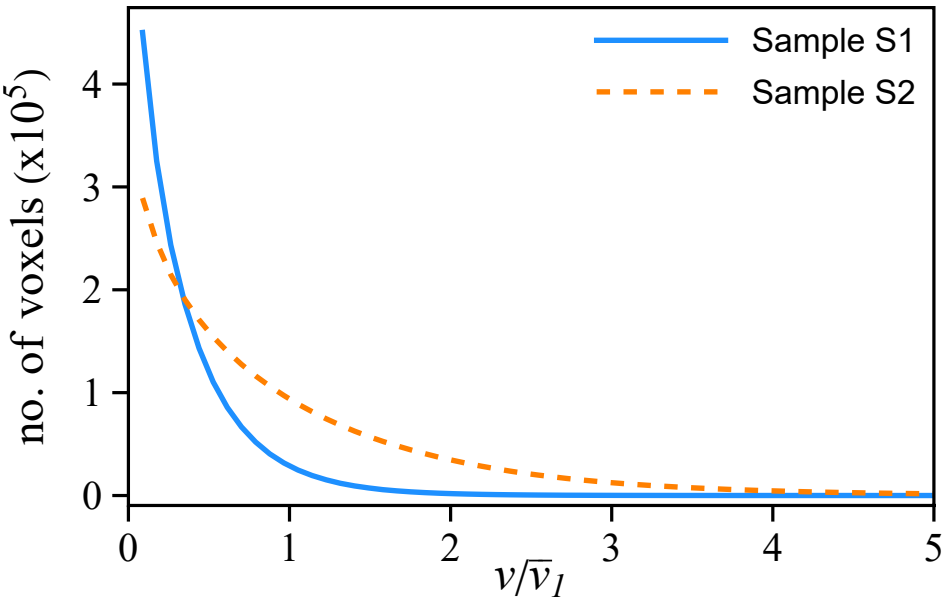

Figure 4.9: The distribution of velocities in the dissolved and undissolved sample. The velocities are normalized by the mean velocity in the undissolved sample. The bin size used to calculate the counts is $\Delta = 0.004$ [150].

much larger. One important mechanism is merging of the pores, which is prevalent in a sample of such high porosity. Merging can significantly increase the thickness of the pore space; in the extreme case (if the merging pores are oblate in shape), the merged pore will have a thickness equal to the sum of the thicknesses of the constituents. However, it turns out that merging itself cannot explain all of the changes in the pore-space geometry. We observe strong focusing of dissolution in the largest pore spaces, which can be described in terms of the uniform channeling regime, with the emergence of preferential pathways linking the regions of the highest local permeability. This is also reflected in the decrease of tortuosity of the flow paths, and the increase of the fraction of the faster flow in the sample.

From a more general perspective, a set of tools presented in this chapter should allow one to delineate the effects of uniform dissolution of individual pores, merging and emergence of preferential flow paths during dissolution, both in natural and laboratory settings.

Chapter 5

Geometric characterization of wormhole shape in core-dissolution and influence of rock structures

There is geometry in the humming of the strings, there is music in the spacing of the spheres.

Pythagoras

5.1 Introduction

This chapter is also the original work of the Author and contains both published [41] and unpublished findings. In the published article [41], Author has contributed significantly by developing image-processing methods to analyze the tomographic images of conducted experiments. The discussion will cover those results in detail, along with new findings that further expand upon the study.

In the previous chapter, we discussed how dissolution changes the pore space and therefore influences the rock heterogeneity. However, the resulting dissolution patterns and their growth dynamics can also be influenced by the structural features of the rock, such as microfacies. This influence is not easy to observe as the wormhole usually forms inside a rock, shielded from the naked eye by the rock matrix. The first attempts to study the growth of wormholes were thus limited to either a quasi-2D systems [46] or observing the emergence of channels at the inlet and outlet of 3D systems. A significant advancement was casting Wood's metal into the formed channel [37, 45]. After casting, the remaining sample is dissolved, leaving an imprint of the wormhole network. This allowed the visualization of the network of the wormholes in acidized cores and established that the geometry of the wormholes strongly depends on the injection rate of the fluid.

The growth dynamics of wormholes were still impossible to capture using casting methods and the alternative was to use X-rays. However, due to technological limitations, the studies involving X-rays were initially restricted to projection radiography

of wormholes [175]. The growth of a wormhole can only be indirectly inferred by measuring the pressure and permeability change in a dissolving sample throughout the experiments. Building on the use of X-ray techniques, a way forward was to use time-lapse tomography, which required placing the reactive flow core holder along with a dissolving sample inside a tomograph. A pioneering study of this kind was conducted by Bazin et al. [47]. However, the acquisition times were still long compared to the wormhole growth rate. While imaging had improved, it was still limited to a few low-resolution 2D scans. Recently, this technique has been significantly advanced, allowing four to ten 3D scans per experiment with time resolution up to 30 minutes [48–51]. In the present study, we optimize scan spatial resolution by balancing it with acquisition times. Using a lower spatial resolution allows for more scans per dissolution experiment within a shorter acquisition time. By taking advantage of shorter acquisition times, we will capture details of the growing wormhole shape, including the position of its tip. We will compare the geometric details of the growing tip at three different resolutions: 42, 84.5 and 169 µm, and select the optimal spatial resolution, balancing accuracy and acquisition speed. We will also investigate the influence of tip movement on sample permeability during wormhole growth.

We will use image-processing methods to extract the wormhole shape from tomography scans. These shapes will then be analyzed to study the geometric evolution of wormholes quantitatively. The analysis will be performed using geometrical measures, such as tortuosity and length wastefulness. These measures will also be used to investigate the influence of micro-layers of a rock over the shape of the formed wormhole. Two different types of limestone will be considered in dissolution experiments: Pińczów and Wierzbica limestone. Both of them are from the Swiętokrzyskie mountain region; however, they both differ significantly. Pińczów limestone is ten times younger than Wierzbica limestone and formed in different environmental conditions. Both limestones display characteristic microfacies layers, indicative of their unique depositional environments. A detailed discussion of these rocks is presented in Sec. 5.2.1. Later in Sec. 5.2.2-5.2.3, we will discuss the sample preparation method, experimental setup, and a list of performed experiments, along with sample properties.

This chapter presents both the results of Cooper et al. [41] as well as the unpublished data analyzed by the Author. The publication, Cooper et al. [41], was a result of a collaborative effort, with experiments and tomography performed by Dr. Max Cooper and the image analysis done by the Author. In the following sections, we will concentrate on the work of the Author. In Sec. 5.2.4, we will introduce an image processing method to extract the shape of the wormhole from the tomographic scans. To achieve this, we propose a volume-based segmentation algorithm that includes a connected component approach. The extracted wormholes are then converted into skeletons, which are single voxel-wide structures that preserve the wormhole features such as branching and overall shape. For the characterization of wormhole shape, we will propose geometric measures, which will be discussed in Sec. 5.2.5. Finally, the results will be discussed in Sec. 5.3.

5.2 Materials and methods

To study the geometrical properties of dissolution channels, we employ 3D and 4D (time-series 3D) X-ray micro-tomography data of dissolved limestone samples, image-processing methods, and calculations of proposed geometrical measures. In this section, we will discuss these methods in detail.

5.2.1 Material properties

We have used two types of limestone rock collected from the Pińczów and Wierzbica quarries. Pińczów quarry is in the Swiętokrzyskie (Holy Cross) mountain region, while the Wierzbica quarry is situated in the northeast margin of these mountains.

The time of formation and geological properties of these limestones differ significantly, with Pińczów being formed during the Middle Miocene (Badenian) formation, approximately 15.97 to 11.608 million years old. The well-described facies of this limestone [176]—characteristics of the rock such as grain size, fossil content, and sedimentary structures, that distinguish it from the adjacent rock—indicate a warm and shallow marine environment at the time of its formation. The deposition of material took place with fluctuating water levels [176], resulting in the formation of less compact and porous limestone with higher primary porosity ($25 - 35\%$) and permeability. The fluctuating water levels also resulted in less diverse marine life and, therefore, less variety of fossils, mostly dominated by foraminifer and echinoid spines.

Figure 5.1: Sample collection sites in Poland

Wierzbica limestone, on the other hand, was formed in the upper Jurassic period (to be more precise, Early Kimmeridgian) around 157 to 152 million years ago [177]. This is an ooid limestone with varying amounts of molluscan bioclasts that exhibits intercalations of oolitic layers (classified as packstone and grainstone) and micritic limestone (classified as wackestone) as well as intercalations containing glauconite [178].

Table 5.1: Material properties of Pińczów and Wierzbica limestones

Limestone	Porosity (%)	Permeability (Darcy)
Pińczów	$25 - 35$	$2 - 2.5 \times 10^{-3}$
Wierzbica	$22 - 23$	1.8×10^{-2}

5.2.2 Sample preparation

The samples used in this study are cylindrical cores. Most have dimensions of around 3.84 cm in diameter and a length of approximately 11.2 cm. However, in four experiments, the samples were smaller: two samples were 6.0 cm in length, and the other two samples were 2.5 and 3.2 cm in length with a diameter of 1.5 cm. Table. 5.2 shows in detail the physical dimensions of different samples. These samples were prepared on a drill press using a coring bit. The drilling was done perpendicular to the bedding direction of Pińczów rock, while for Wierzbica, no specific direction was selected. These samples are then put in a vacuum chamber at 1 bar negative pressure for 12 hours to let the air out of the samples. Later, the samples are left in deionized water for another 12 hours for full saturation. We will follow a labeling method here in which the samples of Pińczów rock are labeled with the prefix "P" and the samples of Wierzbica limestone are labeled with the "WB" prefix.

5.2.3 Experimental Setup and Computed Tomography

The experimental setup used in this study is the same as described in Cooper et al. [41]. The samples were put inside a Viton sleeve with both sides of the tube covered by ceramic disks (3.83 cm diameter) to ensure uniform flow distribution at inlet and outlet. For shorter samples, cylindrical spacers were used to maintain overall length. The whole setup was then mounted in a high-pressure Hassler cell with a confining pressure applied radially to avoid leakage of reactant to the side of the sample. A water/HCl solution was injected into the cell using a computer-controlled high-pressure pump, and back pressure was applied at the outlet of the system to prevent the formation of CO_2 during dissolution experiments. The appropriate back pressure was adjusted to acid concentration using Henry's law [179], and the confinement pressure was set to the sum of the back pressure and the initial pressure drop across the sample, plus a 10% overhead. All the fluids used in the setup were degassed under vacuum prior to an experiment, and all the fluid lines were filled with deionized water to ensure single-phase flow through the entire system.

To obtain in-situ information on dissolving samples, we have used X-ray computed

Table 5.2: Experimental parameters, and properties of different specimens extracted from different limestone rocks.

Sample name	Diameter (cm)	Length (cm)	Injection rate (ml/min)	Acid molarity
PIN01	1.50	3.50	0.07	0.25M HCl
PIN02	1.50	2.50	0.18	0.1M HCl
PIN04	3.84	11.04	0.175	0.5M HCl
PIN05	3.84	11.07	0.175	0.5M HCl
PIN43	3.90	6.00	0.5	0.1M HCl
PZ01	3.82	11.42	0.5	1.0M HCl
PZ02	3.83	11.42	1	0.25M HCl
PZ03	3.83	11.25	1	0.25M HCl
PZ05	3.84	11.40	0.25	1.0M HCl
PZ07	3.83	11.41	4	0.25M HCl
PZ08	3.84	11.36	0.5	0.25M HCl
PZ09	3.84	11.50	4	0.1M HCl
PZ14	3.84	11.50	1	0.25M HCl
PZ25	3.84	11.37	0.25	1.0M HCl
PZ26	3.84	11.66	1	0.25M HCl
PZ27	3.84	11.46	1	0.125M HCl
PZ29	3.86	10.10	0.175	0.5M HCl
PZ103	3.8	11.40	1	0.25M HCl
WB03	3.83	12.15	1	1.0M HCl
WB06	3.85	12.28	1	1.0M HCl
WB10	3.84	12.11	1	1.0M HCl

tomography (XCMT) technique. The scanning was done at two different facilities: the Institute of Oil and Gas (INiG), Krakow, Poland, and Institut Laue-Langevin (ILL), Grenoble, France. Both of these facilities have tomographs of different specifications. INiG model (RXCT GeoTek Ltd. machine) is designed for scanning longer cores at horizontal orientation. The X-ray source (Thermo Kevex Microfocus, 45-130 kV, 4-65W) and detector (Varian PAXScan 2520DX, 1920×1536, 16bit pixels) rotate around the core and can scan in the range of $30 - 350$ µm voxel resolutions. The ILL tomograph, on the other hand, combines neutron and X-ray tomography. The X-ray system in this facility offers high-resolution imaging, combining a Hamamatsu L12161-07 microfocus source and a Varex PaxScan 2530HE detector. The source achieves a minimum focal spot size of 5 µm, while the detector, with its 1792×2176 pixel array, ensures precise image capture.

All the static scanning (pre and post-dissolution) for different samples were performed using INiG Kraków tomograph at full resolution (30 µm), while the scanning of actively dissolving cores (dynamic scanning), was performed at both facilities (ILL and INiG) for different experiments with resolution ranging from $42 - 169$ µm. To scan a full sample (static scanning), a core was held in a plexiglass tube that is attached to motor-controlled arms, capable of repositioning itself, allowing to scan longer cores that go out of field of view due to their length. To cover the whole

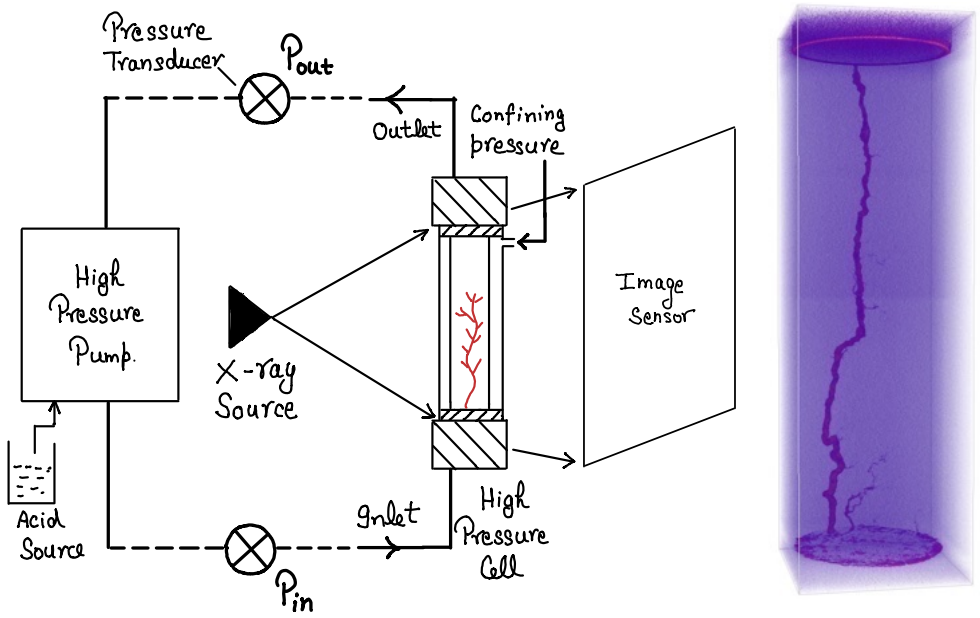

Figure 5.2: Core dissolution experimental setup with a core holder placed inside micro-CT machine. A sample visualization of a wormhole formed inside the sample, shown in right panel. The visualization is prepared from the grayscale scans in an open-source package TomViz.

length of a sample, it was scanned in multiple sections. For each section, the X-ray source rotated 360° and recorded the radiographic projections at 16-bit precision to have enough data for rebuilding the 3D pore-space of the scanned sample. The pore space was then reconstructed from the radiographs of different sections of a sample, resulting in a 3D stack of slices of 16-bit grayscale images. Each slice of the stack is 1800×1800 pixels, containing sections of core-holder, sleeve, and core. The number of slices differs for each sample based on the length of the sample. Fig. 5.2 shows the schematic of the whole setup and an example of the obtained 3D tomography scan visualized in TomViz.

While scanning dissolving cores, a similar process was followed; however, instead of placing just a sample, the entire core-holder setup—including connecting lines and fluid-carrying tubes—was placed inside the tomograph. The scanning was performed at lower resolutions to reduce the time required for one complete scan of a sample. The resolution of each time-series scans are given in Table. 5.4.

5.2.4 Image processing methods

Each grayscale image contains data of 16 bits which means the pixels contain the values (pixel intensity) ranging from 0 to 65536. The lower intensities correspond to air or pores, while the higher intensity indicates a higher-density material such as metal and solid grains. Since in our scans, we captured a core holder (metal) and Viton sleeve in addition to the core sample, we need to process the image to remove this extra information. To do this, we have adopted a sequence of procedures including cropping, subtracting, binning, etc., depending on the type of experiments:

static scans (3D) and time-series 4D (3D with time). For static scans, all the slices are first cropped to 1400×1400 pixels in size, containing mainly the pixels belonging to the core. The cropped slices are converted to a 3D image stack, which is around 16 GB in size, and is hard to process due to computational limitations. Therefore, each 3D image stack is binned by a factor of 4, resulting in an image stack with 350×350 pixels size image. The reason for not scanning the sample directly at lower resolution—but downscaling it—is that due to the availability of higher resolution scans, the loss of information in downscaling a sample can be inspected. The finalized downscaling factor—without much information loss— can be applied to the bulk of the data.

The number of slices in a binned stack depends on the sample size. At this stage, our scans are ready for the segmentation process, which is a crucial step to convert a greyscale stack to binary images containing black and white voxels, referring to pores and grains, respectively. We will discuss the segmentation process in the following section.

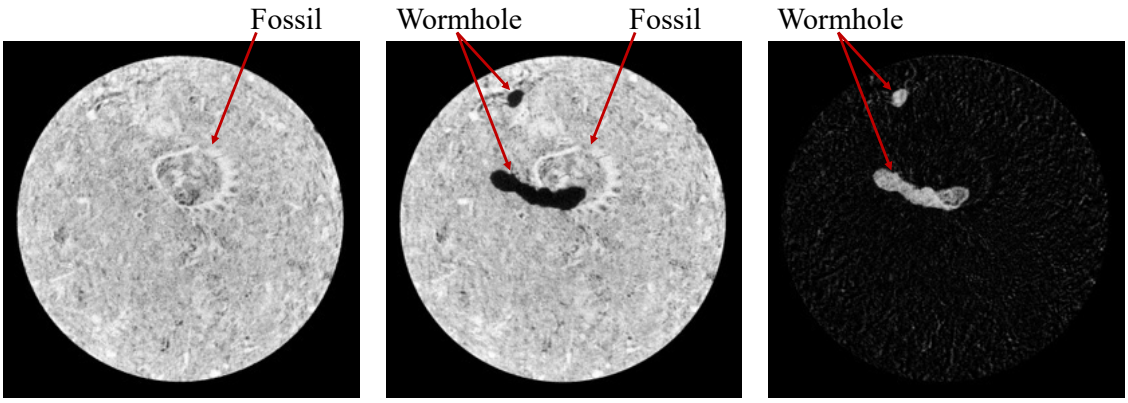

Figure 5.3: Slices of 16-bit grayscale scans of the PZ103 sample at a resolution of 42 µm (a) undissolved sample (b) corresponding slice of dissolved sample (c) the subtracted image. The pixel intensities of all three slices are enhanced for better contrast by rescaling the minimum and maximum to a similar range.

The time-series 4D scans are also processed similarly with a few extra steps. A series of scans contains the information on the time-evolution of evolving porosity in dissolving parts of the sample as well as unaffected rock matrix. To remove this unaffected part, all the scans are subtracted from the initial scan. However, due to moving fluid in the system, and errors in scanning and reconstruction, voxel intensities of some voxel corresponding to rock matrix are not the same in different scans, which results in the appearance of small noise after subtraction. The subtracted images thus contain the evolving wormhole along with minor noise, which needs to be removed for the clean extraction of wormhole. Fig. 5.3a and b show a slice of a sample before and after dissolution, respectively. The slices, shown here, are post-processed by cropping them to 1400×1400 voxels and removing the voxels corresponding to the core-holder. Fig. 5.3c shows the same slice after subtracting

the dissolved one (Fig. 5.3b) from the initial (Fig. 5.3a). It contains noise and a wormhole over a black background.

Volume based segmentation

Segmentation is a commonly used method in image processing that reduces an image to binary format (black and white) and allows one to focus on the specific part (i.e. white, "1"s) of that image by discarding extra information (black,"0"s). Several segmentation methods exist—such as watershed methods [180], region-based methods [181], and of particular interest to us, thresholding methods—most of which are designed for general purposes, making them widely applicable. However, in our case, existing pores and unresolved micro-pores make it harder for an algorithm to differentiate between newly formed pores (dissolution channels) and existing ones. Consequently, we have developed a thresholding method—similar to the Otsu segmentation method [182]—based on calculating the volume of the wormhole. Fig. 5.4 shows a flowchart of the developed volume-based segmentation procedure.

In this algorithm, we first select a region of interest (ROI), for example, $300 \times 300 \times 300$ voxels here, from the grayscale scans, containing a part of wormhole and rock-matrix. The lowest voxel intensity values are pores (either dissolved or pre-existing), and higher values represent grains. Then, we invert the image so that the pores are brighter and the grains are darker. Starting from the minimum voxel value, in the ROI, as a threshold value (Th), we segment the image so that the values higher than Th become white ("1"s) and lower values become black ("0"s). The segmented image contains only the voxels belonging to the dissolution channel and pre-existing pores. To isolate the dissolution channel, we select a voxel of the wormhole and use the Scikit-flood-fill algorithm [183] to extract all the voxels of the wormhole connected to the given voxel. This algorithm finds individual objects for both 2D/3D images by finding orthogonally connected pixels/voxels. Fig. 5.5 shows an example of this algorithm in which a structure corresponding to a given pixel is isolated from a 4×4 binary matrix. The number of voxels in the wormhole is counted and saved as the volume of the wormhole in ROI. The process is repeated with a fixed step increase of Th values to obtain a dependence of volume on the Th values (top right panel of Fig. 5.4).

In the region where the connected component algorithm isolates the wormhole from the surrounding noise or pore space, we observe a smaller slope of volume-threshold curve—indicated by dashed lines in the plots of Fig. 5.4—in comparison to the slope when the wormhole is connected with noise or existing porosity. We analyze the changes in the slope of this curve by calculating the first and second derivatives. When the wormhole is completely detached from noise or pre-existing pores (in the region marked by dashed lines in Fig. 5.4), both the first and second derivatives play a crucial role in selecting a suitable Th value. The first derivative helps identify the transition region where the structure stabilizes, while the second derivative reveals fluctuations caused by the connecting-disconnecting surrounding pores. In the transition region (just before the plateau), the first derivative appears to smoothly approach zero, indicating a reduction in rapid structural changes. However, analyzing the second derivative reveals residual oscillations in the first derivative, which

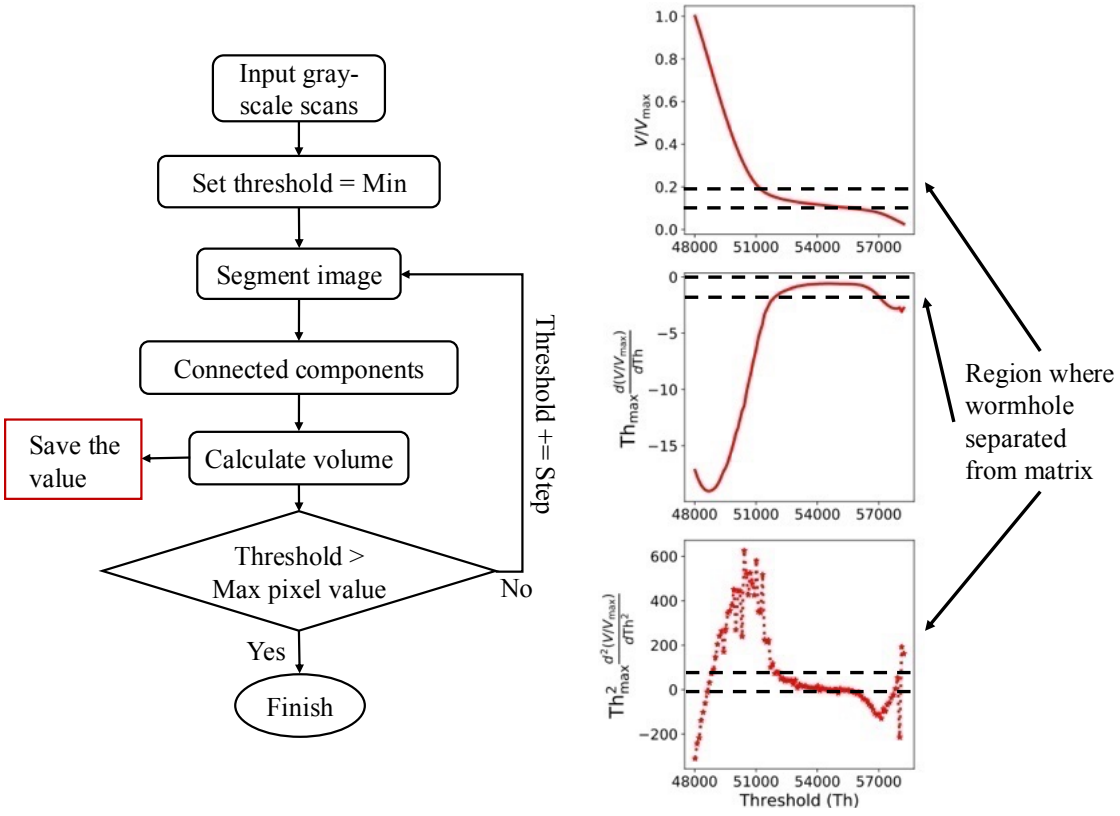

Figure 5.4: Description of volume-based segmentation procedure with flow-chart of the algorithm (left panel). The variation of the volume (rescaled by ROI volume), of the connected structure (wormhole) with threshold values is shown in the right panel, which comprises three plots: rescaled volume vs threshold (top), rate of change of rescaled volume with respect to threshold values (middle) and the second derivative of rescaled volume with respect to the threshold (bottom). Note that both first and second derivatives are also rescaled by the maximum Th value in ROI. These curves show the sensitivity of the volume of the structure to the threshold values. At a specific threshold, the connected component algorithm no longer connects the wormhole to the rest of the pore-matrix leading to a plateau in the curves, as highlighted by the dashed lines.

stem from interactions with nearby pores. These oscillations decay as the plateau is reached, marking the stabilization of the wormhole structure. To ensure that the selected Th value reliably extracts only the largest connected component—without introducing noise or pre-existing pores—we focus on the region where both the first and second derivatives are small. The smallness criteria for these derivatives is defined as when the standard deviation of the values around the plateau value is $< \pm 0.1$. This ensures that the chosen threshold corresponds to a stable structural regime, where minor adjustments do not significantly alter the extracted morphology. Thus, we verify this criterion for ten successive Th values to confirm robustness.

Finally, the threshold value selected using this method is applied to the downscaled greyscale scans of the whole sample. The 3D binary matrix can contain multiple wormholes, of which we ignore the wormholes of length smaller than one-third of the

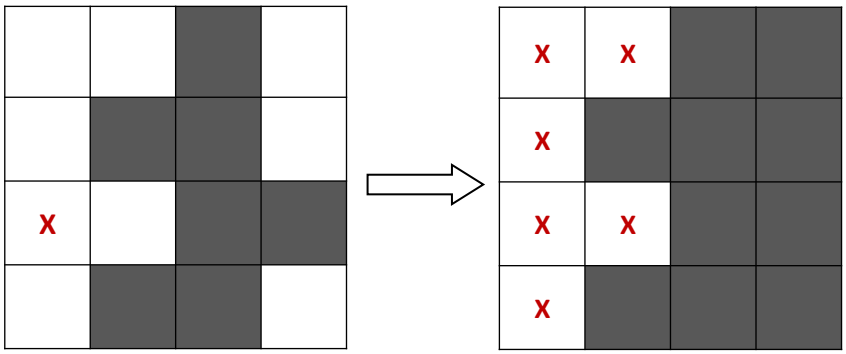

Figure 5.5: A pictorial description of the connected component algorithm in a sample image of 4×4 pixels. In the left panel, three structures are shown in white color, and X represents the selected pixel of the structure of our interest. In the right panel, the connected pixels are found (marked with X), and the rest of the structures are discarded.

diameter of the sample. In most of the experiments, the secondary wormholes are very small therefore we only isolate the largest one in those experiments. However, if the length of secondary wormholes exceeds the criteria ($> d_0/3$), they are also considered. The selected wormholes are extracted by finding connected components and later used in studying the geometrical properties of the dissolution channels.

Skeletonization

To study the morphological properties of wormholes, we use the SciPy library [82]. A 3D skeletonization method is adopted, in which we convert a 3D binary matrix to a structure (skeleton) of one voxel width. For this, we use the scikit-skeletonize3D algorithm. First, the scikit-binary-fillholes function is used to fill the possible holes in the wormhole to avoid artificial loops in the skeleton. These holes may form within the wormhole either due to the undissolvable material that obstructs its evolution, causing the wormhole to develop around the obstacle and form a hole, or from the noise. Next, a median filter of two voxel size is applied for smoothening the surface of the wormhole, as a slight noise can create artificial branching. Finally, the scikit-skeletonize3D function is used to convert the wormhole into a skeleton. The obtained skeleton is still in the form of a binary image stack, which needs to be processed further to convert it into a network graph for studying its properties.

Following skeletonization, we load the skeletonized images in a python package SKAN [184] and convert them into 3D network graphs, which are further loaded in another python package NetworkX [185] for network analysis. A 3D graph is made of connected nodes which are voxels of skeletons in our case, and it contains the information of the coordinates of nodes and their connections in the form of a sparse matrix. These graphs are saved for further inspection using the VTK library [186].

Visualization

The visualization of all the 3D data, including image stacks of wormholes, skeletons, and network graphs, is performed mainly in open-source packages: TomViz, Paraview, and Mayavi. The binned grayscale scans and segmented images are visualized in TomViz [187], which is also used to prepare figures in this study. Paraview [188] is mainly used in the visualization and inspection of the NetworkX graphs. Mayavi [189] is used in the preparation of videos of developing wormholes from time-series experiments.

5.2.5 Geometric measures

For quantitative analysis of wormhole geometry, we use tortuosity (τ) as a standard geometrical measure, along with a newly proposed metric, length wastefulness ($\mathrm{W_L}$). For time-series 4D experiments, we also measure the movement of wormhole tip position $\mathbf{r}_{\mathrm{tip}}(t)$ with time, in addition to the time evolution of other geometric measures. These measures are calculated either from wormhole binary images or from the network graphs. A detailed description of these measures is given below.

Tip position $\mathbf{r_{tip}}(t)$

The movement of the wormhole tip is calculated from binary 3D time-series scans by extracting the coordinates of the tip from each scan. For a scan, tip position $\mathbf{r}_{\mathrm{tip}}$ can be defined as:

$$\mathbf{r}_{\mathrm{tip}}(t) = x_{\mathrm{tip}}\hat{\mathbf{i}} + y_{\mathrm{tip}}\hat{\mathbf{j}} + z_{\mathrm{tip}}\hat{\mathbf{k}}$$

where $\hat{\mathbf{i}}, \hat{\mathbf{j}}$ and $\hat{\mathbf{k}}$ are the unit vectors, and x_{tip}, y_{tip} and z_{tip} are the components of tip position in X, Y and Z directions, respectively.

Tortuosity (τ)

The tortuosity (τ) of a wormhole is defined as the ratio of its total length to the distance traveled by the tip along Z-direction (z_{tip}). For samples that have reached a breakthrough, z_{tip} is just the length of the sample. The measurement of tortuosity is done on a NetworkX graph. First, the inlet node and the node at the tip of the wormhole skeleton are selected. Then, the shortest path along the wormhole between both nodes is extracted from the network using the NetworkX package with the Djikstra algorithm. The length of such a shortest path is considered the length of the wormhole.

Length Wastefulness ($\mathbf{W_L}$)

The length wastefulness ($\mathrm{W_L}$) is defined as the ratio of the total length of a wormhole network, including branches, to z_{tip}.

$$\mathrm{W_L} = \frac{\text{Length of the wormhole including branches}}{z_{\mathrm{tip}}}$$

This property can be treated as the generalization of a tortuosity for a branched structure. It measures the amount of total length wasted—or created—on moving the structure by a unit length. For a non-branched structure, size of network reduces to the actual length of the structure, and therefore, length wastefulness of the structure reduces then to τ. We measure this quantity using NetworkX graphs. The calculation is done by summing up all the lengths in a 3D network and dividing by the z-coordinate of wormhole tip.

5.3 Effect of image resolution on wormhole geometry

Before proceeding to analyze the wormhole geometry, we have investigated the effect of tomography scan resolutions on the fine details of wormhole features. At low resolution, the fine details of the structure will be smeared out while at high resolution the acquisition time will be longer comparing to the time-scales of wormhole growth. Thus, capturing the growth dynamics of a wormhole requires balancing scan duration with the resolution needed to real its fine structure. To determine the optimal acquisition settings, three static scans of a partially dissolved core (PZ103 sample) were performed within the cell setup described in Sec. 5.2.3.

The voxel resolutions of the scans were 42, 84.5, and 169 micrometers, and corresponding voxel grayscale distributions are shown in Fig. 5.6. It is evident that higher resolution (42 µm) has a larger spread, and therefore larger range of pixel values, indicating a larger amount of captured information, which decreases with lower resolutions (82 and 169 µm). In addition, the mean value of the 169 µm distribution is around 2% higher, compared to 42 and 84.5 μm scans, indicating that the segmentation method will give different optimum threshold values for 169 µm resolution. This is indeed the case as seen in Table. 5.3, which shows the obtained threshold values as well as the wormhole volume at different resolutions. For both 42 and 84.5 µm resolution scans, the threshold value is the same (8450 voxels), while for 169 µm case, the threshold value is higher (9495 voxels). Moreover, the volume of the wormhole is very similar for 42 and 84.5 µm resolution, compared to 169 µm scans, which results in a higher volume of the wormhole.

Table 5.3: PZ103: Thresholds and volumes at different resolutions.

Voxel size (µm)	Threshold	Volume (voxels)	Volume (mm^3)
42	8450	9012746	668
84.5	8450	1000227	603
169	9495	238432	1150

We have also visualized the effect of the resolution of the scans and corresponding threshold values on the geometry of wormhole tip (see Fig. 5.7). For this purpose, we have selected a fixed section of wormhole near the tip region, and performed the segmentation procedure with connected components. The extracted tip region from all three resolution scans is shown in the right panel of Fig. 5.7. We again

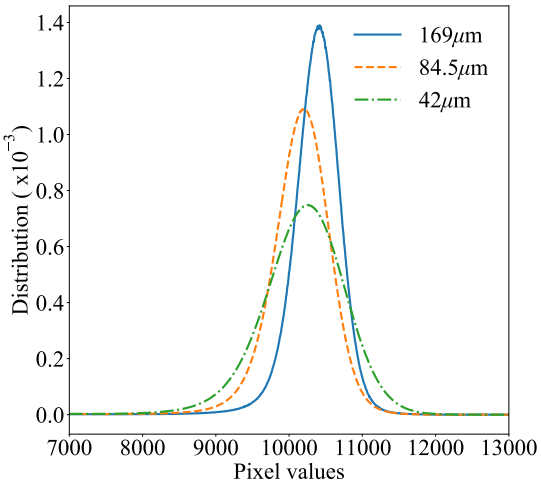

Figure 5.6: PZ103 grayscale distributions for 42, 84.5, and 169 micrometer voxel resolutions.

observe a similar effect of resolution on wormhole tip as on the volume of wormhole, which was larger with lowest resolution (169 µm). At this resolution, the tip appears bulkier, displaying distinct larger features (branches) similar to those observed in higher-resolution tip regions (42 and 84.5 µm), while smaller features remain unresolved. These unresolved features—for instance, small branches and spacing between them—at lowest resolution merge together and form a bulkier structure with a rough appearance.

It is important to note that even at the lowest resolution of 169 µm the most important features of the wormhole, such as the position of the branches, are large enough to be preserved without any significant loss in details. This justifies the use of lower resolution (169 µm) scans for the purpose of capturing details of growing wormholes in time-series experiments where the shortest scanning time is required. For static scans, usually performed before and after the experiment, higher resolution can be used.

5.4 Results and Discussions

5.4.1 Tip evolution of a dominant wormhole

We have first investigated the tip movement of a wormhole in PZ103 sample. The experimental setup is described in Sec. 5.2.3. For shorter acquisition time, as discussed previously, we have scanned PZ103 sample at 169 µm resolution, which resulted in five-minute scanning time. The wormhole shown in Fig. 5.8 was formed in a core taken perpendicular to the bedding of the rock. The sample was dissolved using 0.25M HCl at the flow rate at 1 ml/min flow rate. At this flow rate, a single wormhole develops in the sample, focusing most of the flow. As discussed in Ch. 2, this is so-called dominant wormholing regime.

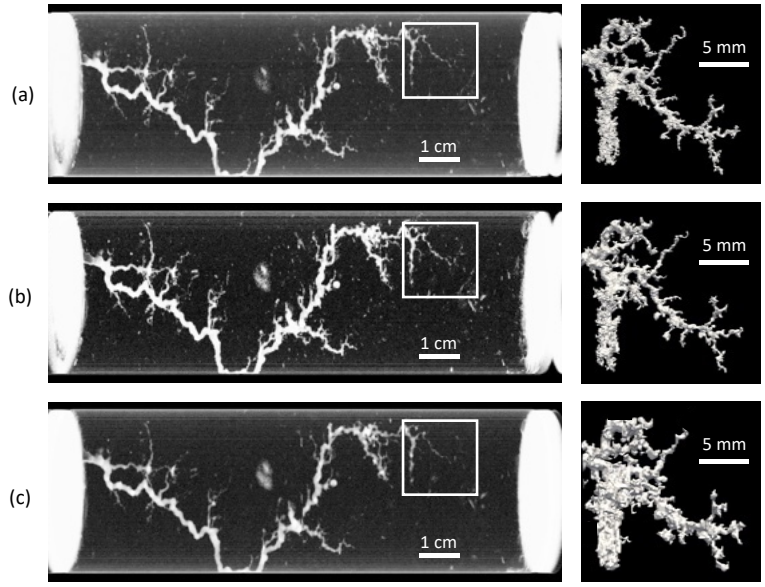

Figure 5.7: PZ103: Projections of the entire wormhole in greyscale shades from tomography (left panels) and wormhole tip region extracted using connected components (flood fill) segmentation (right panels), for 42 µm (a), 84.5 µm (b), and 169 µm (c). The overall morphology of the wormhole is maintained at each resolution, though fine details are lost for larger voxel sizes (e.g., bulkier/merged branches). While finer details are smeared out, the main feature of interest, the wormhole tip position, remains the same for the three resolutions.

As shown in Cooper et al. [41], the wormhole advances in a highly irregular manner, with numerous jumps, branching, and sudden changes of direction. What is more intriguing, however, is the apparent lack of correlation between the wormhole tip position and the changes in the sample permeability. The latter can be measured by a pressure curve (see Fig. 5.9), which shows the pressure required for a pump to push fluid through the sample at a constant injection rate, at which the experiment is performed. The pressure curve shows long plateaus interspersed with step-like pressure decreases. The corresponding tip movement of wormhole indicates that the tip advances throughout the experiment but with slower speed during these plateaus.

Interpretation of this behavior is not straightforward; the simplest but frequently used model of wormhole evolution—discussed in Ch. 2—argues that due to high permeability of a wormhole, the pressure drop along its length is negligible. Following this, and assuming that the rock in front of the wormhole tip is homogeneous, hydraulic resistance of the rock core should drop linearly with the length of the wormhole, $R \sim L - z$ where z is the length of the wormhole, and L is the total length of the system. An immediate consequence of this model is that pressure should decrease linearly with the advancement of a wormhole, $\Delta p/\Delta p_0 = 1 - z/L$, with Δp_0 standing for an initial pressure drop through the sample. However, Fig. 5.9 shows that this is not the case for our system; during pressure plateaus the wormhole

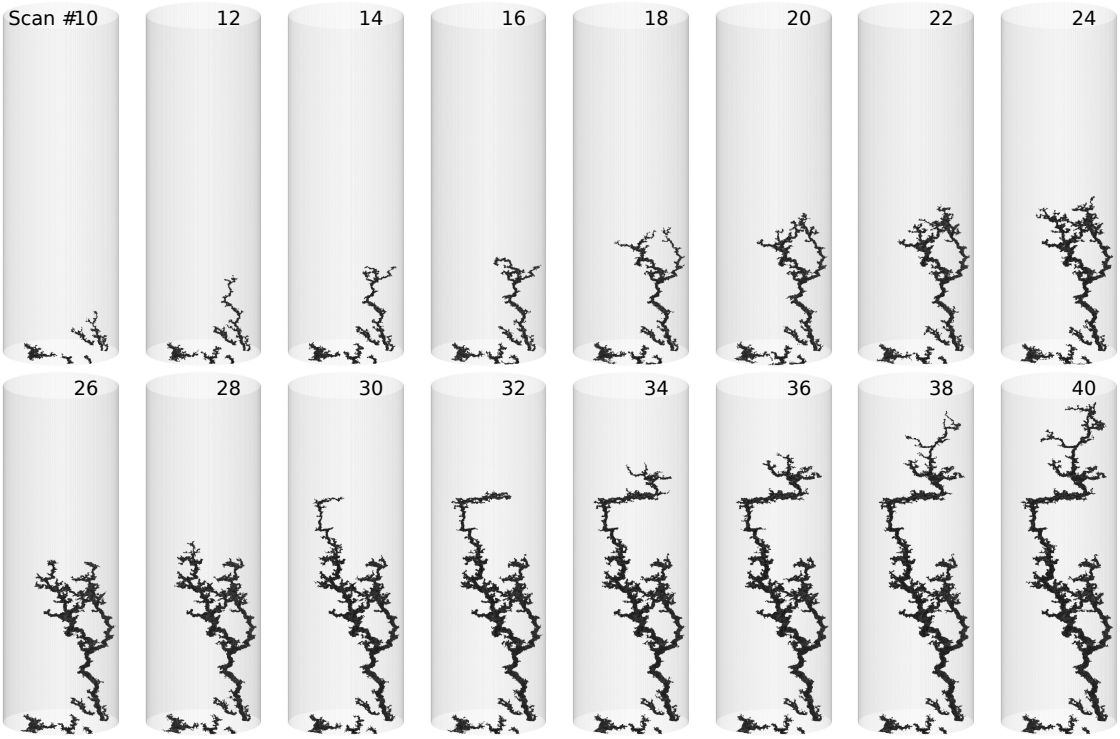

Figure 5.8: Projections of 3D renders of a wormhole at different time instances showing the development of a wormhole in PZ103 sample. Rendered data is generated by subtracting a tomographic scan from the initial tomographic scan, and projections are generated in TomViz. Diameter of plotted cylinders is 38.3mm.

tip progresses noticeably with a nearly constant velocity. Such a behavior has been reported in only a few previous wormhole studies [39, 92]. Izgec et al. [92] attributed it to vugs—large-scale local heterogeneity in pore matrix—where pressure drops are associated with the interaction of vugs with a wormhole. As the wormhole connects to a vug, it causes a more significant change in the permeability of the sample.

Pińczów Limestone, however, is not vuggy [190], and as such, we seek another explanation for this effect. We argue that such a behavior is attributed to the presence of regions of very small porosity within the sample. These regions restrict the flow and effectively act as barriers to permeability [41]. Analogous to the flow of electric current, the rock would resemble then a circuit of resistors, which are connected in series, with regions of small resistance interspersed with regions of very high resistance. If such a system was measured with an ohmmeter, the overall system resistance would be dominated by high-resistance regions. It is only when the wormhole tip reaches these high-resistance regions and begins to etch its way through them that the permeability of the core changes significantly.

Toy model

The mechanism of permeability variations can be demonstrated using a simple model [41] of porous medium of porosity φ_0, which contains bands of much smaller porosity

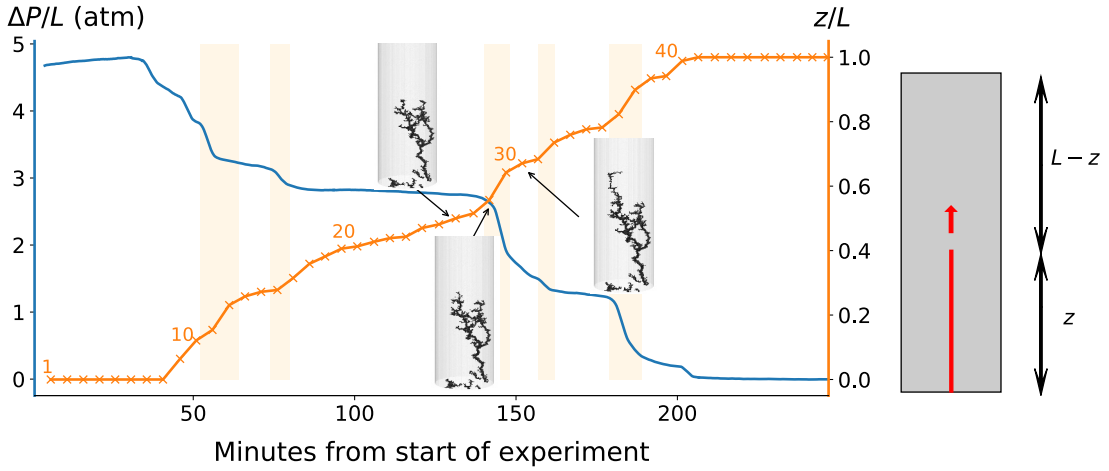

Figure 5.9: Experimentally measured pressure drop in the PZ103 sample as a function of time (blue solid line) correlated with the wormhole tip position determined from the tomographic images (orange line with an X marking the end time of the scan). Orange numbers next to points indicate scan numbers corresponding to Fig. 5.8.

φ_1, marked by light yellow bands in Fig. 5.10A. We also introduced a small region of very high porosity near the inlet of the sample (marked by a red rectangle), to trigger the growth of wormhole at this point. We then let the system dissolve (using the Darcy model described in Ch. 3) and record the advancement of the tip and evolution of the pressure drop in time. Fig. 5.10B shows marked similarities with analogous results for the experimental system, including long pressure plateaus during which the tip of the wormhole advances considerably. Interestingly, and somewhat surprisingly, the model calculation predicts acceleration of the growth rate as the wormhole tip penetrates the impermeable layers in the model. The cause of this is that within a packed layer it is harder for the wormhole to broaden because there is more mineral matter to dissolve around the perimeter [96]. A thinner wormhole results in higher flow velocities within it, in turn leading to a larger propagation velocity of the wormhole tip.

Tip position correlation to heterogeneity

Based on the 4D tomography results (Fig. 5.9) and theoretical considerations (Fig. 5.10), several questions arise: What is the real bulk pore-grain geometry of the sample? Are there any large-scale structures that can block the flow-paths? If so, do such structures correlate spatially with the wormhole tip position jumps?

To determine if such large-scale structures could be the permeability barriers postulated in our model (Fig. 5.10), we analyze high-resolution (30 µm voxels) tomographic images of PZ103 core prior to the dissolution, taken outside of the core holder. In X-ray tomography, image intensity represents the attenuation of matter to X-rays, which is proportional to its atomic number and density. Therefore, pixels of higher intensity correspond to regions with higher solid fraction or minerals with higher atomic numbers. For a rock dominated by one mineral (as is Pińczów Lime-

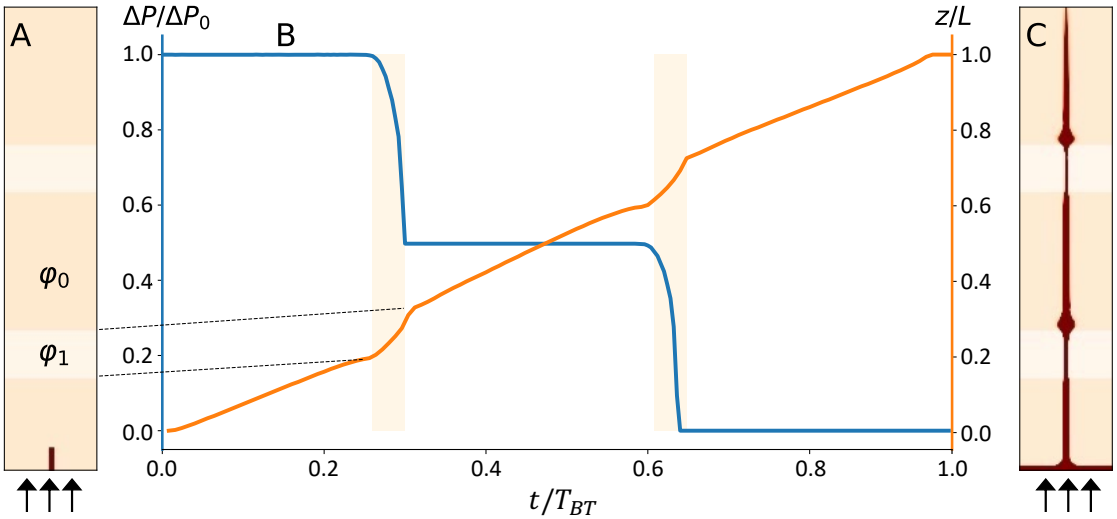

Figure 5.10: A simple numerical model of wormhole growth in a layered medium. (A) The general setup; a rectangular system of porosity φ_0 with two layers of porosity φ_1, with $\varphi_1/\varphi_0 = 0.1$. (B) The pressure drop in the system (blue) and the tip position (orange) as a function of time rescaled by breakthrough time (T_{BT}). (C) The final dissolution pattern with shades of red marking porosity (fully dissolved regions correspond to dark red areas). Jumps in tip position and permeability correlate in time, with tip jumps correlating with regions of lower permeability.

stone), a higher average intensity corresponds, therefore, to a higher grain density (and thus lower porosity). We prepare 2D projection plots by projecting the median values of 3D data in Y (Fig. 5.11A) and X (Fig. 5.11B) direction, respectively. Remarkably, we observe that the large-scale structures—loosely (reddish regions) and densely (bright yellow) packed regions— in both projections appear at the same location with the same orientation, almost perpendicular to the mean flow direction (i.e Z axis). The overlaid image of the wormhole on these projections reveals that the wormhole evolved through these regions as there was no way to bypass them. The competition between the two largest branches of the wormhole (frame 14-28 in Fig. 5.8) ends as the tip of one branch hits the second barrier of low-permeability. The wormhole abandons the growth of this branch and shows speed up in the winning branch (frame 29 in Fig. 5.8). This moment is captured in the pressure curve as the first bigger drop (large permeability increase) after a long plateau.

We also calculate the average grayscale intensity for successive slices perpendicular to the core axis. The data presented in Fig. 5.11C show quantifiable peaks, as determined by an automated peak detection algorithm [82], where average grayscale is higher than for the bulk of the rock. When wormhole tip displacement is juxtaposed with the average grayscale diagram, one notes that the wormhole propagation velocity increases in the peak regions, otherwise maintaining a steady velocity in the bulk of the rock (see Fig. 5.11D). This supports our hypothesis that wormhole propagation rate is controlled by the permeability barriers within the sample. While a peak at $z/L \approx 0.1$ does not necessarily correlate to acceleration in the tip position, and the acceleration at $z/L \approx 0.7$ does not seem to be correlated with a peak,

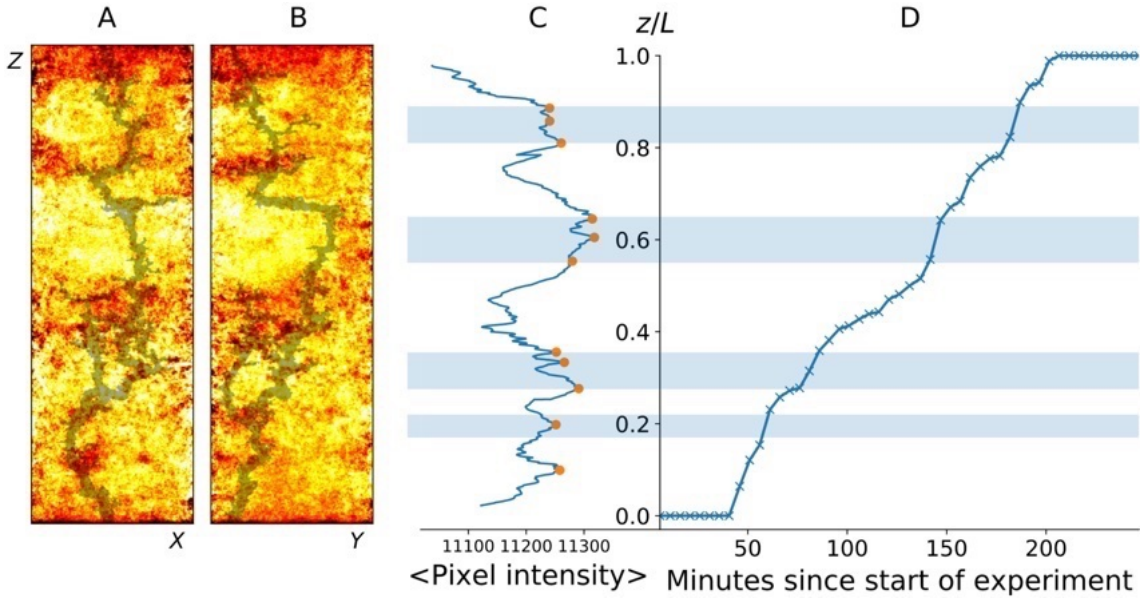

Figure 5.11: A and B show projected median grayscale values of PZ103 pre-dissolution scans in Y and X axis, respectively. Median values are derived from the high resolution, 30 µm initial scans, and are overlaid with the final wormhole geometry (blackish color) projected in the same axis. Red color in these plots corresponds to regions of less voxel intensity (more porous) while yellow/white corresponds to regions of more intensity (grains/crystalline calcite). C shows the average grayscale pixel intensity where the average is taken through the slices perpendicular to the core axis. The average intensities are spatially correlated to the tip position, z/L, (where $L = 115$ mm), plotted versus time (D). Large propagation velocities are associated with high average grayscale pixel intensity, a proxy for solid content. As the wormhole dissolves its way through the packed regions it remains a single channel with minimal branching, with branching and lateral movement occurring before entering the cemented regions.

these two features are relatively narrow and thus the respective correlations might be harder to detect.

Naturally, projecting the grain content information on Z-axis (as performed in Fig. 5.11C) considerably smears out the data on the 3D configurations of pores, grains, and positions of the micro-cementation regions. As a result, the overall variations in the grain content remain relatively small, on the level of a few percent. This is much smaller than the ones used in the toy model of Fig. 5.10 when the porosity in the cemented regions was 10 times smaller than that in the bulk of the rock. Since both the pressure drops and the wormhole speedups recorded during the experiment are substantial (Fig. 5.9), we conclude that the wormhole tip does encounter local, highly cemented structures that it needs to navigate around. or dissolve its way through. The coarse projection of Fig. 5.11C succeeds in picking up the most extended of these regions but—as already mentioned—misses a thinner one at $z \approx 0.7$, as marked in Fig. 5.9. It is important to point out here that these speed-ups are not related to the orientation of wormhole velocity with respect to

the mean flow direction (i.e Z axis) [41].

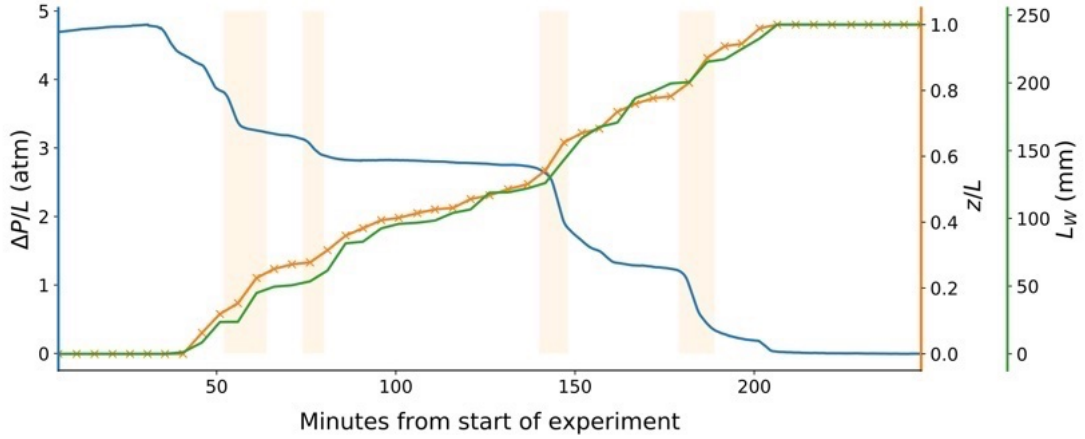

Figure 5.12: Comparison of PZ103 wormhole length (green curve) over time to z extent of tip (orange curve), rescaled by sample length (z/L). The pressure curve over time from this experiment is also shown (blue curve). As the wormhole is tortuous and migrates laterally, the wormhole length can be longer than the sample length (115 mm).

Finally, let us note that cemented regions in the core can have yet another impact on the wormhole advancement, as the wormhole might try to avoid the low permeability, crystalline portions by progressing laterally. In essence, the wormhole searches for an easiest to-dissolve pathway that would lead it through the barrier. This is a three-dimensional effect, not possible to represent in terms of our 1D toy model, since in the latter there is no possibility of bypassing the packed layers. As shown in Cooper et al. [41], this happens between frames 13–15, 30–31 and 33–35, i.e., just before the encounter with the cemented region. In the first and third cases (13–15 and 33–35) this lateral movement is also accompanied by an intense branching of the wormhole, as if it is probing different ways through the obstacle before finding the most effective one (see e.g. frame 34 in Fig. 5.8). The quantification of the lateral movement of the wormhole is provided by Fig. 5.12 which compares the axial movement of the wormhole tip (along Z) with the total movement. As observed, in the regions where $z(t)$ plot is almost flat (no axial advancement), there is still a noticeable advancement in the absolute length of the wormhole, $L_W(t)$. Note that the vertical scale on the two plots is different due to the large tortuosity of the wormhole (its absolute length is about two times larger than its extent in Z direction, thus the real slopes of the $L_W(t)$ line are about twice larger than the $z(t)$.

5.4.2 Tip evolution of a conical wormhole

We have also investigated the tip evolution of a conical wormhole in Pińczów limestone sample. Fig. 5.13 shows 3D visualizations of an evolving conical wormhole (PIN44). The setup of this experiment is similar to PZ103 case, except for the reactant molarity and injection rate. The sample was dissolved with 0.8M HCl at a low flow rate (0.175 ml/min), at which most of the acid is consumed near the inlet pores.

As discussed in Ch. 2, at this flow rate, the formed channel evolves slowly in the mean flow direction with a larger diameter near the inlet that gradually decreases along the length. Due to the slow progress of conical wormhole, the scanning was performed at a regular interval with relatively higher resolution (42 µm) compared to PZ103. The acquisition time for a full scan was around eight minutes, including seven minutes of scanning time and around one minute of resetting time of the X-ray source. However, the slow growth of this wormhole also resulted in significantly long breakthrough times. Therefore, the experiment was stopped before wormhole reached the outlet.

The obtained scans were processed similarly to PZ103 scans by first subtracting them from the initial scan and then isolating the wormhole using the volume-based segmentation method. However, due to large size of PIN44 time-series data with 52 scans—each of 42 µm voxel resolution and 13 GB in size—we downscaled the scans by a factor of four before processing. This resulted in the voxel resolution of each scan of around 168 µm at which—as we discussed in the resolution study (Sec. 5.3)—the PZ103 wormhole does not lose much details.

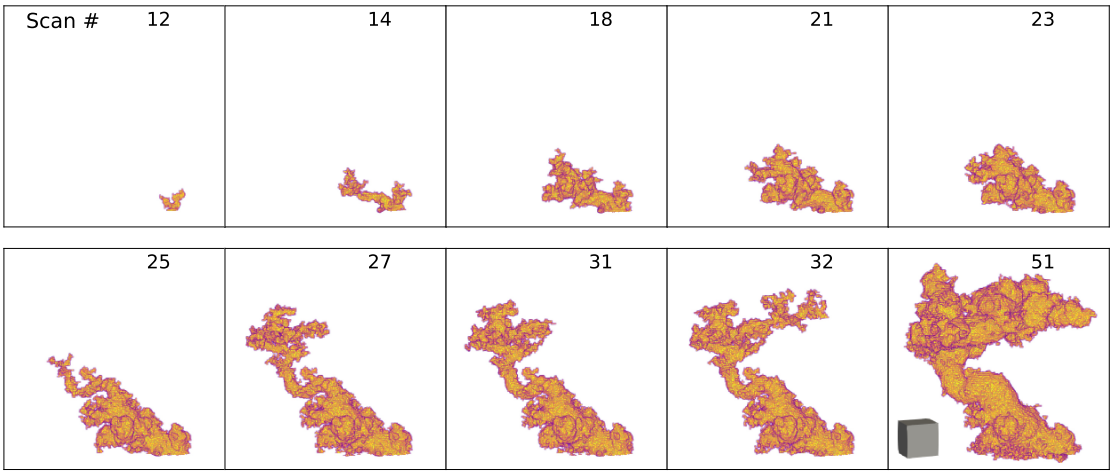

Figure 5.13: Projection of 3D rendering of a conical wormhole at different time instances showing the evolution of the wormhole in acidized PIN44 core. Rendered data is generated by subtracting a tomographic scan from the initial tomographic scan, and visualizing it in TomViz. The sample is half dissolved therefore all the renderings are cropped based on Scan-51 to improve the visualization. To represent the size of wormhole, a scaling cube of 3.4 mm sides is shown in Scan-51.

Fig. 5.14 shows the tip position movement of PIN44 conical wormhole. Similarly to the tip movement in the dominant wormhole (PZ103) that we discussed in the previous section, we observe a non-linear tip movement with jumps, plateaus, and changes in direction. This non-linear growth of conical wormholes has not been reported before. We argue that similar to the PZ103 case, it is correlated with local porosity layers, which act as permeability barriers. When the wormhole tip reaches

these layers, it moves rapidly through the layers, etching out its way and increasing the permeability of the system significantly.

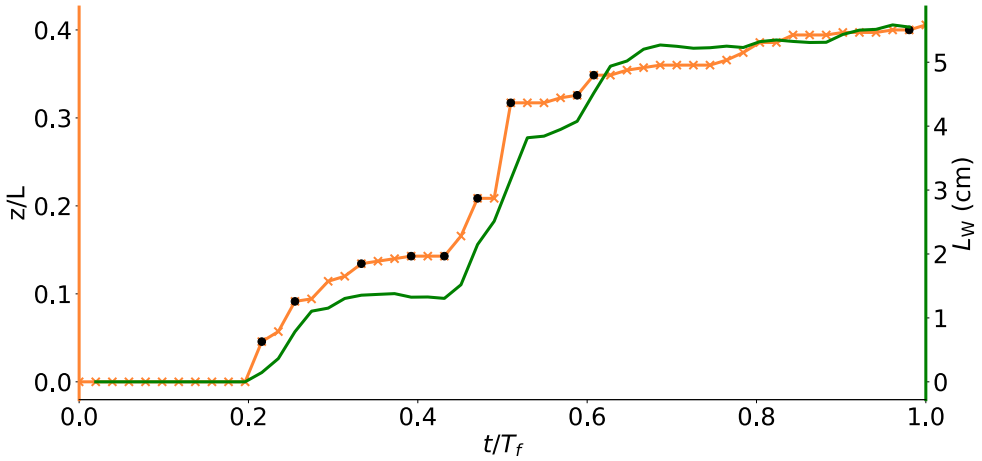

Figure 5.14: Tip position (orange line) and length (green line) of a conical wormhole (PIN44) measured from consecutive tomography scans. Black dots correspond to the scan numbers shown in Fig. 5.13. Note that the sample is half dissolved so the tip of the wormhole is almost halfway. However, the final length of the wormhole is approximately the same as the length of the sample (i.e. 6 cm)

5.4.3 Time evolution of geometrical characteristics

Continuing the line of research outlined in the previous section, we have performed time-lapse experiments to quantify the evolution of geometric properties of wormholes in several Pińczów and Wierzbica rock samples. The experiments involved five dominant-type wormholes including four Pińczów and one Wierzbica wormhole. The details of specimens and experimental parameters related to these experiments are given in Tab. 5.4. The table also shows the specifications of time-series scans taken at different time resolutions for different experiments. All these experiments

Sample	Length (cm)	Diameter (cm)	Injection rate (ml/min)	Scan resolution (µm)	Wormhole type
PZ103	11.4	3.8	1	169	Dominant
PIN43	6	3.9	0.5	42	Dominant
WB10	12.1	3.8	1	60	Dominant
PZ08	11.8	3.8	0.5	30	Dominant
PIN02	2.5	1.5	0.18	70	Dominant

Table 5.4: The characteristics of dissolution experiments, which are scanned at regular time intervals as a time series

are processed using the methodology described in the previous section (Sec. 5.2.4), and the extracted wormholes are used to measure the geometrical properties defined in Sec. 5.2.5.

Fig. 5.15 shows the time evolution of tortuosity (τ) of dominant-type wormholes as a function of the tip position rescaled by the respective core diameter (z_{tip}/d_0). We observe that in PZ103 and PIN43 experiments, initially, the wormhole tortuosity sharply increases, before reaching an asymptotic value around which it oscillates until the wormhole reaches a certain length. However, for other samples—WB10, PIN02, and PZ08—this behavior is not observed, which may be due to the time-frequency of the data not being high enough to capture the early stages of wormhole growth. Therefore, these results should be treated with a certain degree of caution.

For both WB10 and PIN02 wormholes, the first available scan shows that the wormhole has already reached a length where tortuosity is in the asymptotic regime. This can be inferred from Fig. 5.15 where the points of WB10 and PIN02 do not exhibit much spread. Therefore we will use them in calculating the mean and relative variance of tortuosity. On the other hand, for PZ08 we do not see stabilization, so we cannot infer anything about the asymptotic regime from this data.

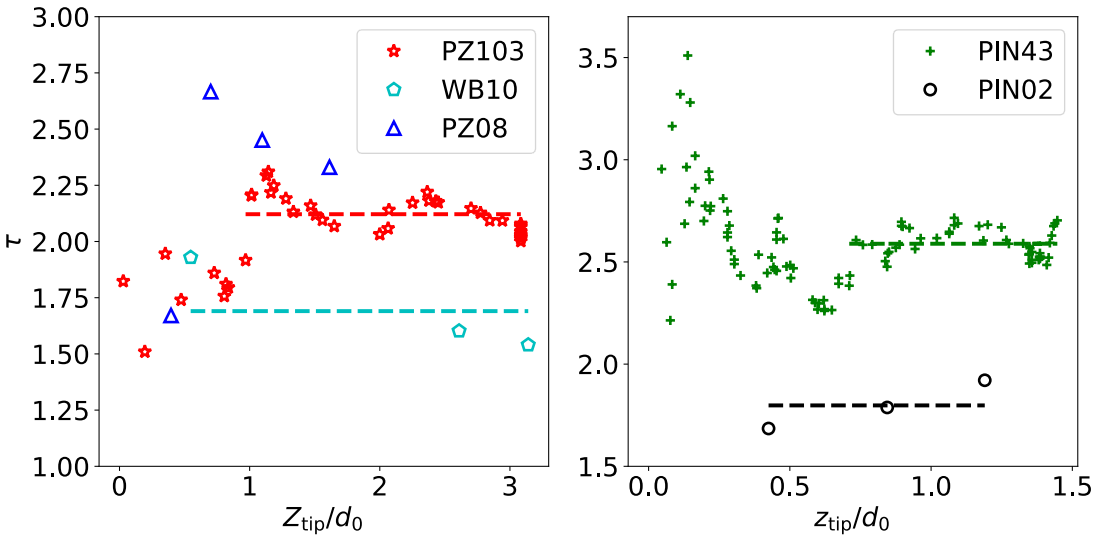

Figure 5.15: Time evolution of tortuosity of dominant type wormholes in time-series dissolution experiments with full-length samples ($\approx$ 11 cm) (left) and smaller samples ($\leq$ 6 cm) (right). Dashed lines are fitted, and their color corresponds to the respective points of the same color.

To determine the wormhole length at which tortuosity stabilizes, we fit a horizontal line from the end of the curve (rightmost point) and extend it backward as far as possible, down to the smallest z_{tip}/d_0 while imposing a criterion that keeps point deviations from the line within an acceptable range. For tortuosity, the maximum deviation is set to 0.1. The calculated values, presented in Table 5.5, show that Wierzbica wormhole (WB10) is characterized by the smallest asymptotic tortuosity ($\approx$ 1.6), while the Pińczów wormholes are more tortuous.

To study the time evolution of the overall wormhole structure, we have investigated length wastefulness (W_{L}) as a function of z_{tip}/d_0 (Fig. 5.16). The length wastefulness of all four wormholes (PZ103, PIN43, PIN02, and WB10) exhibits a behavior

Table 5.5: Asymptotic values of wormhole tortuosity in Fig. 5.15

Sample name	Fit interval	Mean (μ)	Relative standard deviation (σ/μ)
PZ103	$0.97 - 3.08d_0$	2.121	0.064
PIN43	$0.71 - 1.45d_0$	2.589	0.027
PIN02	$0.42 - 1.19d_0$	1.798	0.054
WB10	$0.55 - 3.14d_0$	1.690	0.101

similar to tortuosity, reaching an asymptotic value after initial fluctuations. The only exception is PIN43, whose W_{L} stabilizes earlier than tortuosity.

To quantify the asymptotic behavior of W_{L} curve, we used a line fitting method similar to that for tortuosity. The calculated values are given in Table 5.6. Note that PZ08 shows no stabilization; therefore, we did not include it in the calculation. We observe that WB10 wormhole shows the smallest mean length wastefulness while PIN43 has the highest value. Overall, Pińczów wormholes have higher W_{L} than Wierzbica wormholes, which aligns with the observation made for tortuosity (Table 5.5). We believe that this difference is correlated to the large-scale structures of Pińczów and Wierzbica limestone, a topic we will discuss in later sections.

Table 5.6: Asymptotic values of wormhole length wastefulness in Fig. 5.16

Sample name	Fit interval	Mean (μ)	Relative standard deviation (σ/μ)
PZ103	$1.1 - 3.08d_0$	10.71	0.102
PIN43	$0.45 - 1.45d_0$	12.12	0.075
PIN02	$0.42 - 1.19d_0$	4.195	0.196
WB10	$0.55 - 3.14d_0$	3.164	0.095

From this study, we can conclude that the geometrical characteristics of the dominant wormholes in Pińczów limestone stabilize as the length of the wormhole increases. Both tortuosity and length wastefulness of Pińczów wormholes stabilize for the tip positions between $0.4d_0$ and $1.0d_0$. Experiments with more available data, where wormholes are scanned at high temporal resolution, exhibit a relative dispersion below 10%. This suggests that the geometric measures, such as tortuosity or length wastefulness, are well-defined, represent stable characteristics for long wormholes, and can be used to differentiate between wormhole structures.

5.4.4 Analysis of post-experiment wormhole geometries

While the previous section was devoted to the time-dependent characteristics of the wormhole, which are challenging to obtain due to the need for 4D tomography data, this section analyzes the geometry of wormholes from post-experiment scanning, where significantly more data is available.

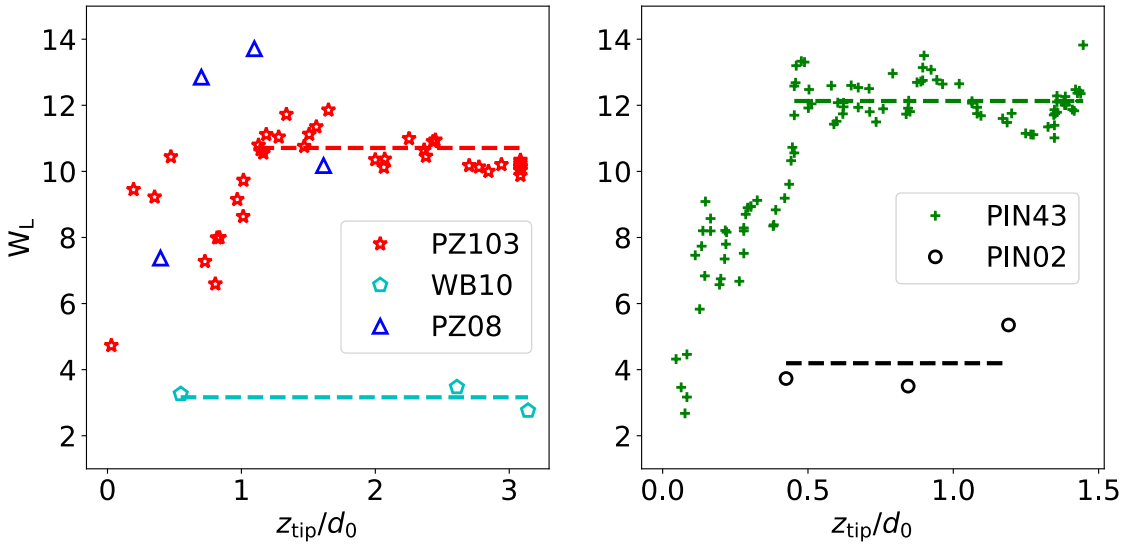

Figure 5.16: Time evolution of length wastefulness of dominant type wormholes in time-series dissolution experiments with full-length samples ($\approx$ 11 cm) (left) and smaller samples ($\leq$ 6 cm) (right). Dashed lines are fitted, and their color corresponds to the respective curve of the same color.

Effect of rock structures on wormhole shape

To investigate the effect of rock structures on wormhole shape, we have studied the wormholes formed in both Pińczów and Wierzbica rock samples at 1ml/min injection rate. At this flow rate, multiple wormholes initially form, but one soon outcompetes the others and continues to grow toward breakthrough. As mentioned previously, in our experiments the secondary wormholes are relatively small. Therefore, in the analysis, we have only included those secondary wormholes whose lengths are larger than one-third of the respective sample diameter ($> d_0/3$). Fig. 5.17 and 5.18 show the extracted dominant channels in different samples of Pińczów and Wierzbica rocks. Despite being formed in the same physical conditions, the wormholes formed in these rocks are visually very different, indicating the effect of rock structures. Wormholes in Wierzbica limestone are relatively straight with minimal branching, in contrast to the highly tortuous and extensively branched wormholes in Pińczów limestone.

To quantify the differences in wormhole shape, we have calculated tortuosity (τ) and length wastefulness (W_L) for all the wormholes in both type of rocks. Fig. 5.20 shows the τ vs W_L plot for these wormholes. Remarkably, we observe the clustering of data points based on the rock type. Points corresponding to Pińczów wormholes are grouped separately, exhibiting higher tortuosity and length wastefulness, with mean values of approximately 2 and 10, respectively. In contrast, Wierzbica wormholes cluster around lower values, showing a mean tortuosity of $\approx$ 1.75 and a mean wastefulness (W_L) of $\approx$ 6. We have also compared the relative deviations of these

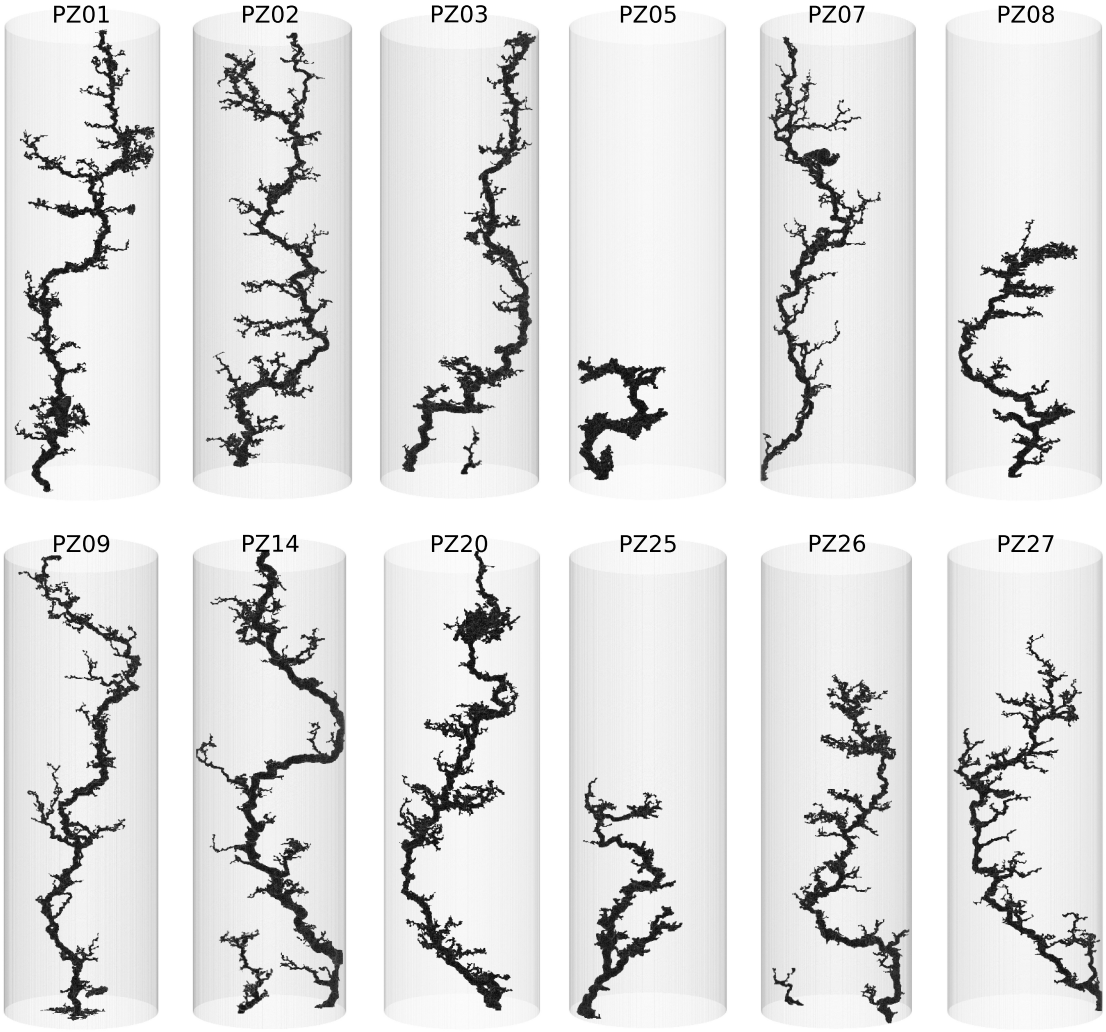

Figure 5.17: Post experiment dominant type wormholes in Pińczów rock samples. Most wormholes have broken through to the outlet, except for PZ05, PZ08, and PZ25–PZ27, where the experiments ended before breakthrough. Secondary wormholes are also shown in PZ03, PZ14 and PZ26

Table 5.7: Mean and relative deviation of post-experiment wormhole measures used in Fig. 5.20

Rock type	Measure	Mean (μ)	Relative standard deviation (σ/μ)
WB	τ	1.746	0.131
PZ	τ	2.102	0.043
WB	W_L	5.88	0.26
PZ	W_L	9.81	0.257

values (Table 5.7) with time series experiments (Table 5.5 and 5.6). We observe that the relative deviation of τ in both types of experiments is similar for both rocks, while the relative deviation of W_L is larger in post-experiment wormholes.

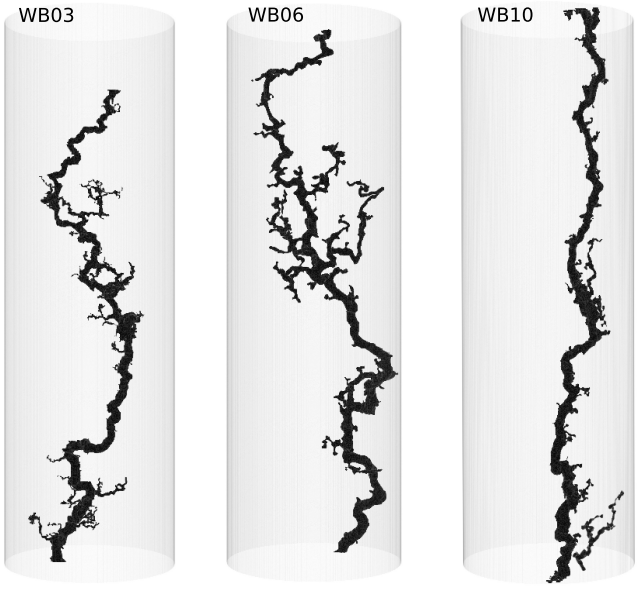

Figure 5.18: Post experiment dominant type wormholes in Wierzbica rock samples. WB06 and WB10 wormholes reached the outlet of the sample while for WB03 the experiment was stopped before the breakthrough. A secondary wormhole is also shown in WB10.

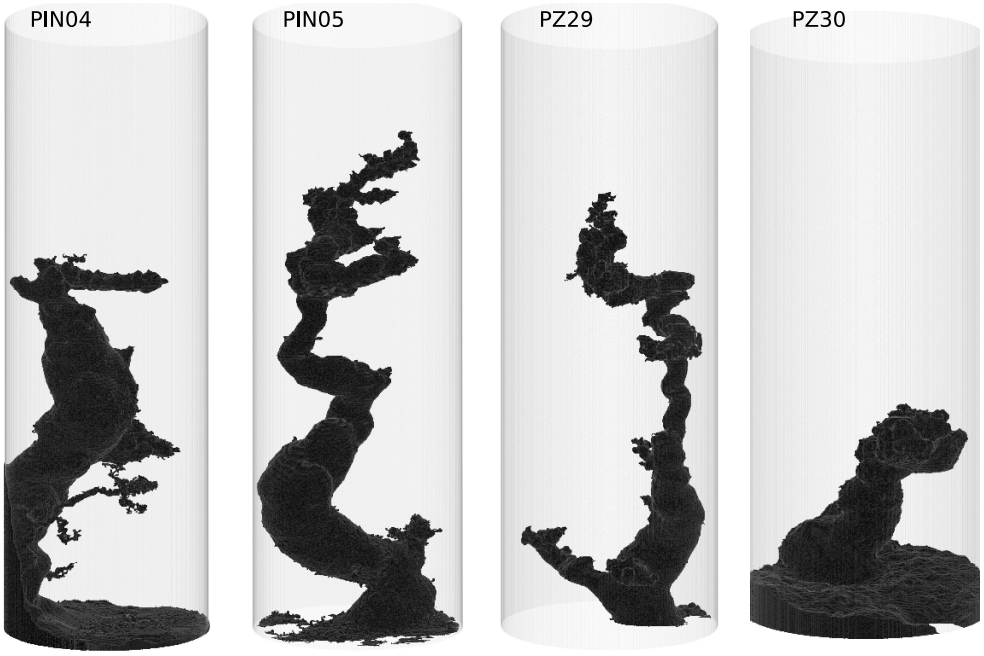

Figure 5.19: Post experiment conical type wormholes in Pińczów rock samples. Due to the longer duration of these experiments, all the experiments were stopped before the wormhole reached outlet.

This could be the result of the formation, growth, and eventual termination of large secondary branches or the formation of large secondary wormholes. In most of our experiments, including time series, the secondary wormholes did not reach signifi-

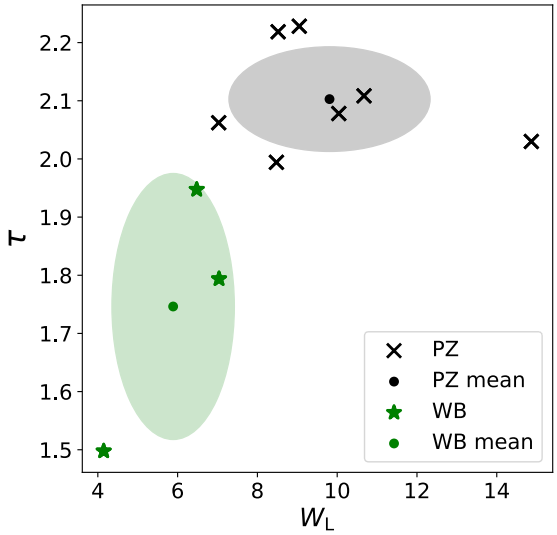

Figure 5.20: Tortuosity vs length wastefullness (W_L) plot for final dominant wormholes in Wierzbica and Pińczów samples. All samples used here are dissolved at 1 ml/min flowrate. The dots represent the mean of the geometric properties of a rock, while the colored ellipses show the standard deviation of the properties of a rock

cant length ($> d_0/3$). However, WB10, PZ03, PZ14 and PZ26 samples produced large secondary wormholes. PZ14 sample has the largest secondary wormhole and the resulting W_L is also the highest (≈ 14.5) among all other experiments. This indicates that the formation of large secondary wormholes can produce a larger variance, compared to the experiments where the secondary wormholes are small.

Table 5.8: Mean and standard deviation of porosity measured from tomography images

Rock type	Mean (μ)	Standard deviation (σ)
WB	23.309%	0.093
PZ	27.085%	0.031

The differences between the geometric measures (τ and W_L) of Pińczów and Wierzbica wormholes can be explained by analyzing rock structures. Earlier, in Sec. 5.4, we have seen that a Pińczów sample, PZ103, has packed cemented regions that are mostly perpendicular to the mean flow direction (Fig. 5.11) i.e the normal vector is close to $(0, 0, 1)$. These regions act as a potential barrier that a wormhole either navigates around or dissolves its way through. Once entering inside the packed region, the wormhole moves quickly and spends less time there compared to when going through loosely packed regions. This also influences the overall shape of the wormhole as PZ103 wormhole. We believe that this is the case for most of the Pińczów wormholes as all the Pińczów samples are taken perpendicular to the bedding plane. However, the Wierzbica samples were not taken perpendicular to the bedding layers but at an arbitrary angle. The 2D projection plots (Fig. 5.21) of WB10 sample reveals that the layers are nearly perpendicular to Y axis, i.e. the normal vec-

tor $(\mathbf{n_x}, \mathbf{n_y}, \mathbf{n_z})$ is such that $|\mathbf{n_x}||\mathbf{n_z}| \ll |\mathbf{n_y}|$. Contrary to PZ103 wormhole, which evolves by going through less and more packed regions, WB10 wormhole advances along a less packed layer (Fig. 5.21A). This layer provides a path of less resistance (high permeability). As a result, wormhole prefers to move quickly through the layer, restricting the lateral movement. This not only reduces the amount of branches but also decreases the tortuosity of the wormhole. That is why WB10 wormhole shows least amount of branching ($W_{\mathrm{L}} = 3.164$) and the smallest tortuosity ($\tau = 1.690$) among all other wormholes, including Pińczów wormholes.

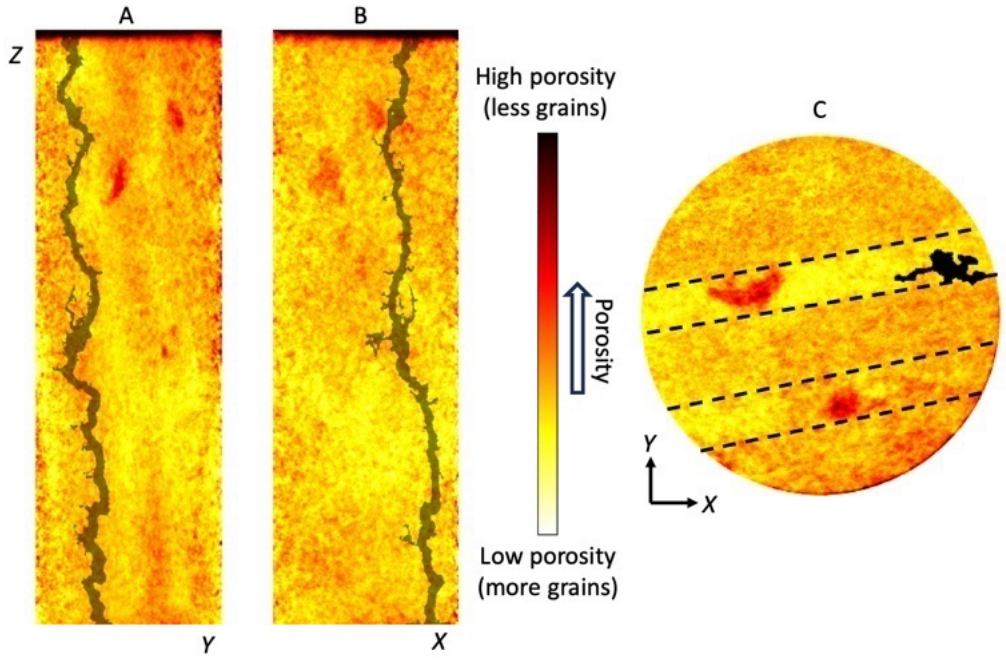

Figure 5.21: 2D projections of WB10 pre-dissolution scans by median grayscale values in X (A), Y (B), and Z (C) axis respectively. Median values are derived from the high resolution, 30μm initial scans, and are overlaid with the final wormhole geometry (blackish color) projected in the same axis. Darker red color in these plots corresponds to regions of less voxel intensity (more porous) while yellow/white corresponds to regions of more intensity (grains/crystalline calcite). Packed layers are visible in X axis projection (A) and Z axis projection (C) in which the layers are highlighted by dashed lines.

To quantify the differences between the rock structures of PZ103 and WB10 samples, we have calculated the voxel intensity-based auto-correlational function (ACF) in X, Y, and Z directions for both samples. The definition of ACF is similar to Cooper et al. [41].

$$\mathrm{ACF}(\mathbf{l}) = \frac{\langle (I(\mathbf{r}+\mathbf{l}) - \mu)\,(I(\mathbf{r}) - \mu)\rangle_{\mathbf{r}}}{\langle (I(\mathbf{r}) - \mu)^2 \rangle_{\mathbf{r}}}, \tag{5.1}$$

where $I(\mathbf{r})$ is a grayscale value at point $\mathbf{r}$ within a sample and $\langle \dots \rangle_{\mathbf{r}}$ denotes averaging over $\mathbf{r}$. Finally, $\mu = \langle I(\mathbf{r}) \rangle_{\mathbf{r}}$ is the average grayscale value. While computing

ACF($\mathbf{l}$) in a specific direction (i.e X, Y or Z) the vector $\mathbf{l}$ can be replaced by the directional vector.

Fig. 5.22 shows the absolute values of calculated ACF for both PZ103 and WB10 samples. Remarkably, the fingerprints of the packed layers are evident in these plots. PZ103 has layers perpendicular to Z direction, resulting in an initial decay of ACF along Z-axis followed with an increase as it enters in differently packed layer (see Fig. 5.22 left). This increase reflects anti-correlation between layers (less or more packed regions) i.e. ACF becomes negative here. WB10, on the other hand, has packed layers with a normal vector oriented approximately along the Y axis, which results in a very slow decay of the correlation function along both X and Z. Note that in this case, the correlation function does not decay to zero, which reflects the presence of persistent large-scale heterogeneity and the non-ergodic nature of the system (the mean value of porosity in the packed layer is different from the mean porosity in the less packed region). However, for Y-axis, the calculated ACF of WB10 shows a periodic behavior (Fig. 5.22 middle). After an initial decay it becomes negative (anti-correlated layer) then around 1 cm it becomes positive while going through a correlated layer, following which it enters in a second anti-correlated layer around 1.8 cm (negative ACF). This highlights the similarity in the behavior of the grayscale auto-correlation function for the WB10 sample along the Y-axis and PZ103 along the Z-axis, as both exhibit packed layers with a normal vector along these directions.

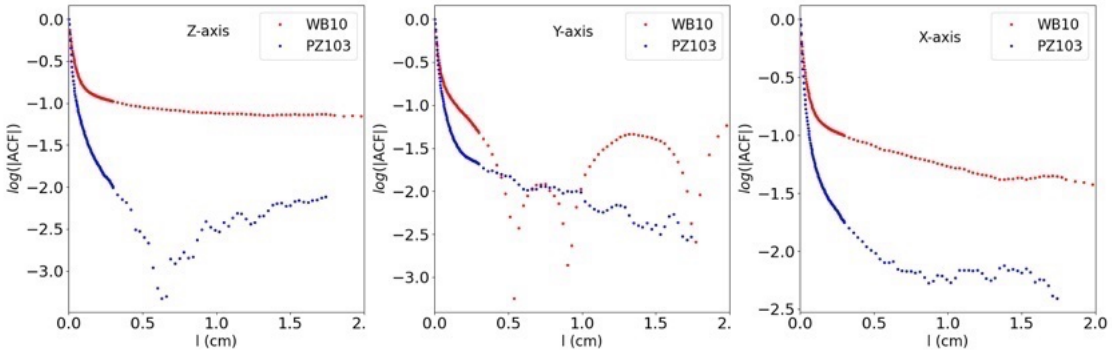

Figure 5.22: Comparison of directional auto-correlation function (ACF) in PZ103 (blue curve) and WB10 (red curve) samples. Note that we are plotting absolute values here. The left panel shows ACF in Z direction, while the middle and right panels show in Y and X directions, respectively. ACF in these plots is calculated on a 2 cm cubic section which is cropped from 30 µm resolution scans.

Effect of flow rates on wormhole shape

To study the effect of flow rate on the geometry of wormholes we conducted dissolution experiments on Pińczów cores at flow rates ranging from 0.175 ml/min to 4 ml/min. Following these experiments, we analyzed the geometric characteristics of the resulting wormholes shown in Fig. 5.17 and 5.19. As discussed in Ch. 2, lower

flow rates in wormholing regime result in the formation of conical channels, while at moderate flow rates, multiple wormholes compete, and one dominates, resulting in a thinner channel with slight branching which increases with the flow rate [37, 38, 191]. Figures 5.17 and 5.19 confirm such a dependence of wormhole shape on the flow rates. However, contrary to previous studies [38, 43, 191] that lacked 3D information of the shape of conical wormholes, we observe highly tortuous structures with reduced number of small branches and extended main pathways. This is most probably, as we discussed earlier, due to the presence of packed layers in Pińczów samples. Furthermore, the conical wormhole while growing has extensive periods where it does not elongate but simply increases its diameter. In these periods it "swallows" the shorter side branches. We will quantify these observations using the geometric properties below.

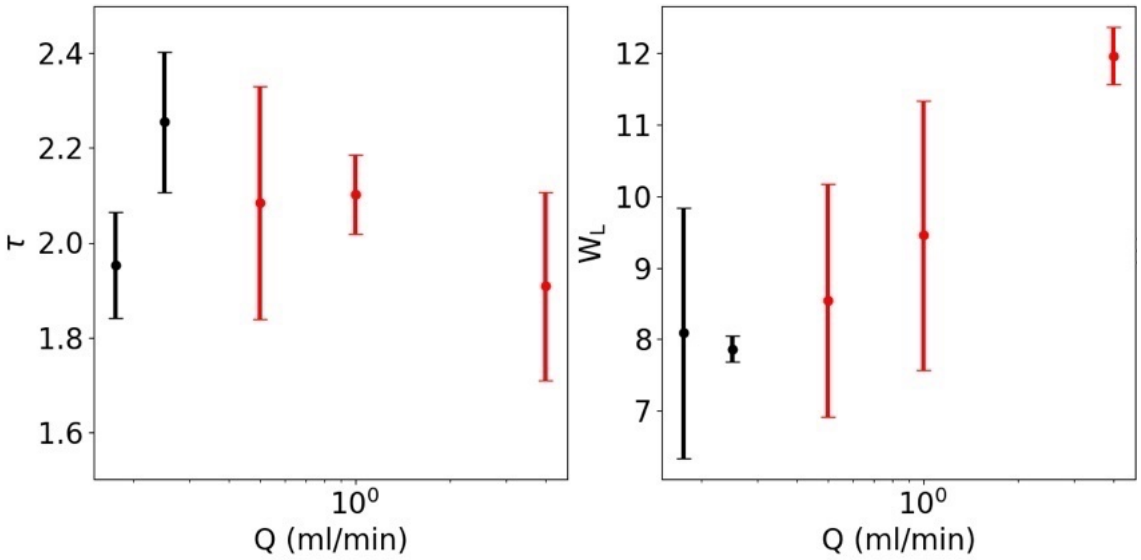

Figure 5.23: Geometric characteristics of post-experiment wormholes vs injection rates. All the wormholes used in this plot were formed in Pińczów limestone samples. The data related to conical wormholes is shown in black color while for dominant wormholes red color is used.

Fig. 5.23(left), shows the variation of tortuosity with injection rates. We observe that the tortuosity of Pińczów wormholes does not exhibit any clear dependence on flow rates. This is a rather surprising result and is in contrast to the results of Li et al. [52], who observed a dependence of tortuosity on injection rates in the wormholes formed in plaster of Paris cores. It is also consistent with our observations made in Fig. 5.17 and 5.19, where Pińczów conical wormholes are as tortuous as the dominant wormholes. We argue that it is connected to the characteristics of a particular rock. Pińczów rock is known to be very heterogeneous [41, 190], in comparison to laboratory-made plaster of Paris, which is relatively homogeneous [45, 52]. Moreover, Pińczów samples used in Cooper et al. [41] are reported to have layers of varying porosity with abundant fossils, which contributes to the tortuosity of both the existing flow paths and the wormholes.

Finally, we have investigated the effect of flow rate on length wastefulness, W_L.

Fig. 5.23 (right) shows that W_L is nearly constant for conical wormholes while for dominant wormholes it keeps on increasing. Note that increasing W_L indicates an increase in the amount of branching—the number of branches and their length—in a wormhole. Conical wormholes ($Q \leq 0.25$ ml/min) show the lowest W_L (≈ 8), which means that they have the lowest number of branches. This is evident in Fig. 5.19, where we observe fewer branches compared to dominant wormholes (Fig. 5.17), which have a higher number of branches.

5.5 Conclusions

In this chapter, we presented a novel data analysis approach to study the growth dynamics of wormholes in dissolving limestone rocks. More specifically, we developed a volume-based segmentation method with a self-adjustable threshold, relying on a connected component algorithm to extract the wormhole shape from tomography images. We also proposed geometric measures to quantify the shape of three-dimensional wormholes. These methods provided new insights into the effect of specific rock characteristics, such as low porosity layers, on the tip advancement of a wormhole, as well as how the rock structures and injection rates can affect the overall shape of wormholes.

The tip movement study showed that the growth of the wormhole in a real limestone rock can be more complex than simple proportionality of the driving pressure and tip displacement predicted by a typical model which assumes micro-structural homogeneity [45, 46, 52, 91]. In our sample, we observed temporal plateaus alternated with larger drops in pressure, which correlate well with the predictions of a conceptual model that assumes a layered porosity distribution. The toy model reproduced the general character of the observed pressure curve (Fig. 5.10), and predicted speedups of wormhole tip. The high temporal resolution of the 4D tomography technique used here enabled the capture of wormhole growth characteristics corresponding to temporal variation of the driving pressure. This made it possible to test the permeability barrier model and show that tip velocity increases as the wormhole penetrates the barrier. The observed spatial correlation of wormhole tip propagation velocity with average grayscale intensity indicates that regions which contain large structures, such as impermeable fossils, act as barriers to reactive flow. As confirmed in the numerical model, tip velocity increases as the wormhole penetrates these barriers.

The quantification of evolving wormhole geometry using the proposed geometric measures, such as tortuosity and length wastefulness, reveals that these measures approach an asymptotic value as the dominant wormhole elongates. For PZ103 and PIN43 wormholes, where enough time series scans are available, this behavior is observed within 10% relative standard deviation when the wormhole reaches a length equal to the sample diameter. However, for the wormholes with a limited number of scans, the relatively standard deviation is higher ($10 - 20\%$). The tendency of our geometric measures to approach well-defined values for sufficiently long wormholes suggests that these measures can reliably characterize different wormhole structures.

We also investigated the effect of rock structures on the shape of post-experiment wormholes. The comparison of tortuosity and length wastefulness of Pińczów and Wierzbica wormholes—formed at 1ml/min flowrate—led us to conclude that these measures can serve as characteristics of rock structures. The geometric measures showed that Wierzbica wormholes, on average, are relatively straight and have fewer branches compared to Pińczów wormholes. On investigating the differences between these measures of Wierzbica and Pińczów wormholes, we found that rock structures such as packed regions have a significant effect on wormhole shape. WB10 sample has packed layers of low porosity with a large normal vector in Y direction, contrary to Pińczów samples where the layers have the normal vector in Z-axis. The result of the different orientation of these layers is that WB10 wormhole evolved in a less packed region of higher permeability (almost parallel to the layer), completely ignoring crossing the densely packed region. On the other hand, PZ103 wormhole was growing in a setting where the layers were oriented perpendicular to its growth direction, hence it could not bypass them. These observations are confirmed by comparing the 2D projection plots of 3D rock matrix and directional auto-correlation functions of PZ103 and WB10 sample.

The results of this study can be generalized to all Pińczów and Wierzbica samples, where PZ103 is the representative of all of the Pińczów samples, since they were cut perpendicular to the bedding. On the other hand, WB samples had random orientation, which means that in most cases, the layers would not block the wormhole completely, and it can propagate along the less packed regions without crossing it, resulting in the structures of smaller tortuosity than those of Pińczów limestone. Note that these different behaviors and geometric characteristics are thus the combination of the rock properties (presence of the layers) and the sample preparation (orientation of the cores), where Pińczów samples are just an extreme case of sample/layer orientation, i.e. perpendicular to the mean flow direction.

Finally, we conducted a study to examine the effect of varying injection rates on the wormhole shapes. This study reveals that there is no dependence of the tortuosity of the Pińczów wormholes on flow rates, indicating that conical wormholes are as tortuous as dominant ones. This observation further supports our argument that wormhole tortuosity is a characteristic feature of rock structures. However, the length wastefullness does show a direct dependence on injection rates and increases with it. This result is aligned with other studies [37, 38, 191] where increasing flow rate (or decreasing $\mathrm{Da}_{\mathrm{eff}}$) resulted in the transition from conical wormholes (which have a small number of branches) to a ramified regime, where many parallel flow paths develop.

Chapter 6

Effects of mixing at pore intersections on large-scale dissolution patterns

The poet's task is to bring together the disparate elements of experience, to mix them into something that sings.

T. S. Elliot

6.1 Introduction

In this chapter, we will turn our focus toward the pore-scale mixing processes and their effects on network-scale dissolution patterns. This chapter also contains a set of new findings which are published in a peer-reviewed journal article [138].

Dissolution patterns are commonly observed at macro-scales, while they are the result of micro-scale reactive transport processes. The chemical reactions occur at the rock surface, which, coupled with reactant transport via advection and diffusion, govern the dissolution process. On the other hand, the magnitude of the flow and the concentration profile in the sample are global in nature and depend on the existence of dominant flow paths and large-scale heterogeneities. The coupling between micro and macro scale processes could influence the dissolution process, especially in the unstable regime, where the existing flow paths compete, and the dominating one gets amplified [53, 54].

Realizing the importance of pore-scale processes in the formation of large-scale dissolution patterns, several researchers conducted studies to understand their effects and showed that macroscopic reactive transport can be influenced by pore-scale mixing [57–59] and pore-scale properties such as mineral distribution and pore network structure [56, 77]. Pore-scale mixing plays a crucial role in reactive flows, controlling the transport of reactants at pore surfaces and the reactions induced by mixing processes [192]. Particularly, the mixing at fracture intersections and pore junctions has attracted considerable interest because the intersections are the places where

vigorous mixing and reactions between different fluids take place [65, 193, 194]. For instance, Bochet et al. [195] and Lee and Kang [64] have identified the fracture intersections as the hotspots for potential biogeochemical reactions. Additionally, previous studies have indicated that the degree of mixing at pore intersections can influence solute spreading at large-scale [61–63]. This suggests that the dissolution patterns could be influenced by mixing at pore-intersections, with recent findings showing a wide range of mixing conditions can occur at these places [64, 65]. Nevertheless, the traditional network scale dissolution models [56, 66], described in Ch. 3, assume a full mixing of reactant concentrations at pore-intersections. This is due to the absence of a universal, coarse-grained mixing rule to quantify the degree of mixing at intersections.

To tackle this issue, we will use the pore network model introduced in Ch. 3 with one exception. Instead of considering only the traditional full mixing condition which assumes that the solute transport at pore junctions is diffusion-dominated and the reactive solute becomes well mixed, we will also use streamline routing. This type of mixing assumes that the reactant transport is advection-dominated, and the solute is carried by streamlines without transitioning between them. As a result, the latter leads to partial or no mixing of incoming reactant concentrations. We have implemented both mixing conditions at pore junctions in the network model of a dissolving porous medium.

In Sec. 6.3, we will describe in details a general formulation of streamline routing. The formulation is inspired by Kang et al. [62] and is based on the calculation of flow fractions at an intersection with four connected pores. The results will be presented in Sec. 6.4 with a quantitative and qualitative comparison of dissolution patterns formed by both types of mixing. In addition, we will also compare breakthrough curves, which are important in petroleum reservoir stimulation, where the key emphasis is on the amount of reactant required for the breakthrough. In this study, we found that the interplay between network heterogeneity and mixing strongly affects the macroscopic dissolution patterns, and the underlying mechanism is highlighted.

6.2 Pore network model

We use a network model similar to the one described in Ch. 3, in which the porous rock is represented as a network of cylindrical capillaries (of initially heterogeneous sizes) that are broadened by the dissolution [37, 56, 66]. The nodes of the network (pore junctions) are assumed to be volumeless such that all the reactions take place in the capillaries (pores) only. A rhombic (diamond) lattice is used to create a network for which the nodes are placed on a regular lattice with the link length of constant l_0, as shown in Fig. 6.1(a). Such geometry with four branch intersections is particularly well suited to study the mixing effects [196–198]. In the limiting case of short residence times at the intersection and uniform pore diameters, the two incoming tracer streams will remain unmixed in this geometry. Heterogeneity in the network is introduced by assigning each pore an initial diameter according to a log-normal distribution, generated with mean d_0 and the variance of hydraulic conductance σ^2. A wide range of σ^2 is considered to study the effects of initial

network heterogeneity. The reason to choose a log-normal distribution in this study is its ubiquity in many natural systems [199]. In the generated network, the reactive fluid enters through the set of N_y inlet nodes (see Fig. 6.1a) where the pressure $p_{\text{in}}(t)$ is imposed, and leaves through outlet nodes where the pressure is kept at zero, $p_{\text{out}}(t) = 0$. The inlet pressure is adjusted in each time step to keep the total volumetric flow rate through the system, Q_0, constant. Periodic boundary conditions are applied along the lateral direction.

A fixed value of Sherwood number, Sh(= 5) and parameter G (= 1) is used in this study. In our model, the geometry of each pore is circular, for which the approximation of Sh = 5 is well in the asymptotic limits of higher Sh= 4.861 and lower Sh= 5.385 reaction rates [148]. The rationale for choosing a fixed value of G, as shown by Budek and Szymczak [66], is that the influence of varying G on dissolution patterns is less significant than the effect of Da_{eff}. Moreover, $G = 1$ implies a mixed transport and reaction control on the dissolution rate, which is similar to the conditions of acidization experiments. For example, in the case of the dissolution of Indiana limestone using hydrochloric acid, the surface reaction rate $k = 0.2$ cm/s yields $G \approx 0.7$, close to $G = 1$ adopted here.

6.3 Incomplete mixing

We have discussed full mixing in Sec. 3.2.3, where it was assumed that the solute has a longer residence time at pore intersections to mix completely. However, in the case of shorter residence time (corresponding to higher flow rates), the mixing is incomplete, with a considerable portion of reactant following the streamlines. In the limit of negligible residence time, the incoming reactant concentrations do not mix at all and follow the streamlines as depicted in Fig. 6.1c. The choice of mixing protocol in a given physical situation depends on the local Péclet number characterizing the flow through the intersection, Pe_{int}. This number is equal to the ratio of the advective travel time through the intersection, d_{int}/v, to the respective diffusive time, d_{int}^2/D, with d_{int} – a characteristic size of an intersection. The intersection Péclet number is then $\text{Pe}_{\text{int}} = d_{\text{int}}v/D$, with $\text{Pe}_{\text{int}} > 1$ leading to streamline routing, and $\text{Pe}_{\text{int}} \ll 1$ defining the range over which full mixing assumption should work well. In natural and laboratory systems, one encounters a large range of Pe_{int}. Taking as an example acidization of Indiana limestone [37], where v is in the range $0.05 - 5$ cm/s, $D = 3.6 \times 10^{-5}$ cm^2/s [38] and $d_{\text{int}} \approx 5\mu m$ [200], we get Pe_{int} in the range $0.5 - 50$, depending on the flow rate used. On the other hand, groundwater flows in natural rocks are much lower, usually in the range $10^{-8} - 10^{-5}$cms^{-1} [201], which leads to $\text{Pe}_{\text{int}} \ll 1$. A substantially different situation is encountered for the dissolution of rock fractures or bedding planes. Such systems can be simulated using the present model, with the 2D network of channels then representing the flow paths in the fracture plane around the asperities. Fracture apertures are between 0.005cm and 0.1cm [202–204], and hydraulic gradients are of the order of 10^{-3} to 10^{-1} [205, 206]. This gives a range of characteristic flow velocities in undissolved fractures from 10^{-4}cm/s to 1cm/s. The corresponding intersection Péclet numbers are then $0.05 < \text{Pe}_{\text{int}} < 10^4$, taking the fracture aperture as the characteristic

intersection size and assuming the solute diffusion coefficient of $D = 10^{-5}\text{cm}^2\text{s}^{-1}$. The above shows that a wide range of Péclet numbers can be encountered when dissolving fractured and porous rocks, which implies that both mixing rules can commonly occur in nature. For a node i, a general mixing rule would be:

$$c_{ik}^{\text{in}} = (\sum_j \alpha_{jk} q_{ji} c_{ji}^{\text{out}})/(\sum_j \alpha_{jk} q_{ji}) \tag{6.1}$$

where α_{jk} is the fraction of flow from pore ji that makes it to the pore ik. It is noteworthy to point out that if α_{jk} is a constant and independent of j and k, then streamline routing reduces to full mixing rules.

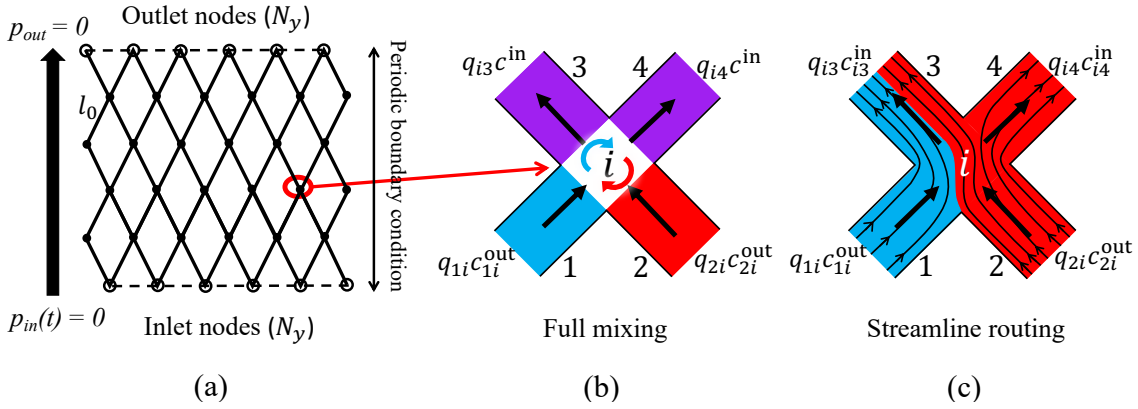

Figure 6.1: (a) A schematic representation of a network with rhombic lattice and line inputs and outputs. (b) Full mixing: Junction i is fed by two solute fluxes with concentrations c_{1i}^{out} and c_{2i}^{out} from pore outlets 1 and 2 respectively. After full mixing, a final concentration c^{in} flows into pores 3 and 4. The colour indicates different concentrations. (c) Streamline routing: Reactant fluxes follow the streamlines. The concentrations entering pores 3 and 4 from node i are c_{i3}^{in} and c_{i4}^{in} respectively.

In the case of a diamond lattice, fraction α_{jk} can be calculated by considering a pore junction i. The incoming concentrations (c_{1i}^{out}) from pore-1 outlet to node i are shown in blue while from pore-2 is marked in red. Pore-2 is assumed to have a larger volumetric flow rate than pore-4 ($q_{2i} > q_{i4}$). With a longer residence time limit (corresponding to full mixing conditions (Fig. 6.1b), these probabilities are $\alpha_{13} = \alpha_{14} = \alpha_{23} = \alpha_{24} = 1$ and the final concentration c^{in} is shown in violet. In the case of streamline routing (Fig. 6.1c), due to larger flow in pore-2, pore-3 will get reactant fluxes from both pore-1 and a fraction of pore-2. The remaining flux is forwarded to pore-4. The corresponding reactant transfer probabilities are $\alpha_{13} = 1, \alpha_{14} = 0, \alpha_{23} = (q_{2i} - q_{i4})/q_{2i}, \alpha_{24} = q_{i4}/q_{2i}$. Using these probabilities in Eq. (6.1), the outgoing concentrations are following:

$$c_{i3}^{\text{in}} = \frac{q_{1i}c_{1i}^{\text{out}} + (q_{2i} - q_{i4})c_{2i}^{\text{out}}}{q_{i3}} \tag{6.2}$$

$$c_{i4}^{in} = c_{2i}^{\text{out}} \tag{6.3}$$

In the case of the reverse situation, that is $q_{i4} > q_{2i}$ (or $q_{i3} < q_{1i}$), the transfer

probabilities can be calculated similarly by performing an appropriate permutation of indices in above expression [61, 62]. In another situation, when there is a node with one inlet pore and three outlet pores or vice versa, the streamline routing rules reduce to full mixing rules; therefore, Eq. (3.24) can be used.

6.4 Results and Discussions

To investigate the effects of pore intersection mixing on the network scale dissolution patterns, we have performed a large number of simulations on a network made of 200×200 nodes, using both full mixing rules (3.24) and streamline routing rules (6.1). Simulations are carried out for a range of Damköhler numbers ($0.01 < \mathrm{Da}_{\mathrm{eff}} < 1.0$). The reason for selecting $\mathrm{Da}_{\mathrm{eff}}$ within this range is that outside this range, dissolution is either uniform (small $\mathrm{Da}_{\mathrm{eff}}$) due to large penetration length or leads to face dissolution (large $\mathrm{Da}_{\mathrm{eff}}$) resulting from small penetration length.

One other parameter of consideration is system heterogeneity. Based on hydraulic variance, three categories of networks are generated: homogeneous ($\sigma^2 = 0.002$), moderate heterogeneous ($\sigma^2 = 0.16$) and strongly heterogeneous ($\sigma^2 = 11$). The results of dissolution simulations conducted with different $\mathrm{Da}_{\mathrm{eff}}$ on different heterogeneous networks are shown in Fig. 6.2. All simulations have a stopping criterion at half breakthrough time, which is defined as when any pore at location $x = L_x/2$ grows five times its initial diameter, with L_x standing for the domain size in the mean flow direction, x. In a uniform dissolution regime, that is, $\mathrm{Da}_{\mathrm{eff}} \leq 0.02$, it is observed that there is no significant difference in the dissolution patterns formed with different mixing rules. Due to the large penetration length, the reactant invades the whole network and results in the same concentrations arriving at the pore intersections from different channels. Referring to Fig. 6.1b-c, if the incoming concentrations ($c_{1i}^{\mathrm{out}} \approx c_{2i}^{\mathrm{out}}$) are the same at any pore intersection, the outgoing concentrations ($c_{i3}^{\mathrm{in}} = c_{i4}^{\mathrm{in}} = c_{1i}^{\mathrm{out}}$) are also same and therefore streamline routing behaves similar to full mixing resulting in similar patterns. However, with increasing $\mathrm{Da}_{\mathrm{eff}}$, the penetration length l_p decreases, which results in more localized dissolution. The reactant is consumed more rapidly locally by the competing flow paths, resulting in faster growth of dominant channels that further localize the dissolution to a few selected dissolution paths. Within this $\mathrm{Da}_{\mathrm{eff}}$ range ($0.05 < \mathrm{Da}_{\mathrm{eff}} < 0.1$), streamline routing yields thinner channels in comparison to channels produced by full mixing rules.

To understand this effect, let us first comment on the impact of mixing protocol on the value of transverse dispersion in the network. In case of fully homogeneous network ($\sigma^2 = 0$), the reactant transfer probabilities α_{jk} at pore junctions (Fig. 3.3(c)) reduces to $\alpha_{13} = 1, \alpha_{14} = 0, \alpha_{23} = 0, \alpha_{24} = 1$. The reactant concentration in pore-1 is transferred to pore-3 and the concentration in pore-2 is forwarded to pore-4, resulting in the movement of concentration in the mean flow direction without any transverse dispersion. On the other hand, in the case of full mixing, the transfer probabilities at any junctions are ($\alpha_{jk} = 1/2$) which results in a uniform distribution of the concentrations in outgoing pores, regardless of the flow. This gives rise to a Saffman-type dispersion [207] in a fully homogeneous network ($\sigma^2 = 0$) for which

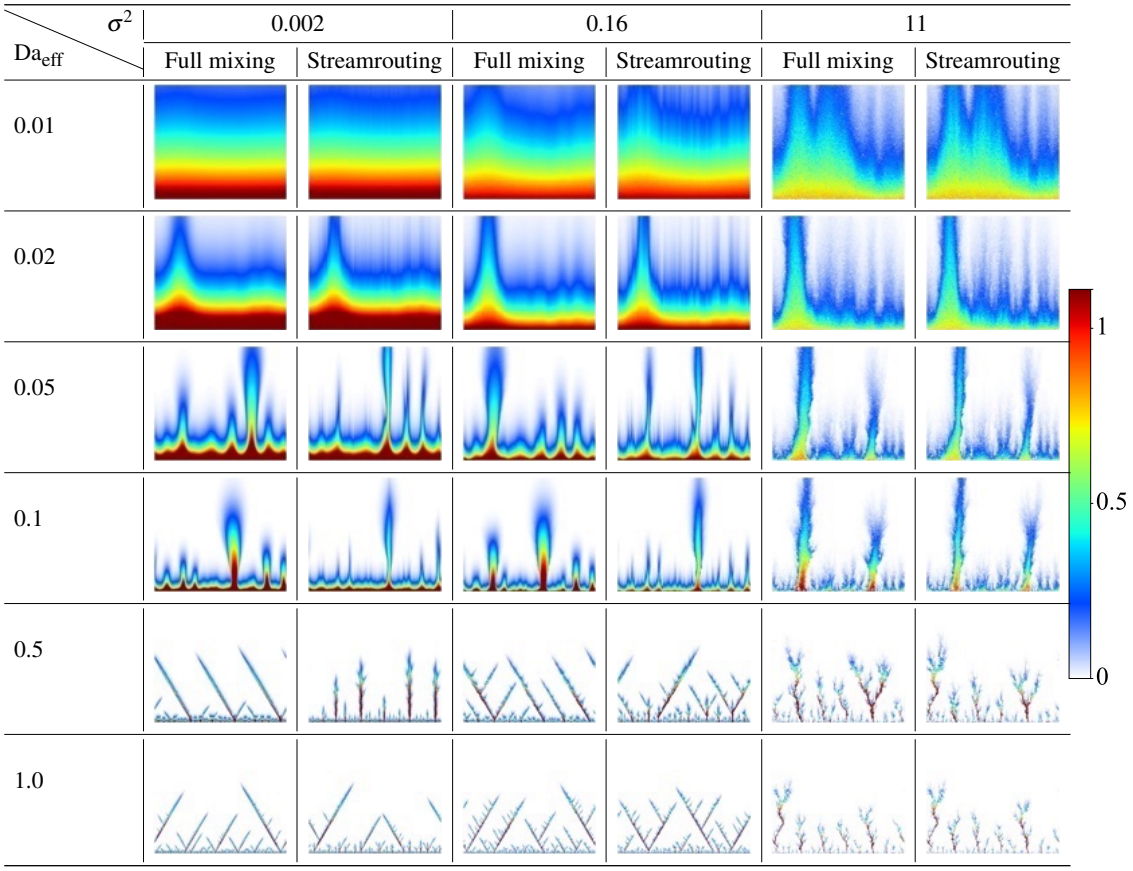

Figure 6.2: Dissolution patterns for different mixing rules as a function of effective Damköhler number (Da_{eff}) and initial heterogeneity of the network. Initial pore diameters are distributed log-normally, and σ^2 is the log-variance of initial hydraulic conductance values. The colours represent the growth of pore diameters ($d_{ij}(t) - d_{ij}(0)$). To better visualize the dissolution patterns, we increased the widths of the lines with which we plot individual pores to three times the diameter of each pore ($3d_{ij}$). The successive shadings indicate large chemical erosion (dark red), intermediate erosion (yellow and green), low erosion (blue), and no erosion (white).

the transverse dispersion coefficient can be calculated by considering a small section of the network (Fig. 6.3).

In full mixing condition, the solute particles can go to either of the outgoing pores with equal transfer probabilities (1/2). The mean square displacement of solute particles in the transverse direction is:

$$\langle X_i^2 \rangle = (l_0 \sin(\pi/4))^2 = l_0^2/2$$

After n time-steps where each step is of size Δt, the dispersion coefficient can be calculated by:

$$2D_T^{\mathrm{fm}} n\Delta t = nl_0^2/2$$

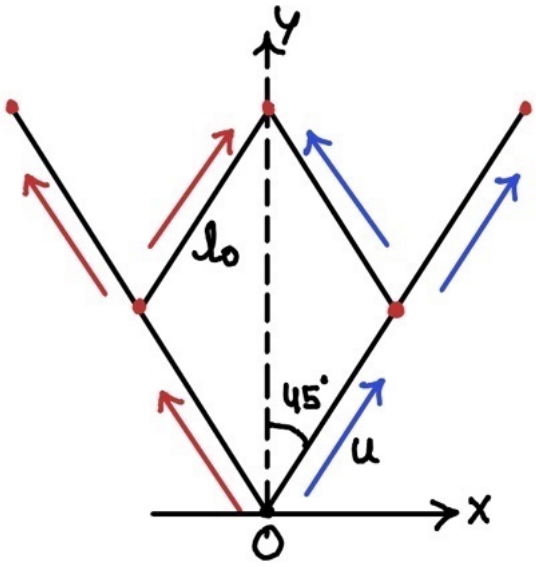

Figure 6.3: A small section of diamond lattice where the solute particles are injected at a node at origin. In full mixing conditions, the solute particle has equal probabilities (1/2) to go out of a node in either of the outgoing pores.

Now replacing, $\Delta t = l_0/u$ gives the dispersion coefficient, $D_T^{\text{fm}} = ul_0/4$ where u is the mean flow rate in the pore.

For streamline routing in a homogeneous network transverse dispersion coefficient vanishes ($D_T^{\text{st}} = 0$), which reflects the fact that the concentration is s simply transmitted from pore to pore, without spreading. Naturally, for a heterogeneous network D_T^{st} will have a finite value, but the magnitude of it is still expected to be considerably smaller than the corresponding value of D_T^{fm}. Another observation, as argued by Steefel and Lasaga [208], is that the width of the dissolution channel is proportional to the square root of dispersion coefficient, $\sqrt{D_T}$ which means that full mixing should produce wider channels in comparison to streamline routing, which is indeed observed. However, as system heterogeneity increases, many of the transfer coefficients α_{jk} become non-zero, and there is an appreciable redistribution of the reactant between the outgoing pores for both mixing protocols [62]. Thus we expect that the differences in channel width produced by different mixing rules decrease with increasing heterogeneity. In the case of moderate and large $\text{Da}_{\text{eff}} \geq 0.5$, the reactant penetration length l_p becomes comparable to the pore length resulting in stronger competition between pores for available reactant concentration. The dominant pores with larger flow rates receive more reactant and exhibit faster growth. In a strongly heterogeneous system ($\sigma^2 = 11$), this leads to the formation of highly branched dissolution patterns with fractal-like characteristics and the width comparable to that of a single pore. The effect of mixing rules is weaker in this dissolution regime. It can be explained by considering a pore-intersection (Fig. 6.4) at which the tip of the wormhole has arrived. Pore-1, corresponding to the path of the wormhole, has significantly higher flow rate in comparison to the other pores. In this situation, the outlet pores (3 & 4) receive a similar concentration as the leading pore, pore-1,

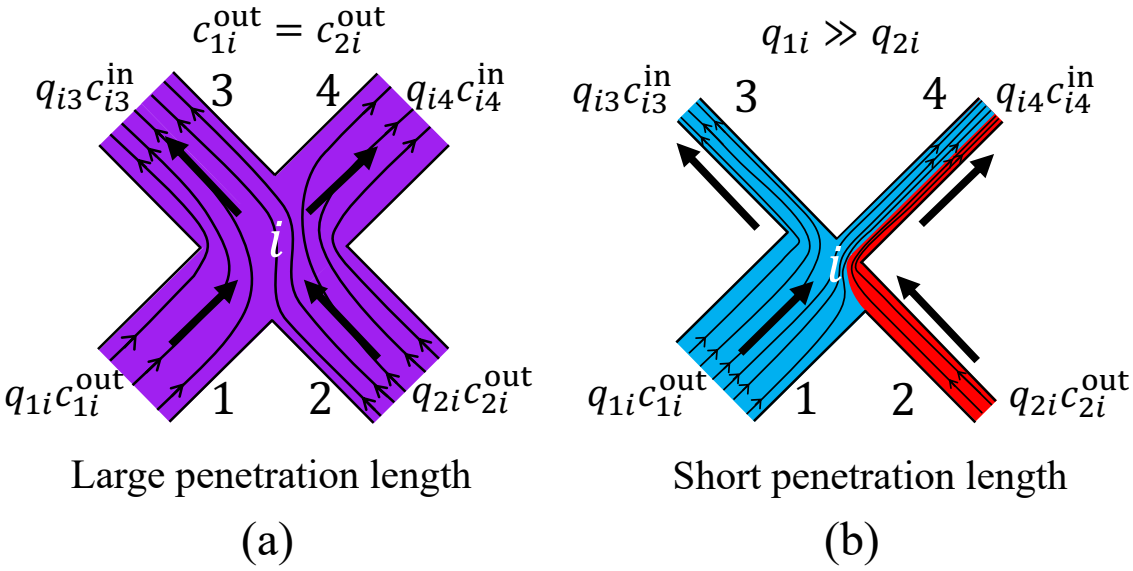

Figure 6.4: Two different scenarios in which streamline routing behaves similar to full mixing (a) Large penetration length (l_p) where concentrations (violet colour) from both pore outlets 1 and 2 are the same ($c_{1i}^{\text{out}} = c_{1i}^{\text{out}}$) and the resulting final concentration ($c_{i3}^{\text{in}} = c_{i4}^{\text{in}} = c_{2i}^{\text{out}}$) enters in pore 3 and 4 (b) Small penetration length with pore 1 having larger flow rate ($q_{1i} \gg q_{2i}$). The respective concentration c_{1i}^{out} (blue colour) dominates the junction and is forwarded to both pores 3 and 4.

reducing the effect of streamline routing. The resulting patterns from both mixing rules are very much the same.

In this dissolution regime ($\text{Da}_{\text{eff}} \geq 0.5$), with smaller heterogeneity ($\sigma^2 = 0.002$), regular Y-shaped patterns are observed with two dominant branches extending along the lattice directions with a characteristic angle of $\pm 45°$ from the mean flow direction. For full mixing case, as shown by Budek and Szymczak [66], once such a configuration forms, it continues to grow since the reactant flux in the pores parallel to the arms will always be larger than that in differently oriented pores around the channel tip. On the other hand, in the case of streamline routing, the formation of Y-shaped patterns is delayed to larger Da_{eff} because streamline routing more strongly focuses reactant in the flow direction. Such a focusing effect intensifies with a decrease in network heterogeneity. This is evidenced, for example, by formed patterns in a small heterogeneity case ($\sigma^2 = 0.002$) with Damköhler number $\text{Da}_{\text{eff}} = 0.5$, in which straight fingers form with characteristics splitting near the tip where the side-branches, angled at $\pm 45°$, briefly appear and grow before dying off. At an even higher Damköhler number ($\text{Da}_{\text{eff}} = 1.0$), the two patterns (straight and angled) coexist, with small straight fingers forming near the inlet, only to give way to Y-shaped channels, which emerge from their side branches. This is because a very short penetration length diminishes the effect of mixing by increasing the network heterogeneity near the dissolution front.

For the quantitative study of the effect of mixing rules over the width of dissolution patterns, we introduce the total width (W) of patterns—defined as the sum of the

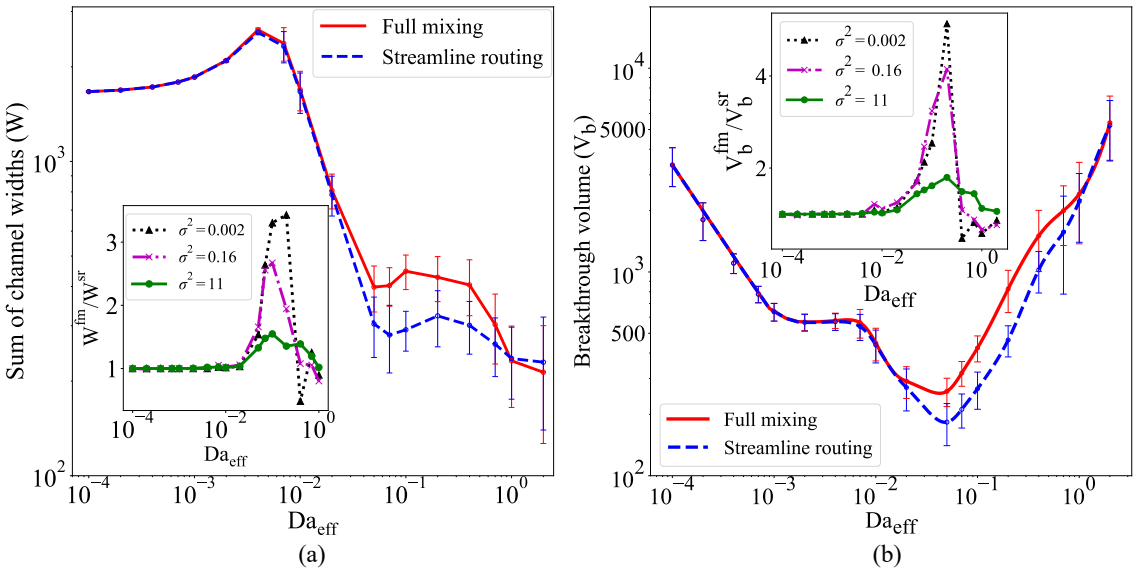

Figure 6.5: (a) The width of the pattern (W) vs effective Damköhler number $\mathrm{Da_{eff}}$ for a network of 200x200 nodes with the transport parameter $G = 1$ and heterogeneity $\sigma^2 = 11$. The simulations were run with full mixing (red line) and streamline routing (blue dashed line). The points present averages over ten realizations of the initial disorder in the network, along with the respective error bars. In the inset, the ratio of the total pattern widths with full mixing and streamline routing, $(W^{\mathrm{fm}}/W^{\mathrm{sr}})$, is plotted vs $\mathrm{Da_{eff}}$ for different heterogeneities ($\sigma^2 = 0.002, 0.16, 11$). (b) Breakthrough volume (V_b) dependence on the Damköhler number for 200x200 network with the transport parameter $G = 1$ and heterogeneity $\sigma^2 = 11$ for both full mixing (red line) and streamline routing (blue dashed line). The points represent averages over ten simulations, along with the respective error bars. In the inset, the ratio of full mixing breakthrough volume to streamline routing volume ($V_b^{\mathrm{fm}}/V_b^{\mathrm{sr}}$) is shown for different heterogeneities.

growth of pore diameters ($\sum \Delta d_i$) where d_i is the diameter of the pores intersecting the mid-line—along the line ($x = L_x/2$). Variation of channel width (W) with different $\mathrm{Da_{eff}}$ is shown in Fig. 6.5. It is evident that for both small and large $\mathrm{Da_{eff}}$ the values of W are insensitive to the mixing rules. However, in the intermediate regime $10^{-2} < \mathrm{Da_{eff}} < 1$ the effect of streamline routing is most pronounced and therefore the channels are the thinnest. The inset of Fig. 6.5 depicts the ratio of channel widths, formed using two mixing rules $W_{\mathrm{fm}}/W_{\mathrm{st}}$, for different network heterogeneities (σ^2). It shows that in the least heterogeneous systems ($\sigma^2 = 0.002$), the effect of mixing rules is maximised at the intermediate values of $\mathrm{Da_{eff}}$, diminishing with an increase in network heterogeneity.

We also investigate the effect of both mixing protocols on the total volume of reactive fluid, V_b, that must be injected into the pores to obtain the breakthrough of the dissolution front. The breakthrough criteria is defined here as the moment when at least one pore at the outlet broadens five times of its initial value. Note that, the breakthrough criteria is set here at the outlet contrary to the Fig. 6.2 where it was

set at $x = L_x/2$. The dependence of V_b on $\mathrm{Da}_{\mathrm{eff}}$ holds a particular significance in the optimisation of dissolution of carbonate reservoirs in which the permeability of reservoirs needs to be increased with the least reactant expense [38, 43, 44, 89, 90].

Fig. 6.5b shows the variation of breakthrough volume, V_b, with $\mathrm{Da}_{\mathrm{eff}}$ for both types of mixing rules in a highly heterogeneous system ($\sigma^2 = 11$). V_b increases for both low ($\mathrm{Da}_{\mathrm{eff}} < 10^{-2}$) and high ($\mathrm{Da}_{\mathrm{eff}} > 1$) Damköhler numbers, with similar values observed for both types of mixing protocols. In these regimes, dissolution is far from optimal in terms of the required volume of reactant to open up the system. In a low Damköhler number regime, the penetration length is larger than the system size resulting in a uniform dissolution throughout the system. In such a case, a lot of reactant is needed to dissolve all the available pore surfaces. On the other hand, for large $\mathrm{Da}_{\mathrm{eff}}$, face dissolution takes place. All the reactant is consumed at the inlet face of the sample, which results in very long dissolution times, and therefore larger breakthrough volume. However, in the moderate $\mathrm{Da}_{\mathrm{eff}}$ number regime, strong competition for reactant among growing pores leads to the formation of dominant channels, which are very effective conduits for the reactant. In this regime, we observed that the streamline routing not only produces thinner wormholes but also minimizes the breakthrough reactant volume. This effect of minimisation is stronger in a nearly homogeneous system ($\sigma^2 = 0.002$), as shown in the inset of Fig. 6.5(a), where the required breakthrough volume can be as much as five times smaller than that in the full mixing case. As the heterogeneity of the system increases, this effect of mixing protocols diminishes but even for the most heterogeneous system ($\sigma^2 = 11$) there can still be a factor of two difference between the breakthrough volumes (inset of Fig. 6.5a).

Lastly, we have also investigated the effect heterogeneity of the system over the breakthrough volume as shown in Fig. 6.6. The Damköhler number used here ($\mathrm{Da}_{\mathrm{eff}} = 0.1$) corresponds to the optimum $\mathrm{Da}_{\mathrm{eff}}$ for the fastest breakthrough in the system. As discussed above, streamline routing requires less reactant volume to achieve breakthrough. This effect is the strongest for the least inhomogeneous case, and then diminishes with heterogeneity, in accordance to our previous observations on the impact of heterogeneity on the mixing effect on dissolution.

6.5 Conclusions

Dissolution of porous medium by an infiltrating reactive fluid is a prime example of a process where pore scales couple to the core- or even reservoir scales. This coupling is particularly pronounced in the unstable regime, which is characterized by the emergence of dissolution channels. This work shows that shapes and propagation velocities of these channels are sensitive to the details of mixing process at pore intersections. When the reactant follows the streamlines, with no time to mix diffusively at the intersections, the flow focusing at the tips of the channels is significantly enhanced and they propagate faster, thus decreasing the breakthrough time. These effects are the strongest in the intermediate Damköhler number regime, where the reactive and advective timescales are similar. Both for larger and smaller Damköhler number the effect of mixing on the dissolution patterns becomes weaker,

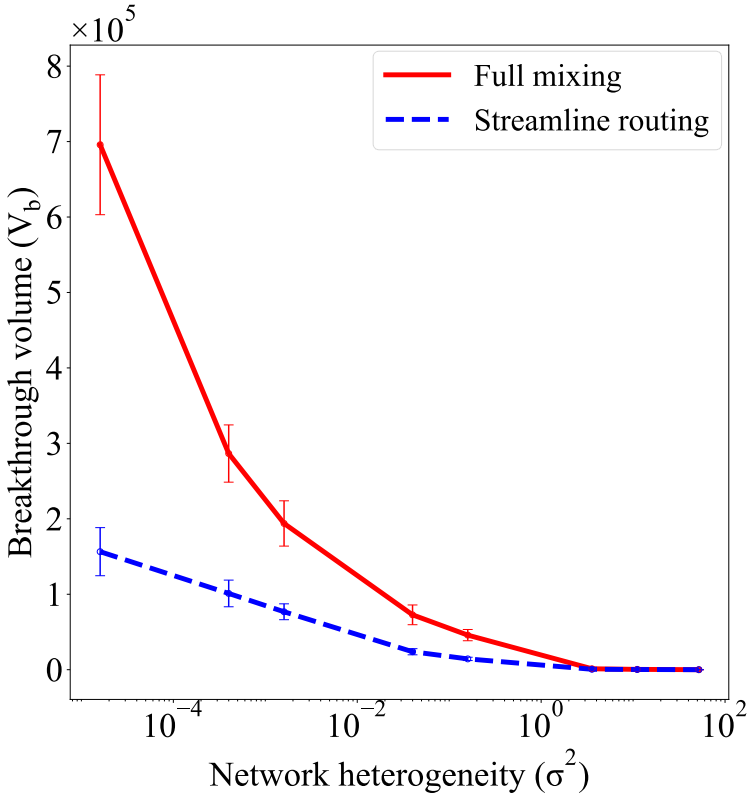

Figure 6.6: Dependence of breakthrough volume (V_b) on system heterogeneity—log-variance of hydraulic conductance (σ^2)—for a network of 200x200 nodes at $Da_{eff} = 0.1$ with transport parameter $G = 1$ for both mixing rules: the blue dashed line represents streamline routing, while the red solid line corresponds to full mixing. The points represent average over ten realization of initial disorder of the network, along with the respective error bars.

but for different reasons. At small Da_{eff}, the concentration of reactant becomes uniform throughout the sample and the mixing rules become irrelevant. At large Da_{eff}, on the other hand, the wormhole tip focuses a very large flow and reactant concentration, so the presence of other incoming pores no longer matters. This is because the disparity of flow and concentration between the pore at wormhole tip and others results in an increase of network heterogeneity at dissolution front. This increase, combined with the short penetration length diminishes the mixing effect. Additionally, the coupling of mixing rules and the large-scale dissolution patterns is suppressed as the initial heterogeneity of the pore space increases.

Chapter 7

Summary

Therefore, I conclude. Therefore, I assume it complete. ...But is it a conclusion, or merely an illusion?...

The present thesis has investigated the dissolution of porous rocks and resulting patterns through a combination of experimental (image-analysis), numerical, and theoretical approaches, mainly focusing on the coupling between micro-scale processes and macro-scale evolution. A key theme of the thesis is micro-macro interplay, where micro-scale dissolution mechanisms such as mixing at pore intersections and pore geometry evolution influence the macro-scale properties such as permeability and porosity, and the shape of dissolution patterns. This thesis integrates both static (pre-post dissolution) and dynamics (during dissolution) perspectives, analyzing dissolution patterns in both naturally karstified and experimentally altered environments. To systematically categorize the findings of this thesis, the research work is described using Table 7.1. The categorization is done based on scale—micro vs. macro, differentiating between micro-scale dissolution mechanisms and their large-scale consequences, as well as on-time dependence, i.e., static vs. dynamic systems, distinguishing structural analysis from the study of time-dependent evolution.

This framework highlights how static characterizations (such as micro and macro structural analysis using tomography imaging) complement dynamic investigations (such as time-lapse tomography analysis of evolving wormhole and network modelling simulation) to provide a comprehensive picture of dissolution-driven evolution in porous media.

Achievements

The key achievements of the thesis are the following:

- We have developed a quantitative framework to analyze pore merging, connectivity evolution, and thickness distribution using X-ray microtomography.

State	Scale	
	Micro	**Macro**
Static	• X-ray microtomography revealed dissolution-induced changes in pore geometry (Ch. 4) • Thickness distribution and connectivity analysis indicates pore-merging (Ch. 4) • Flinn diagram quantified merging of different pore geometries (Ch. 4)	• 4D tomography captured large-scale rock structures before dissolution (Ch. 5) • Packed layers of low permeability act as a barrier, resulting dissolution patterns are tortuous and have more branches (Ch. 5) • Wormholes formed in the layer of higher permeability, are relatively less tortuous and contain fewer branches (Ch. 5) • Tortuosity of wormholes is a characteristic of rock (Ch. 5) • Dissolution-induced changes in pore geometry decreased flow tortuosity (Ch. 4)
Dynamic	• Network scale dissolution modeling shows how inhomogeneous dissolution develops over time (Ch. 6) • Wormhole growth dynamics depends on pore intersection mixing rules (Ch. 6) • Full mixing rules lead to higher dispersion of solute particles at pore intersections, compared to streamline routing (Ch. 6) • In natural dissolution, pore geometries evolve by enlargening as well as merging of pores (Ch. 4) • Strong flow focusing in largest pores also accounts for changes in pore-geometries (Ch. 4)	• Time-lapse (4D) tomography tracked real-time wormhole propagation (Ch. 5) • Tip evolution of wormhole showed speed-ups and lateral turns. (Ch. 5) • Permeability evolution is correlated with tip evolution, showing larger drops and plateaus (Ch. 5) • Evolution of wormhole geometry is quantified by geometric characteristics (Ch. 5) • Streamline routing resulted in thinner channels that move faster, leading to a faster breakthrough in comparison to the channels formed by full mixing rules (Ch. 6)

Table 7.1: Categorization of thesis contributions based on micro-macro coupling and static-dynamic aspects.

- We have also used, Flinn diagrams, to quantify the type of merging geometries (i.e. oblate and prolate shapes) and their impact on the thickness evolution in

the merging process.

- We have demonstrated that inhomogeneous dissolution plays a significant role in karstification where pore space evolves through different mechanisms: uniform dissolution of individual pores, merging of pores, and emergence of preferential flow paths.
- We have developed a novel segmentation method, volume-based segmentation, to analyze time-lapse 4D microtomography images.
- We have also proposed geometric characteristics to quantify the differences in the shape of different wormholes formed in two types of rock.
- We have shown that large-scale structures such as cemented regions (packed layers) act as flow barriers, influencing not only the growth dynamics but also the overall shape of a wormhole.
- Using time-lapse experiments, we demonstrated that wormhole while evolving through packed layers, shows speed-ups and lateral turns, which correspond to non-linear permeability evolution (dispersed in plateaus and large drops).
- Using a network modeling approach, we have established that pore-scale processes (such as pore-intersection mixing) not only influence the shape large-scale dissolution patterns but also their growth velocities.

These findings improve our understanding of dissolution processes in porous media by elucidating the fundamental physics behind reactive flow instabilities, pore-scale transport phenomena, and the formation of self-organized dissolution patterns, which enhances predictive capabilities in this key area of reactive transport. The insights gained into porous media dissolution, particularly in terms of micro-macro coupling, could help refine reactive-transport models and address various transport physics challenges. The deeper understanding of wormholing—especially the role of system heterogeneity, such as macro-scale rock microfacies—has direct implications for geology and petroleum engineering. However, its relevance extends beyond these fields, as wormhole-like, fractal channels also form in other unstable growth systems. The results of this thesis will also be valuable for applications such as geological carbon storage, groundwater remediation, karst formation studies, or any area where predicting and controlling dissolution-driven processes is crucial. Additionally, the methods developed for extracting and analyzing dissolution pattern shapes have significant potential for pattern formation studies. Techniques like volume-based segmentation and tools for analyzing pore geometry from tomography images, initially designed for reactive transport studies, could benefit a wider range of research communities

Bibliography

[1] Snowcrystal.com. A stellar-plate type snowflake. URL https://www.snowcrystals.com/photos/photos.html.

[2] M. Hofmann, R. Anderssohn, H. Bahr, H. Weiß, and J. Nellesen. Why hexagonal basalt columns? *Phys. Rev. Lett.*, 115(15):154301, 2015.

[3] P. Meakin and B. Jamtveit. Geological pattern formation by growth and dissolution in aqueous systems. *Proc. Roy. Soc. A-Math Phy.*, 466(2115):659–694, 2010.

[4] NASA/JPL-Caltech. An infrared view of the m81 galaxy, 2019. URL https://science.nasa.gov/resource/an-infrared-view-of-the-m81-galaxy/.

[5] A. M. Turing. The chemical basis of morphogenesis. *Philos. Trans. R. Soc. Lond. B. Biol. Sci.*, 237(641):37–72, 1952.

[6] D. W. Thompson. *On growth and form*. Cambridge University Press, 1942.

[7] NASA/Goddard. Large-scale fractal motion of clouds, 1999. URL https://earthobservatory.nasa.gov/images/625/.

[8] T. Von Kármán. *Aerodynamics*. McGraw-Hill paperbacks : Science, mathematics and engineering. McGraw-Hill, 1963.

[9] Rayleigh. Investigation of the character of the equilibrium of an incompressible heavy fluid of variable density. *Proc. Lond. Math. Soc.*, s1-14(1):170–177, 1882.

[10] G. I. Taylor. The instability of liquid surfaces when accelerated in a direction perpendicular to their planes. *Proc. Roy. Soc. A-Math Phy.*, 201(1065):192–196, 1950.

[11] D. H. Clark and F. R. Stephenson. *The Historical Supernovae*. Pegamon Press, 1977.

[12] J. J. Hester, J. M. Stone, P. A. Scowen, B. Jun II, J. S. Gallagher III, M. L. Norman, et al. WFPC2 studies of the Crab nebula. III. magnetic Rayleigh-Taylor instabilities and the origin of the filaments. *Astrophys. J.*, 456:225, 1996.

[13] O. Porth, S. S. Komissarov, and R. Keppens. Rayleigh–Taylor instability in magnetohydrodynamic simulations of the Crab nebula. *Mon. Not. Roy. Astron Soc.*, 443(1):547–558, 2014.

[14] M. Mohammadi, M. Khalifi, N. Sabet, and H. Hassanzadeh. Experiments and reduced order modeling of symmetry breaking in Rayleigh-Taylor mixing. *Phys. Rev. Fluids*, 8(10):103504, 2023.

[15] P. G. Saffman and G. Taylor. The penetration of a fluid into a porous medium or Hele-Shaw cell containing a more viscous liquid. *Proc. R. Soc. A-Math Phy.*, 245(1242):312–329, 1958.

[16] J. D. Chen. Growth of radial viscous fingers in a Hele-Shaw cell. *J. Fluid Mech.*, 201(1):223, 1989.

[17] O. Zik and E. Moses. Fingering instability in combustion: An extended view. *Phys. Rev. E*, 60(1):518–531, 1999.

[18] E. Ben-Jacob. From snowflake formation to growth of bacterial colonies II: Cooperative formation of complex colonial patterns. *Contemp. Phys.*, 38(3): 205–241, 1997.

[19] S. de Villiers, A. Nermoen, B. Jamtveit, J. Mathiesen, P. Meakin, and S. C. Werner. Formation of Martian araneiforms by gas-driven erosion of granular material. *Geophys. Res. Lett.*, 39(13):L13204, 2012.

[20] H. J. Seybold, E. Kite, and J. W. Kirchner. Branching geometry of valley networks on Mars and Earth and its implications for early Martian climate. *Sci. Adv.*, 4(6):eaar6692, 2018.

[21] O. Devauchelle, A. P. Petroff, H. F. Seybold, and D. H. Rothman. Ramification of stream networks. *Proc. Natl. Acad. Sci.*, 109(51):20832–20836, 2012.

[22] A. P. Petroff, O. Devauchelle, H. Seybold, and D. H. Rothman. Bifurcation dynamics of natural drainage networks. *Philos. Trans. R. Soc. A: Math. Phys. Eng. Sci.*, 371(2004):20120365, 2013.

[23] M. E. Glicksman. Mechanism of dendritic branching. *Metall. Mater. Trans. A.*, 43(2):391–404, 2011.

[24] B. Chopard, H. J. Herrmann, and T. Vicsek. Structure and growth mechanism of mineral dendrites. *Nature*, 353(6343):409–412, 1991.

[25] Z. Hou, D. Woś, C. Tschegg, A. Rogowitz, A. H. N. Rice, L. Nasdala, F. Fusseis, P. Szymczak, and B. Grasemann. Three-dimensional mineral dendrites reveal a nonclassical crystallization pathway. *Geology*, 51(7):626–630, 2023.

[26] D. Chadam, D. Hoff, E. Merino, P. J. Ortoleva, and A. Sen. Reactive infiltration instabilities. *J. Appl. Math.*, 36:207–221, 1986.

[27] P. J Ortoleva. *Geochemical Self-Organization*. Oxford University PressNew York, NY, 1994.

[28] F. J. Dahlkamp. *Uranium Deposits of the World*. Springer, 2009.

[29] M. Lipar, J. A. Webb, S. Q. White, and K. G Grimes. The genesis of solution pipes: Evidence from the middle—late pleistocene bridgewater formation calcarenite, southeastern Australia. *Geomorphology*, 246:90–103, 2015.

[30] Laotzu. *Tao Te Ching*. 600BC.

[31] A. Catcott. *A Treatise on the Deluge*. 1768.

[32] C. Lyell. *Principles of Geology: being an Attempt to Explain the Former Changes of the Earth's Surface, by Reference to Causes Now in Operation-I*. 1832.

[33] D. Romanov, F. Gabrovšek, and W. Dreybrodt. Dam sites in soluble rocks: a model of increasing leakage by dissolutional widening of fractures beneath a dam. *Eng. Geol.*, 70:129–145, 2003.

[34] J. E. King and L. Paterson. Coupling of geochemical reactions and convective mixing in the long-term geological storage of carbon dioxide. *Int. J. Greenh. Gas Control*, 1:86–93, 2007.

[35] A. E. Fryar and F. W. Schwartz. Hydraulic-conductivity reduction, reaction-front propagation, and preferential flow within a model reactive barrier. *J. Contam. Hydrol.*, 32:333–351, 1998.

[36] M. J. Economides and K. G. Nolte. *Reservoir Stimulation*. John Wiley and Sons, 2000.

[37] M. L. Hoefner and H. S. Fogler. Pore evolution and channel formation during flow and reaction in porous media. *AIChE J.*, 34(1):45–54, 1988.

[38] C. N. Fredd and H. S. Fogler. Influence of transport and reaction on wormhole formation in porous media. *AIChE J.*, 44:1933–1949, 1998.

[39] B. Bazin, C. Roque, and M. Bouteca. A laboratory evaluation of acid propagation in relation to acid fracturing: Results and interpretation. *SPE European Formation Damage Conference, The Hague, Netherlands*, 1995.

[40] D. McDuff, C. E. Shuchart, S. Jackson, D. Postl, J. S. Brown, et al. Understanding wormholes in carbonates: Unprecedented experimental scale and 3D visualization. *J. Pet. Technol.*, pages 78–81, 2010.

[41] M. P. Cooper, R. P. Sharma, S. Magni, T. P. Blach, A. P. Radlinski, K. Drabik, A. Tengattini, and P. Szymczak. 4D tomography reveals a complex relationship between wormhole advancement and permeability variation in dissolving rocks. *Adv. Water Resour.*, 175:104407, 2023.

[42] G. Daccord, E. Touboul, and R. Lenormand. Chemical dissolution of a porous medium: limits of the fractal behaviour. *Geoderma*, 44(2-3):159–165, 1989.

[43] F. Golfier, C. Zarcone, B. Bazin, R. Lenormand, D. Lasseux, and M. Quintard. On the ability of a Darcy-scale model to capture wormhole formation during the dissolution of a porous medium. *J. Fluid Mech.*, 457:213–254, 2002.

[44] C. E. Cohen, D. Ding, M. Quintard, and B. Bazin. From pore scale to well-bore scale: Impact of geometry on wormhole growth in carbonate acidization. *Chem. Eng. Sci.*, 63(12):3088–3099, 2008.

[45] G. Daccord. Chemical dissolution of a porous medium by a reactive fluid. *Phys. Rev. Lett.*, 58(5):479–482, 1987.

[46] G. Daccord and R. Lenormand. Fractal patterns from chemical dissolution. *Nature*, 325:41–43, 1987.

[47] B. Bazin, M. T. Bieber, C. Roque, and M. Bouteca. Improvement in the characterization of the acid wormholing by in-situ X-ray CT visualizations. *SPE Formation Damage Control Symposium, Lafayette, Louisiana*, 1996.

[48] H. Ott and S. Oedai. Wormhole formation and compact dissolution in single- and two-phase CO2-brine injections. *Geophys. Res. Lett.*, 42:2270–2276, 2015.

[49] Y. Al-Khulaifi, Q. Lin, M. J. Blunt, and B. Bijeljic. Pore-scale dissolution by CO2 saturated brine in a multimineral carbonate at reservoir conditions: Impact of physical and chemical heterogeneity. *Water Resour. Res.*, 55(4): 3171–3193, 2019.

[50] H. P. Menke, C. A. Reynolds, M. G. Andrew, J. P. Pereira Nunes, B. Bijeljic, and M. J. Blunt. 4D multi-scale imaging of reactive flow in carbonates: Assessing the impact of heterogeneity on dissolution regimes using streamlines at multiple length scales. *Chem. Geol.*, 481:27–37, 2018.

[51] J. Snippe, S. Berg, K. Ganga, N. Brussee, and R. Gdanski. Experimental and numerical investigation of wormholing during CO2 storage and water alternating gas injection. *Int. J. Greenh. Gas Control.*, 94:102901, 2020.

[52] W. Li, H. H. Einstein, and J. T. Germaine. An experimental study of matrix dissolution and wormhole formation using gypsum core flood tests: 1. Permeability evolution and wormhole geometry analysis. *J. Geophys. Res. Solid Earth.*, 124(11):11055–11073, 2019.

[53] H. P. Menke, M. G. Andrew, M. J. Blunt, and B. Bijeljic. Reservoir condition imaging of reactive transport in heterogeneous carbonates using fast synchrotron tomography—Effect of initial pore structure and flow conditions. *Chem. Geol.*, 428:15–26, 2016.

[54] V. K. Upadhyay, P. Szymczak, and A. J. C. Ladd. Initial conditions or emergence: What determines dissolution patterns in rough fractures? *J. Geophys. Res. Solid Earth*, 120(9):6102–6121, 2015.

[55] L. Li, C. A. Peters, and M. A. Celia. Effects of mineral spatial distribution on reaction rates in porous media. *Water Resour. Res.*, 43(1):W01419, 2007.

[56] R. Roded, P. Szymczak, and R. Holtzman. Wormholing in anisotropic media: Pore-scale effect on large-scale patterns. *Geophys. Res. Lett.*, 48(11): e2021GL093659, 2021.

[57] L. Li, C. A. Peters, and M. A. Celia. Upscaling geochemical reaction rates using pore-scale network modeling. *Adv. Water Res.*, 29(9):1351–1370, 2006.

[58] H. Deng, S. Molins, D. Trebotich, C. Steefel, and D. DePaolo. Pore-scale nu-

merical investigation of the impacts of surface roughness: Upscaling of reaction rates in rough fractures. *Geochim. Cosmochim. Acta*, 239:374–389, 2018.

[59] M. Liu, B. Kwon, and P. K Kang. Machine learning to predict effective reaction rates in 3D porous media from pore structural features. *Sci. Rep*, 12:5486, 2022.

[60] W. Lee, S. Yoon, and P. K Kang. Inertia and diffusion effects on reactive transport with fluid-solid reactions in rough fracture flows. *Phys. Rev. Fluids*, 8(5):054502, 2023.

[61] Y. J. Park, K. K. Lee, and B. Berkowitz. Effects of junction transfer characteristics on transport in fracture networks. *Water Resour. Res.*, 37(4):909–923, 2001.

[62] P. K. Kang, M. Dentz, T. Le Borgne, and R. Juanes. Anomalous transport on regular fracture networks: Impact of conductivity heterogeneity and mixing at fracture intersections. *Phys. Rev. E*, 92(2):022148, 2015.

[63] T. Sherman, J. D. Hyman, D. Bolster, N. Makedonska, and G. Srinivasan. Characterizing the impact of particle behavior at fracture intersections in three-dimensional discrete fracture networks. *Phys. Rev. E*, 99(1):013110, 2019.

[64] S. H. Lee and P. K. Kang. Three-dimensional vortex-induced reaction hot spots at flow intersections. *Phys. Rev. Lett.*, 124(14):144501, 2020.

[65] L. Zou, L. Jing, and V. Cvetkovic. Modeling of flow and mixing in 3D rough-walled rock fracture intersections. *Adv. Water Res.*, 107:1–9, 2017.

[66] A. Budek and P. Szymczak. Network models of dissolution of porous media. *Phys. Rev. E*, 86(5):056318, 2012.

[67] M. G. Rios, L. Luquot, J. M. Soler, and J. Cama. Influence of the flow rate on dissolution and precipitation features during percolation of CO2-rich sulfate solutions through fractured limestone samples. *Chem. Geol.*, 414:95–108, 2015.

[68] L. Luquot, O. Rodriguez, and P. Gouze. Experimental characterization of porosity structure and transport property changes in limestone undergoing different dissolution regimes. *Transp. Porous Media*, 101(3):507–532, 2014.

[69] C. Noiriel, P. Gouze, and B. Made. 3D analysis of geometry and flow changes in a limestone fracture during dissolution. *J. Hydrol.*, 486:211–223, 2013.

[70] J. Qajar and C. H. Arns. Chemically induced evolution of morphological and connectivity characteristics of pore space of complex carbonate rock via digital core analysis. *Water Resour. Res.*, 58(3):e2021WR031298, 2022.

[71] J. Qajar and C. H. Arns. A comparative study of micro-CT and mercury intrusion techniques for predicting permeability and surface area evolution during chemical dissolution. *Adv. Water Resour.*, 168:104301, 2022.

[72] P. V. Cappellen. Reactive surface area control of the dissolution kinetics of biogenic silica in deep-sea sediments. *Chem. Geol.*, 132(1–4):125–130, 1996.

[73] J. M. Gautier, E. H. Oelkers, and J. Schott. Are quartz dissolution rates proportional to B.E.T. surface areas? *Geochim. Cosmochim. Acta*, 65(7): 1059–1070, 2001.

[74] C. Noiriel, L. Luquot, B. Madé, L. Raimbault, P. Gouze, and J. V. Lee. Changes in reactive surface area during limestone dissolution: An experimental and modelling study. *Chem. Geol.*, 265:160–170, 2009.

[75] A. J. Luhmann, X. Z. Kong, B. M. Tutolo, N. Garapati, B. C. Bagley, M. O. Saar, and W. E. Seyfried. Experimental dissolution of dolomite by CO2-charged brine at 100° and 150bar: Evolution of porosity, permeability, and reactive surface area. *Chem. Geol.*, 380:145–160, 2014.

[76] R. S. Schechter and J. L. Gidley. The change in pore size distribution from surface reactions in porous media. *AIChE J.*, 15(3):339–350, 1969.

[77] L. Li, C. A. Peters, and M. A. Celia. Effects of mineral spatial distributions on reaction rates in porous media. *Water Resour. Res.*, 43:W01419, 2007.

[78] L. Luquot and P. Gouze. Experimental determination of porosity and permeability changes induced by injection of CO2 into carbonate rocks. *Chem. Geol.*, 265(1-2):148–159, 2009.

[79] S. Molins, D. Trebotich, L. Yang, J. B. Ajo-Franklin, T. J. Ligocki, C. Shen, and C. I. Steefel. Pore-scale controls on calcite dissolution rates from flow-through laboratory and numerical experiments. *Environ. Sci. Technol.*, 48 (13):7453–7460, 2014.

[80] T. Hildebrand and P. Rüegsegger. A new method for the model-independent assessment of thickness in three-dimensional images. *J. Microsc.*, 185(1):67–75, 1997.

[81] R. Dougherty and K. H. Kunzelmann. Computing local thickness of 3D structures with ImageJ. *Microsc. Microanal.*, 13(S02):1678–1679, 2007.

[82] P. Virtanen, R. Gommers, T. E. Oliphant, M. Haberland, T. Reddy, D. Cournapeau, E. Burovski, P. Peterson, W. Weckesser, and J. Bright. Scipy 1.0: fundamental algorithms for scientific computing in Python. *Nat. Methods*, 17 (3):261–272, 2020.

[83] P. Ortoleva, J. Chadam, E. Merino, and A. Sen. Geochemical self-organization II: The reactive-infiltration instability. *Am. J. Sci*, 287:1008–1040, 1987.

[84] F. Osselin, A. Budek, O. Cybulski, P. Kondratiuk, P. Garstecki, and P. Szymczak. Microfluidic observation of the onset of reactive infiltration instability in an analog fracture. *Geophys. Res. Lett.*, 43:6907–6915, 2016.

[85] C. G. Groves and A. D. Howard. Minimum hydrochemical conditions allowing limestone cave development. *Water Resour. Res.*, 30:607–615, 1994.

[86] P. Szymczak and A. J. C. Ladd. Instabilities in the dissolution of a porous matrix. *Geophys. Res. Lett.*, 38:L07403, 2011.

[87] Y. Wang, A. D. Hill, R. S. Schechter, et al. The optimum injection rate for matrix acidizing of carbonate formations. *SPE Annual Technical Conference and Exhibition, Houston, Texas*, 1993.

[88] Y. Huang, G. Ouillon, H. Saleur, and D. Sornette. Spontaneous generation of discrete scale invariance. *Phys. Rev. E*, 55:6433–6447, 1997.

[89] N. Kalia and V. Balakotaiah. Modeling and analysis of wormhole formation in reactive dissolution of carbonate rocks. *Chem. Eng. Sci.*, 62(4):919–928, 2007.

[90] M. Panga, M. Ziauddin, and V. Balakotaiah. Two-scale continuum model for simulation of wormhole formation in carbonate acidization. *AIChE J.*, 51: 3231–3248, 2005.

[91] A. D. Hill, D. Zhu, and Y. Wang. The effect of wormholing on the fluid-loss coefficient in acid fracturing. *SPE Prod. Facil.*, 10(04):257–264, 1995.

[92] O. Izgec, D. Zhu, and A. D. Hill. Numerical and experimental investigation of acid wormholing during acidization of vuggy carbonate rocks. *J. Pet. Sci. Eng.*, 74(1-2):51–66, 2010.

[93] T. P. Frick, B. Mostofizadeh, and M. J. Economides. Analysis of radial core experiments for hydrochloric acid interaction with limestones. *SPE Formation Damage Control Symposium, Lafayette, Louisiana*, 1994.

[94] J. Etten, D. Zhu, and A. D. Hill. The combined effect of permeability and pore structure on carbonate matrix acidizing. *EUROPEC 2015, Madrid, Spain*, 2015.

[95] D. Dubetz, H. Cheng, D. Zhu, and A. D. Hill. Characterization of rock pore-size distribution and its effects on wormhole propagation. *SPE Annual Technical Conference and Exhibition, Dubai, UAE*, 2016.

[96] K. Petrus and P. Szymczak. Influence of layering on the formation and growth of solution pipes. *Front. Phys.*, 3:92, 2016.

[97] M.E. Ziauddin and E Bize. The effect of pore-scale heterogeneities on carbonate stimulation treatments. *SPE Middle East Oil and Gas Show and Conference, Kingdom of Bahrain*, SPE-104627, 2007.

[98] S. Békri, J. F. Thovert, and P. M. Adler. Dissolution of porous media. *Chem. Eng. Sci.*, 50:2765–2791, 1995.

[99] M. A. Buijse. Understanding wormholing mechanisms can improve acid treatments in carbonate formations. *SPE Prod. Facil.*, 8:168, 2000.

[100] P. Szymczak and A. J. C. Ladd. Microscopic simulations of fracture dissolution. *Geophys. Res. Lett.*, 31:L23606, 2004.

[101] C. Soulaine and H. A. Tchelepi. Micro-continuum approach for pore-scale simulation of subsurface processes. *Transp. Porous Med.*, 113(3):431–456, 2016.

[102] J. P. Pereira Nunes, M. J. Blunt, and B. Bijeljic. Pore-scale simulation of carbonate dissolution in micro-CT images. *J. Geophys. Res. Solid*, 121(2): 558–576, 2016.

[103] V. Starchenko, C. J. Marra, and A. J. C. Ladd. Three-dimensional simulations of fracture dissolution. *J. Geophys. Res. Solid*, 121:6421–6444, 2016.

[104] D. Yu and A. J. C. Ladd. A numerical simulation method for dissolution in porous and fractured media. *J. Comput. Phys.*, 229:6450–6465, 2010.

[105] H. Yoon, A. J. Valocchi, C. J. Werth, and T. Dewers. Pore-scale simulation of mixing-induced calcium carbonate precipitation and dissolution in a microfluidic pore network. *Water Resour. Res.*, 48(2), 2012.

[106] Li Chen, Q. Kang, H. S. Viswanathan, and W. Q. Tao. Pore-scale study of dissolution-induced changes in hydrologic properties of rocks with binary minerals. *Water Resour. Res.*, 50(12):9343–9365, 2014.

[107] J. P. Pereira Nunes, M. J. Blunt, and B. Bijeljic. Pore-scale simulation of carbonate dissolution in micro-CT images. *J. Geophys. Res. Solid Earth*, 121 (2):558–576, 2016.

[108] C. Soulaine, S. Roman, A. Kovscek, and H. A. Tchelepi. Mineral dissolution and wormholing from a pore-scale perspective. *J. Fluid Mech.*, 827:457–483, 2017.

[109] S. Molins, C. Soulaine, N. I. Prasianakis, A. Abbasi, P. Poncet, A. J. C. Ladd, et al. Simulation of mineral dissolution at the pore scale with evolving solid-fluid interfaces: Review of approaches and benchmark problem set. *Comput. Geosci.*, 25:1285–1318, 2021.

[110] Z. Wang, M. Hu, and C. Steefel. Pore-scale modeling of reactive transport with coupled mineral dissolution and precipitation. *Water Resour. Res.*, 60 (6):e2023WR036122, 2024.

[111] Q. Kang, P. C. Lichtner, and D. Zhang. Lattice boltzmann pore-scale model for multicomponent reactive transport in porous media. *J. Geophys. Res.*, 111 (B5):B05203, 2006.

[112] V. Starchenko and A. J. C. Ladd. The development of wormholes in laboratory scale fractures: perspectives from three-dimensional simulations. *Water Resour. Res.*, 54(10):7946–7959, 2018.

[113] C. I. Steefel, S. B. Yabusaki, and K. U. Mayer. Reactive transport benchmarks for subsurface environmental simulation. *Comput. Geosci.*, 19(3):439–443, 2015.

[114] P. Lichtner, G. Hammond, C. Lu, S. Karra, G. Bisht, B. Andre, R. Mills, and J. Kumar. PFLOTRAN user manual: A massively parallel reactive flow and transport model for describing surface and subsurface processes. 2015.

[115] J. Bear. *Dynamics of fluids in porous media*. Dover Publications, 1972.

[116] E. de Boever, C. Varloteaux, F. H. Nader, A. Foubert, S. Békri, S. Youssef, and E.ś Rosenberg. Quantification and prediction of the 3D pore network evolution in carbonate reservoir rocks. *Oil Gas Sci. Technol.*, 67(1):161–178, 2012.

[117] C. Varloteaux, M. Tan Vu, S. Békri, and P. M. Adler. Reactive transport in porous media: pore-network model approach compared to pore-scale model. *Phys. Rev. E*, 87(2):023010, 2013.

[118] S. Li, Z. Kang, X. Feng, Z. Pan, X. Huang, and D. Zhang. Three-dimensional hydrochemical model for dissolutional growth of fractures in karst aquifers. *Water Resour. Res.*, 56(3):e2019WR025631, 2020.

[119] A. J. C. Ladd and P. Szymczak. Use and misuse of large-density asymptotics in the reaction-infiltration instability. *Water Resour. Res.*, 53(3):2419–2430, 2017.

[120] A. J. C. Ladd and P. Szymczak. Reactive flows in porous media: Challenges in theoretical and numerical methods. *Annu. Rev. Chem. Biomol. Eng.*, 12: 543–571, 2021.

[121] M. Oostrom, Y. Mehmani, P. Romero-Gomez, Y. Tang, H. Liu, H.u Yoon, Q. Kang, V. Joekar-Niasar, M. T. Balhoff, T. Dewers, et al. Pore-scale and continuum simulations of solute transport micromodel benchmark experiments. *Computat. Geosci.*, 20(4):857–879, 2016.

[122] X. Yang, Y. Mehmani, W. A. Perkins, A. Pasquali, M. Schönherr, K. Kim, M. Perego, M. L. Parks, et al. Intercomparison of 3D pore-scale flow and solute transport simulation methods. *Adv. Water Res.*, 95:176–189, 2016.

[123] M. J. Berger and P. Colella. Local adaptive mesh refinement for shock hydrodynamics. *J. Comput. Phys.*, 82(1):64–84, 1989.

[124] M. Yousefzadeh and I. Battiato. High order ghost-cell immersed boundary method for generalized boundary conditions. *Int. J. Heat Mass Tran.*, 137: 585–598, 2019.

[125] R. Verberg and A. J. C. Ladd. Simulation of chemical erosion in rough fractures. *Phys. Rev. E*, 65:056311, 2002.

[126] Q. J. Kang, D. X. Zhang, and S. Y. Chen. Simulation of dissolution and precipitation in porous media. *J. Geophys. Res.*, 108:B102505, 2003.

[127] W. Aniszewski, T. Ménard, and M. Marek. Volume of fluid (VOF) type advection methods in two-phase flow: A comparative study. *Comput. Fluids.*, 97:52–73, 2014.

[128] X. Zhijie and M. Paul. Phase-field modeling of two-dimensional solute precipitation/dissolu tion: Solid fingers and diffusion-limited precipitation. *J. Chem. Phys.*, 134(4):044137, 2011.

[129] H. Luo, M. Quintard, G. Debenest, and F. Laouafa. Properties of a diffuse

interface model based on a porous medium theory for solid–liquid dissolution problems. *Comput. Geosci.*, 16(4):913–932, 2012.

[130] S. Molins, D. Trebotich, C. I. Steefel, and C. Shen. An investigation of the effect of pore scale flow on average geochemical reaction rates using direct numerical simulation. *Water Resour. Res.*, 48(3), 2012.

[131] B. De Baere, S. Molins, K. U. Mayer, and R. François. Determination of mineral dissolution regimes using flow-through time-resolved analysis (FT-TRA) and numerical simulation. *Chem. Geol.*, 430:1–12, 2016.

[132] F. Dutka, V. Starchenko, F. Osselin, S. Magni, P. Szymczak, and A. J. C. Ladd. Time-dependent shapes of a dissolving mineral grain: comparisons of simulations with microfluidic experiments. *Chem. Geol.*, 540:119459, 2020.

[133] C. I. Steefel and A. C. Lasaga. A coupled model for transport of multiple chemical species and kinetic precipitation/dissolution reactions with application to reactive flow in single phase hydrothermal systems. *Am. J. Sci.*, 294 (5):529–592, 1994.

[134] L. M. Walter and J. W. Morse. Reactive surface area of skeletal carbonates during dissolution: Effect of grain size. *J. Sediment. Res.*, 54(4):1081–1090, 1984.

[135] G. T. Yeh and V. S. Tripathi. A model for simulating transport of reactive multispecies components: Model development and demonstration. *Water Resour. Res.*, 27(12):3075–3094, 1991.

[136] C. I. Steefel, C. A. J. Appelo, B. Arora, D. Jacques, T. Kalbacher, O. Kolditz, V. Lagneau, P. C. Lichtner, et al. Reactive transport codes for subsurface environmental simulation. *Comput. Geosci.*, 19(3):445–478, 2014.

[137] R. Roded, E. Aharonov, R. Holtzman, and P. Szymczak. Reactive flow and homogenization in anisotropic media. *Water Resour. Res.*, 56(12): e2020WR027518, 2020.

[138] R. P. Sharma, J. Deng, P. K. Kang, and P. Szymczak. Effects of mixing at pore intersections on large-scale dissolution patterns and solute transport. *Geophys. Res. Lett.*, 50(21):e2023GL105183, 2023.

[139] A. Raoof, H. M. Nick, T. K. T. Wolterbeek, and C. J. Spiers. Pore-scale modeling of reactive transport in wellbore cement under CO2 storage conditions. *Int J. Greenh. Gas Con.*, 11:S67–S77, 2012.

[140] J. P. Nogues, J. P. Fitts, M. A. Celia, and C. A. Peters. Permeability evolution due to dissolution and precipitation of carbonates using reactive transport modeling in pore networks. *Water Resour. Res.*, 49(9):6006–6021, 2013.

[141] M. J. Blunt, B. Bijeljic, H. Dong, O. Gharbi, S. Iglauer, P. Mostaghimi, A. Paluszny, and C. Pentland. Pore-scale imaging and modelling. *Adv. Water Resour.*, 51:197–216, 2013.

[142] J. Tansey and M. T. Balhoff. Pore network modeling of reactive transport and dissolution in porous media. *Transp. Porous Media*, 113(2):303–327, 2016.

[143] Q. G. Xiong, T. G. Baychev, and A. P. Jivkov. Review of pore network modelling of porous media: Experimental characterisations, network constructions and applications to reactive transport. *J. Contam. Hydrol.*, 192:101–117, 2016.

[144] A. Ameri, A. Raoof, N. C. Blonk, and V. Cnudde. Detailed modeling of carbonate acidizing by coupling a multi-purpose pore-network simulator to the chemistry package PHREEQC-application to chelating agents. *SPE Latin America and Caribbean Petroleum Engineering Conference*, SPE-185532-MS, 2017.

[145] H. Dong and M. J. Blunt. Pore-network extraction from micro-computerized-tomography images. *Phys. Rev. E*, 80(3):036307, 2009.

[146] A. Bejan. *Convection heat transfer*. Wiley, 1984.

[147] N. Gupta and V. Balakotaiah. Heat and mass transfer coefficients in catalytic monoliths. *Chem. Eng. Sci.*, 56(16):4771–4786, 2001.

[148] M. A. Ebadian and Z. F. Dong. Forced convection, internal flow in ducts. In *Handbook of Heat Transfer*. McGraw-Hill, 1998.

[149] B. A. Finlayson. *Nonlinear Analysis in Chemical Engineering*. Ravenna Park Publishing, 1980.

[150] R. P. Sharma, M. Białecki, M. P. Cooper, A. P. Radliński, and P. Szymczak. Pore merging and flow focusing: Comparative study of undissolved and karstified limestone based on microtomography. *Chem. Geol.*, 627:121397, 2023.

[151] C. Dubois, Y. Quinif, J. M. Baele, L. Barriquand, A. Bini, L. Bruxelles, G. Dandurand, C. Havron, O. Kaufmann, B. Lans, et al. The process of ghost-rock karstification and its role in the formation of cave systems. *Earth Sci. Rev.*, 131:116–148, 2014.

[152] E. Merino and A. Banerjee. Terra Rossa genesis, implications for Karst, and Eolian dust: A geodynamic thread. *J. Geol.*, 116:62–75, 2008.

[153] P. Walsh and I. Morawiecka. A dissolution pipe palaeokarst of mid-Pleistocene age preserved in Miocene limestones near Staszów, Poland. *Palaeogeogr. Palaeoclimatol. Palaeoecol.*, 174(4):327–350, 2001.

[154] M. Lipar, P. Szymczak, S. Q. White, and J. A. Webb. Solution pipes and focused vertical water flow: Geomorphology and modelling. *Earth-Sci. Rev.*, 218:103635, 2021.

[155] I. Morawiecka and P. Walsh. A study of solution pipes preseryed in the Miocene limestones (Staszów, Poland). *Acta Carsologica*, 20:337–350, 1997.

[156] C. A. Schneider, W. S. Rasband, and K. W. Eliceiri. NIH image to ImageJ: 25 years of image analysis. *Nat. Methods*, 9(7):671–675, 2012.

[157] A. Sheppard, R. Sok, and H. Averdunk. Improved pore network extraction methods. *International Symposium of the Society of Core Analysts*, 2015.

[158] H. P. Menke, B. Bijeljic, M. G. Andrew, and M. J. Blunt. Dynamic three-dimensional pore-scale imaging of reaction in a carbonate at reservoir conditions. *Environ. Sci. Technol.*, 49(7):4407–4414, 2015.

[159] A. Scanziani, K. Singh, T. Bultreys, B. Bijeljic, and M. J. Blunt. In situ characterization of immiscible three-phase flow at the pore scale for a water-wet carbonate rock. *Adv. Water Res.*, 121:446–455, 2018.

[160] A. Scanziani, K. Singh, H. Menke, B. Bijeljic, and M. J. Blunt. Dynamics of enhanced gas trapping applied to CO2 storage in the presence of oil using synchrotron X-ray micro tomography. *Appl. Energ.*, 259:114136, 2020.

[161] L. Louis. Strength model parameterization as a building block for image-based prediction of mechanical properties. In *53rd US Rock Mechanics/Geomechanics Symposium, New York, USA*, 2019.

[162] M. Voltolini and J. Ajo-Franklin. The effect of CO2-induced dissolution on flow properties in indiana limestone: An in situ synchrotron X-ray micro-tomography study. *Int. J. Greenh. Gas Con.*, 82:38–47, 2019.

[163] M. Doube, M. M. Kłosowski, I. Arganda-Carreras, F. P. Cordelières, R. P. Dougherty, J. S. Jackson, B. Schmid, J. R. Hutchinson, and S. J. Shefelbine. BoneJ: free and extensible bone image analysis in ImageJ. *Bone*, 47(6):1076–1079, 2010.

[164] M. Doube. The ellipsoid factor for quantification of rods, plates, and intermediate forms in 3D geometries. *Front. Endocrinol*, 6:15, 2015.

[165] D. Flinn. On folding during three-dimensional progressive deformation. *Quart. J. Geol. Soc.*, 118(1-4):385–428, 1962.

[166] A. Odgaard and H. J. G. Gundersen. Quantification of connectivity in cancellous bone, with special emphasis on 3D reconstructions. *Bone*, 14(2):173–182, 1993.

[167] K. Janich. *Topology*. Springer, 1984.

[168] H. G. Weller, G. Tabor, H. Jasak, and C. Fureby. A tensorial approach to computational continuum mechanics using object-oriented techniques. *Comput. Phys.*, 12(6):620–631, 1998.

[169] A. Duda, Z. Koza, and M. Matyka. Hydraulic tortuosity in arbitrary porous media flow. *Phys. Rev. E*, 84(3):036319, 2011.

[170] P. Szymczak and A. J. C. Ladd. Wormhole formation in dissolving fractures. *J. Geophys. Res.*, 114(B6), 2009.

[171] I. M. Lifshitz and V. V. Slyozov. The kinetics of precipitation from supersaturated solid solutions. *J. Phys. Chem. Sol.*, 19(1-2):35–50, 1961.

[172] S. Emmanuel, J. J. Ague, and O. Walderhaug. Interfacial energy effects and the evolution of pore size distributions during quartz precipitation in sandstone. *Geochim. Cosmochim. Acta*, 74(12):3539–3552, 2010.

[173] S. Emmanuel and B. Berkowitz. Effects of pore-size controlled solubility on reactive transport in heterogeneous rock. *Geophys. Res. Lett.*, 34(6), 2007.

[174] P. Egermann, S. Békri, and O. Vizika. An integrated approach to assess the petrophysical properties of rocks altered by rock-fluid interactions (CO2 injection). *Petrophysics*, 51:32–40, 2010.

[175] C. N. Fredd and H. S. Fogler. The influence of chelating agents on the kinetics of calcite dissolution. *J. Colloid Interface Sci.*, 204(1):187–197, 1998.

[176] W. Studencki. Facies and sedimentary environment of the Pinczow limestones (Middle Miocene; Holy Cross Mountains, central Poland). *Facies*, 18(1):1–25, 1988.

[177] G. Pieńkowski and G. Niedźwiedzki. Pterosaur tracks from the early Kimmeridgian intertidal deposits of Wierzbica, Poland. *Geol. Q.*, 49:339–346, 2005.

[178] J. Gutowski. Early Kimmeridgian oolitic sedimentary cycle in the Wierzbica quarry, NE margin ot the Holy Cross Mts., Poland. *Volumina Jurassica*, 2(1): 37–48, 2004.

[179] R. Sander. Compilation of Henry's law constants (version 4.0) for water as solvent. *Atmos. Chem. Phys.*, 15(8):4399–4981, 2015.

[180] L. Vincent and P. Soille. Watersheds in digital spaces: an efficient algorithm based on immersion simulations. *IEEE Trans. Pattern Anal. Mach. Intell.*, 13 (6):583–598, 1991.

[181] H. G. Kaganami and Z. Beiji. Region-based segmentation versus edge detection. In *Fifth International Conference on Intelligent Information Hiding and Multimedia Signal Processing*, 2009.

[182] N. Otsu. A threshold selection method from gray-level histograms. *IEEE Trans. Syst. Man Cybern.*, 9(1):62–66, 1979.

[183] S. V. Walt, J. L. Schönberger, J. N. Iglesias, F. Boulogne, J. D. Warner, N. Yager, E. Gouillart, and T. Yu. Scikit-image: image processing in Python. *PeerJ*, 2:e453, 2014.

[184] J. N. Iglesias, A. J. Blanch, O. Looker, M. W. Dixon, and L. Tilley. A new Python library to analyse skeleton images confirms malaria parasite remodelling of the red blood cell membrane skeleton. *PeerJ*, 6:e4312, 2018.

[185] A. A. Hagberg, D. A. Schult, and P. J. Swart. Exploring network structure, dynamics, and function using NetworkX. In *Proceedings of the 7th Python in Science Conference*, pages 11–15, 2008.

[186] W. Schroeder, K. Martin, and B. Lorensen. *The Visualization Toolkit (4th ed.)*. Kitware, 2006.

[187] J. Schwartz, C. Harris, J. Pietryga, H. Zheng, P. Kumar, A. Visheratina, N. A. Kotov, et al. Real-time 3D analysis during electron tomography using Tomviz. *Nat. Commun.*, 13(1), 2022.

[188] J. Ahrens, B. Geveci, and C. Law. *Visualization Handbook*, chapter ParaView: An End-User Tool for Large Data Visualization, pages 717–731. Elsevier Inc., 2005.

[189] P. Ramachandran and G. Varoquaux. Mayavi: 3D visualization of scientific data. *Comput. Sci. Eng.*, 13(2):40–51, 2011.

[190] B. Figarska-Warchoł and G. Stańczak. The effect of petrographic characteristics on the physical and mechanical properties of currently exploited Pińczów limestones – a type of Leitha limestone (Carpathian Foredeep, southern Poland). *Min. Resour. Manag.*, 35:59–98, 2019.

[191] D. R. McDuff, C. E. Shuchart, S. K. Jackson, D. Postl, and J. S. Brown. Understanding wormholes in carbonates: Unprecedented experimental scale and 3D visualization. *J. Petrol. Technol.*, 62:78–81, 2010.

[192] M. Dentz, T. Le Borgne, A. Englert, and B. Bijeljic. Mixing, spreading and reaction in heterogeneous media: A brief review. *J. Contam. Hydrol.*, 120: 1–17, 2011.

[193] B. Berkowitz, C. Naumann, and L. Smith. Mass transfer at fracture intersections: An evaluation of mixing models. *Water Resour. Res.*, 30(6):1765–1773, 1994.

[194] H. W. Stockman, J. Johnson, and S. R. Brown. Mixing at fracture intersections: Influence of channel geometry and the Reynolds and Peclet numbers. *Geophys. Res. Lett.*, 28(22):4299–4302, 2001.

[195] O. Bochet, L. Bethencourt, A. Dufresne, J. Farasin, M. Pédrot, T. Labasque, E. Chatton, N. Lavenant, C. Petton, B. W. Abbott, et al. Iron-oxidizer hotspots formed by intermittent oxic–anoxic fluid mixing in fractured rocks. *Nat. Geosci.*, 13(2):149–155, 2020.

[196] L. C. Hull and K. N. Koslow. Streamline routing through fracture junctions. *Water Resour. Res.*, 22(12):1731–1734, 1986.

[197] P. K. Kang, M. Dentz, and R. Juanes. Predictability of anomalous transport on lattice networks with quenched disorder. *Phys. Rev. E*, 83(3):030101, 2011.

[198] P. K. Kang, M. Dentz, T. Le Borgne, S. Lee, and R. Juanes. Anomalous transport in disordered fracture networks: Spatial Markov model for dispersion with variable injection modes. *Adv. Water Res.*, 106:80–94, 2017.

[199] X. Sanchez-Vila, A. Guadagnini, and J. Carrera. Representative hydraulic conductivities in saturated groundwater flow. *Rev. Geophys.*, 44(3), 2006.

[200] M. F. Gormaly, J. S. Ellis, H. L. MacLean, and A. Bazylak. Pore structure characterization of Indiana limestone and pink dolomite from pore network reconstructions. *Oil Gas Sci. Technol.—Revue d'IFP Energies nouvelles*, 71 (3):33, 2016.

[201] L. W. Lake, S. L. Bryant, and A. N. A. Martinez. *Geochemistry and Fluid Flow*. Elsevier, 2002.

[202] I. Motyka and Z. Wilk. Hydraulic structure of karst-fissured Triassic rocks in the vicinity of Olkusz (Poland). *Kras i Speleologia*, 14:11–24, 1984.

[203] F. L. Paillet, A. E. Hess, C. H. Cheng, and E. Harding. Characterization of fracture permeability with high-resolution vertical flow measurements during borehole pumping. *Ground Water*, 25:28–40, 1987.

[204] W. Dreybrodt. Principles of early development of karst conduits under natural and man-made conditions revealed by mathematical analysis of numerical models. *Water Resour. Res.*, 32:2923–2935, 1996.

[205] A. N. Palmer. Origin and morphology of limestone caves. *Geol. Soc. Am. Bull.*, 103:1–21, 1991.

[206] P. Dijk and B. Berkowitz. Precipitation and dissolution of reactive solutes in fractures. *Water Resour. Res.*, 34:457–470, 1998.

[207] P. G. Saffman. A theory of dispersion in a porous medium. *J. Fluid Mech.*, 6 (03):321, 1959.

[208] C. I. Steefel and A. C. Lasaga. Evolution of dissolution patterns: Permeability change due to coupled flow and reaction. In *Chemical Modeling of Aqueous Systems II*, pages 212–225, 1990.